

FTL REPORT R86-7

AN EXPERIMENTAL AND THEORETICAL STUDY
OF THE ICE ACCRETION PROCESS
DURING ARTIFICIAL AND NATURAL
ICING CONDITIONS

Mark S. Kirby
and R. John Hansman, Jr.

May 1986

MIT

DEPARTMENT
OF
AERONAUTICS
&
ASTRONAUTICS

FLIGHT TRANSPORTATION
LABORATORY
Cambridge, Mass. 02139

FLIGHT TRANSPORTATION LABORATORY REPORT R86-7

AN EXPERIMENTAL AND THEORETICAL STUDY
OF THE ICE ACCRETION PROCESS
DURING ARTIFICIAL AND NATURAL ICING CONDITIONS

Mark Samuel Kirby
and
R. John Hansman, Jr.

May 1986

AN EXPERIMENTAL AND THEORETICAL STUDY
OF THE ICE ACCRETION PROCESS
DURING ARTIFICIAL AND NATURAL ICING CONDITIONS

ABSTRACT

Real-time measurements of ice growth during artificial and natural icing conditions were conducted using an ultrasonic pulse-echo technique. This technique allows ice thickness to be measured with an accuracy of ± 0.5 mm; in addition, the ultrasonic signal characteristics may be used to detect the presence of liquid on the ice surface and hence discern wet and dry ice growth behaviour. Ice growth was measured on the stagnation line of a cylinder exposed to artificial icing conditions in the NASA Lewis Icing Research Tunnel, and similarly for a cylinder exposed in flight to natural icing conditions. Ice thickness was observed to increase approximately linearly with exposure time during the initial icing period. The ice accretion rate was found to vary with cloud temperature during wet ice growth, and liquid runback from the stagnation region was inferred. A steady-state energy balance model for the icing surface was used to compare heat transfer characteristics for icing wind tunnel and natural icing conditions. Ultrasonic measurements of wet and dry ice growth observed in the Icing Research Tunnel and in flight were compared with icing regimes predicted by a series of heat transfer coefficients. The heat transfer magnitude was generally inferred to be higher for the icing wind tunnel tests than for the natural icing conditions encountered in flight. An apparent variation in the heat transfer magnitude was also observed for flights conducted through different natural icing cloud formations.

ACKNOWLEDGMENTS

This work was supported by the National Aeronautics and Space Administration and the Federal Aviation Administration under Grants NGL-22-009-640 and NAG-3-666. Wind tunnel and flight test facilities were provided by the NASA Langley Research Center.

TABLE OF CONTENTS

Abstract	2
Acknowledgements	3
Table of Contents	4
List of Figures	8
List of Tables	11
Nomenclature	12
1. <u>INTRODUCTION</u>	14
1.1 Overview	14
1.2 Aircraft Icing	15
1.3 Modeling The Ice Accretion Process	20
2. <u>STEADY-STATE THERMODYNAMIC ANALYSIS OF AN ICING SURFACE</u>	26
2.1 Modes of Energy Transfer	26
2.2 Control Volume Analysis for an Icing Surface	27
2.2.1 Control Volume Mass Balance	29
i) Mass Balance for Dry Ice Growth	32
ii) Mass Balance for Wet Ice Growth	34
2.2.2 Control Volume Energy Balance	36
i) Energy Balance for Dry Ice Growth	37
ii) Energy Balance for Wet Ice Growth	38
iii) Stagnation Region Energy Balance for Wet Ice Growth	39

iv) Threshold Condition for Transition from Dry to Wet Ice Surface in Stagnation Region	42
2.3 Comparison of Heat Transfer Models	44
3. <u>REAL-TIME MEASUREMENT OF ICE GROWTH USING ULTRASONIC PULSE-ECHO TECHNIQUES</u>	47
3.1 Ultrasonic Pulse-Echo Thickness Measurement	47
3.2 Ultrasonic Signal Characteristics for Dry Ice Growth	50
3.3 Ultrasonic Signal Characteristics for Wet Ice Growth	52
3.4 Summary	56
4. <u>ICING OF A CYLINDER DURING ARTIFICIAL ICING CONDITIONS</u>	57
4.1 Overview	57
4.2 Experimental Apparatus	58
4.3 Icing Research Tunnel Installation and Test Procedure	61
4.3.1 The Icing Research Tunnel	61
4.3.2 Cylinder Installation	63
4.3.3 Test Procedure	64
4.3.4 Test Icing Conditions	65
4.4 Experimental Measurements of Ice Growth During Artificial Icing Conditions	66
4.4.1 Comparison of Ice Growth During Heavy and Light Icing Conditions	67

i) Effect of Exposure Time on Icing Rate	70
ii) Comparison of Ice Accretion Rates for Heavy and Light Icing Conditions	73
iii) Effect of Cloud Temperature on Ice Accretion Rate - Wet and Dry Ice Growth	76
iv) Liquid Runback from the Stagnation Region	81
4.5 Comparison of Different Local Convective Heat Transfer Models for an Icing Surface in the Icing Research Tunnel	83
4.5.1 Stagnation Region Heat Transfer and Ice Shape Prediction	83
4.5.2 Heat Transfer Coefficient Models for the Icing Surface & the Experimental Measurements of Van Fossen et al.	84
4.5.3 Comparison of Heat Transfer Model Results	87
4.6 Summary of Ice Growth Behaviour and Heat Transfer Characteristics	94
5. <u>ICING OF A CYLINDER IN NATURAL ICING CONDITIONS</u>	96
5.1 Overview	96
5.2 Experimental Apparatus	97
5.3 Natural Icing Flight Tests	99
5.3.1 Cylinder Installation on the Icing Research Aircraft	99
5.3.2 Icing Research Aircraft Instrumentation	99
5.3.3 Flight Test Procedure in Natural Icing Conditions	102

5.3.4 Summary of Time-Averaged Natural Icing Conditions and Cylinder Ice Accretions	103
5.4 Ice Growth Behaviour Observed During Natural Icing Conditions	105
5.5 Comparison of Heat Transfer Coefficient Models for the Stagnation Region of a Cylinder in Natural Icing Conditions	112
5.6 Summary of Ice Growth Behaviour and Heat Transfer Analysis for Natural Icing Conditions	118
6. <u>SUMMARY AND CONCLUSIONS</u>	121
REFERENCES	128
APPENDIX A - Measurement of Ice Accretion Using Ultrasonic Pulse-Echo Techniques	130
APPENDIX B - Calculation of Liquid Water Content for Cylinder Location Outside Calibrated Cloud Region	136

LIST OF FIGURES

Chapter 1

1-1	Typical "rime" and "glaze" ice formations	16
1-2	Increase in airfoil drag coefficient due to typical rime and glaze ice accretions	18
1-3	Rapid onset of helicopter rotor icing	19
1-4	Schematic breakdown of analytical ice accretion modeling procedure	21
1-5	Comparison of experimentally measured airfoil ice accretion and analytically predicted ice growth, for rime ice conditions	23
1-6	Effect of assumed surface roughness, k_s , on analytically predicted ice growth, for glaze ice conditions	25

Chapter 2

2-1	Modes of energy transfer for an accreting ice surface	26
2-2	Control volume definition	28
2-3	Local collection efficiency for a 10 cm diameter cylinder, as a function of droplet size	31
2-4	Control volume mass balance for a dry ice surface	33
2-5	Control volume mass balance for a wet ice surface	35
2-6	Stagnation region control volume	39

Chapter 3

3-1	Ultrasonic pulse-echo thickness measurement and typical ultrasonic pulse-echo signal in ice	48
3-2	Ultrasonic signal characteristics for dry ice growth	51
3-3	Ultrasonic signal characteristics for wet ice growth	53

Chapter 4

4-1	Schematic of experimental apparatus configuration	59
4-2	Cylinder installation in Icing Research Tunnel	62
4-3	Photograph of cylinder installation in IRT test section	64
4-4	Ice growth measured for "heavy" icing conditions	68
4-5	Ice growth measured for "light" icing conditions	69
4-6	Average ice accretion rate vs. cloud temperature for "heavy" and "light" icing conditions in the Icing Research Tunnel	78
4-7	Plot of impinging liquid water content versus cloud temperature, showing ultrasonically measured wet/dry ice growth and theoretical wet/dry threshold curves	89
4-8	Plot of impinging liquid water content versus cloud temperature, showing ultrasonically measured wet/dry ice growth and theoretical wet/dry threshold curves	93

Chapter 5

5-1	Photograph of the video camera and oscilloscope installation on the floor of the NASA Lewis Icing Research Aircraft	98
5-2	Cylinder installation on the NASA Lewis Icing Research Aircraft	100
5-3	Photograph showing the test cylinder extended above the roof of the icing research aircraft	101
5-4	Summary of time-averaged icing conditions and cylinder ice accretions for flight tests	104
5-5	Ice thickness vs. exposure time for flight 85-24	106
5-6	Typical icing cloud and flight data for cylinder exposure period (flight 85-22)	108
5-7	Plot of liquid water content versus exposure time for flight 85-24 showing fluctuations in natural icing cloud liquid water content, and wet, dry and transitional ice growth periods measured using ultrasonic system	111
5-8	Plot of impinging liquid water content versus cloud temperature showing wet, dry and transitional ice growth observed during flight tests, and theoretical wet/dry threshold curves	114

LIST OF TABLES

Chapter 4

<u>Table 4-1</u>	Range of icing conditions tested for cylinder in the Icing Research Tunnel.	66
<u>Table 4-2</u>	Summary of ice accretion rates measured for heavy and light icing conditions.	74
<u>Table 4-3</u>	Nusselt number power law relationships, $Nu = A Re^B$, used as models for the stagnation region heat transfer on a cylinder exposed to artificial icing conditions in the Icing Research Tunnel.	87

NOMENCLATURE

A	experimentally derived constant
B	experimentally derived constant
C	speed of sound in ice, m/s
C_i	specific heat capacity of ice, J/Kg. $^{\circ}$ C
C_p	specific heat capacity of air, J/Kg. $^{\circ}$ C
C_w	specific heat capacity of water, J/Kg. $^{\circ}$ C
d	cylinder diameter, m
D	ice thickness, m
\dot{D}	ice accretion rate, m/s
D_w	diffusion coefficient of water vapor in air, m^2/s
h	local convective heat transfer coefficient, $W/m^2.\mathcal{C}$
k	thermal conductivity of air, $W/m.\mathcal{C}$
L_f	latent heat of fusion of water, J/Kg
L_s	latent heat of sublimation of water, J/Kg
L_v	latent heat of vaporization of water, J/Kg
L^*	effective latent heat of fusion, J/Kg
LWC	cloud liquid water content, Kg/m^3
\dot{M}''	local mass flux per unit time, $Kg/m^2.s$
MVD	median volume diameter of cloud droplets, m
n	freezing fraction
Nu	Nusselt number
\dot{Q}''	local heat flux per unit time, W/m^2
r	recovery factor, 0.875
Re	Reynolds number (based on cylinder diameter)
T_{∞}	cloud temperature, \mathcal{C}

ΔT_{∞}	cloud supercooling = $-T_{\infty}$, °C
T_{p-e}	pulse-echo transit time in ice, s
T_{surf}	equilibrium surface temperature, °C
T^*	effective temperature difference, °C
t	exposure time, s
V_{∞}	freestream velocity, m/s
W	cloud liquid water content, Kg/m ³
β	local collection efficiency
ρ_{∞}	freestream air density, Kg/m ³
ρ_{ice}	ice density, Kg/m ³
$\rho_{v,surf}$	saturated water vapor density over surface, Kg/m ³
$\rho_{v,\infty}$	saturated vapor density in cloud, Kg/m ³
μ_{∞}	freestream air viscosity, Kg/m.s

Superscripts

"	per unit area, /m ²
·	per unit time, /s

Chapter 1

INTRODUCTION

1.1 OVERVIEW

The objective of this thesis is to examine the ice accretion process during artificial and natural icing conditions. Experimental measurements of ice growth on a cylinder are compared for artificial icing conditions in an icing wind tunnel, and natural icing conditions encountered in flight. Real-time ultrasonic pulse-echo measurements of ice accretion rate and ice surface condition are used to examine a steady-state energy balance model for the stagnation region of the cylinder. Chapter 2 describes the steady-state model and develops the energy balance equations used to compare the experimental measurements. Chapter 3 outlines the principle of ultrasonic pulse-echo thickness measurement and describes the unique ultrasonic signal characteristics used to detect the presence of liquid water on the ice surface. Chapters 4 and 5 describe real-time measurements of ice growth in the stagnation region of a cylinder exposed to artificial and natural icing conditions. These ultrasonic measurements are then used to compare different heat transfer models applicable to icing wind tunnel and flight icing conditions. Chapter 6 summarizes the

results of the icing experiments and heat transfer analysis conducted.

1.2 AIRCRAFT ICING

Whenever an aircraft encounters liquid water in the form of supercooled cloud droplets, or freezing rain, ice will form on the aircraft's exposed surfaces. Typical cloud droplet diameters range from as large as 50 microns to less than 10 microns. In the case of freezing rain, droplets may be several millimetres in diameter. The shape of the accreted ice and its affect on the aircraft's performance¹ depend on several parameters - the cloud temperature, the average cloud droplet size and the size spectrum, the amount of liquid water per unit volume, W , contained in the cloud and the size, shape and airspeed of the accreting body.

Two distinct icing regimes have been identified. When all of the impinging droplets freeze on impact with the accreting surface the ice formed is characterized as rime ice. The resulting ice shape typically protrudes forward into the airstream, as shown in figure 1-1. Cold cloud temperatures (below -10°C) and small droplet sizes promote rime ice formation.

At warmer cloud temperatures and for the larger droplet sizes and liquid water contents characteristic of these clouds, the freezing process, and the ice shapes formed, are markedly different from the rime ice case. Under these conditions the impinging droplets may not freeze on impact, but instead may coalesce and run back over the accreting surface as liquid water before freezing further downstream on the surface. This type of ice accretion is characterized as glaze ice. Often the resulting ice shape displays two pronounced growth peaks, or horns, on either side of the body stagnation line, as shown in figure 1-1 below.

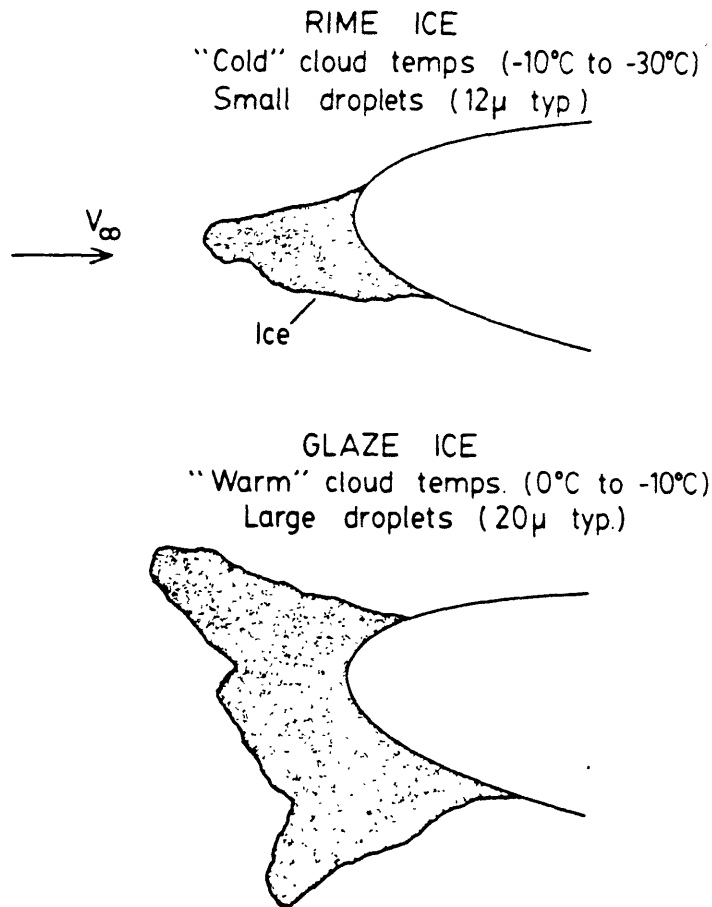


Fig. 1-1 Typical "rime" and "glaze" ice formations.

Ice accretion on aircraft lifting surfaces produces a sharp rise in drag and a reduction in the maximum lift coefficient. This aerodynamic performance degradation is due to both the change in the gross shape of the airfoil, and the increased surface roughness caused by the ice. This increase in surface roughness removes energy from the boundary layer and may result in premature stall. In addition to these aerodynamic penalties, icing of propellers, rotor blades and engine inlets can significantly reduce available power. The change in rotor blade pitching moment, due to helicopter rotor icing, can also result in excessive control loads as well as severe vibration². These effects are illustrated in figures 1-2 and 1-3. Figure 1-2 shows the decrease in aerodynamic performance due to typical rime and glaze ice formations, while figure 1-3 shows the rapid increase in torque and control loads caused by helicopter rotor icing.

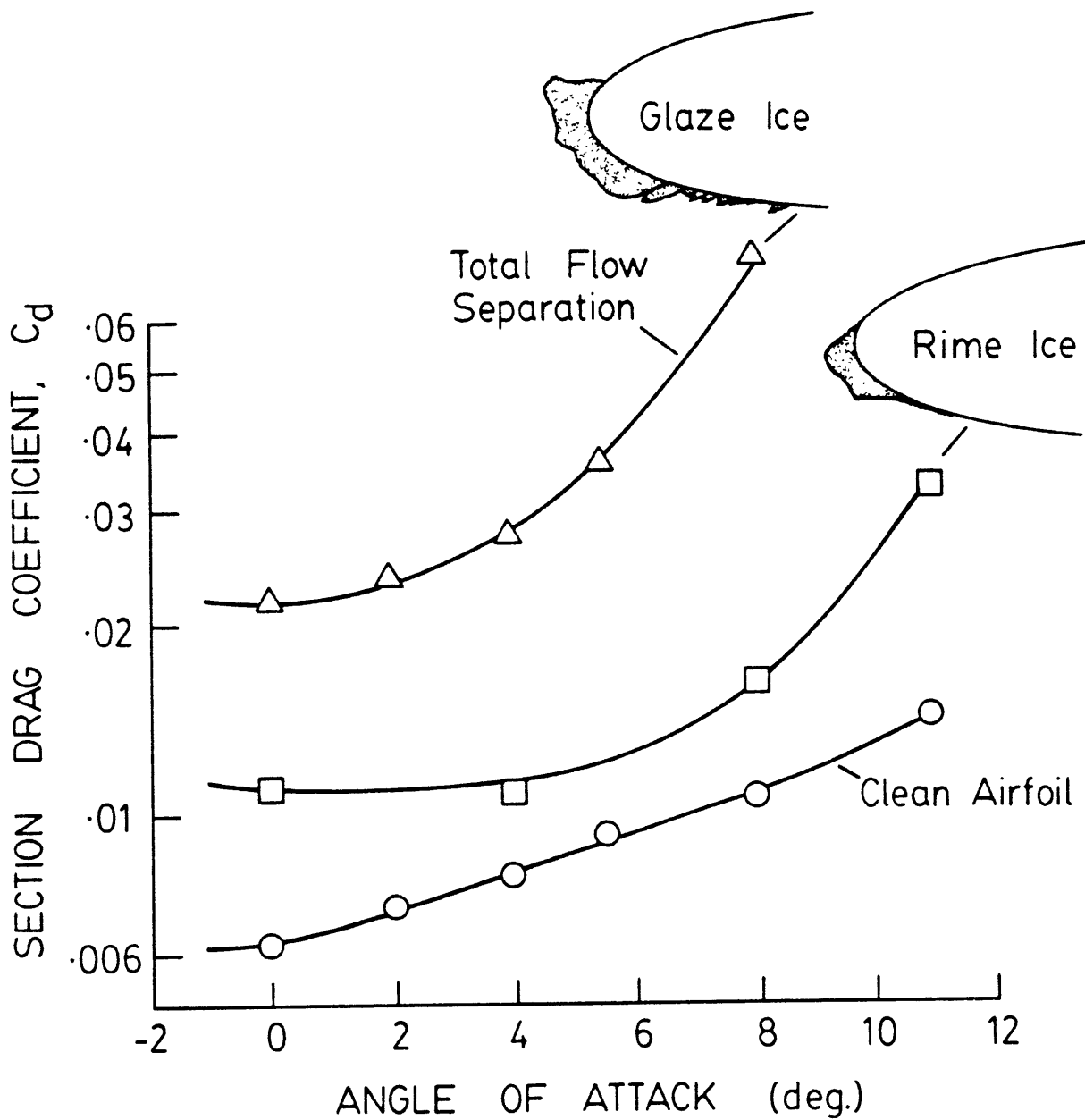


Fig. 1-2 Increase in airfoil drag coefficient due to typical rime and glaze ice accretions. [NACA 0012 airfoil, adapted from Ref. 1]

Rapid onset of rotor icing

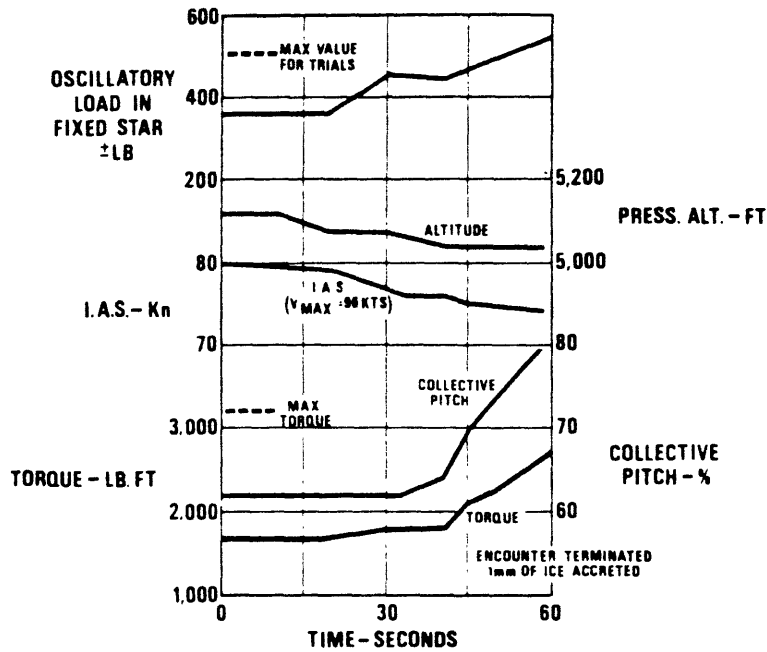


Fig. 1-3 Rapid onset of helicopter rotor icing.
[From Ref. 2]

Growing requirements for aircraft to operate in all weather conditions, coupled with advanced airfoil designs that are more susceptible to the effects of icing and a reduced availability of engine bleed air for thermal anti-icing, have led to renewed interest in aircraft icing research.

Since flight testing in natural icing conditions is inherently time consuming, expensive and potentially dangerous, considerable emphasis has been placed on testing

in icing wind tunnels. Due to facility limitations it is often impossible to test full size aircraft components or to duplicate the desired flight icing conditions; thus accurate icing scaling laws need to be developed in order to alleviate these limitations. Another area that has received considerable attention is the development of computer codes to predict ice accretion under different icing conditions. If the geometry, location and roughness of the ice can be determined then the aerodynamic performance of the iced component can be calculated using appropriate CFD codes. Fundamental to both the development of icing scaling laws and computer codes to predict ice shapes is an accurate physical model of the ice accretion process itself. Current models used to describe the icing process are discussed in the next section.

1.2 MODELING THE ICE ACCRETION PROCESS

Figure 1-4 illustrates schematically how recent³⁻⁵ attempts to analytically model aircraft icing have decomposed the ice accretion process. First, the aerodynamic flowfield around the body of interest is calculated, usually by a potential flow panelling method. Droplet trajectories around the body are then calculated by integrating the droplet equations of motion within the body flowfield.

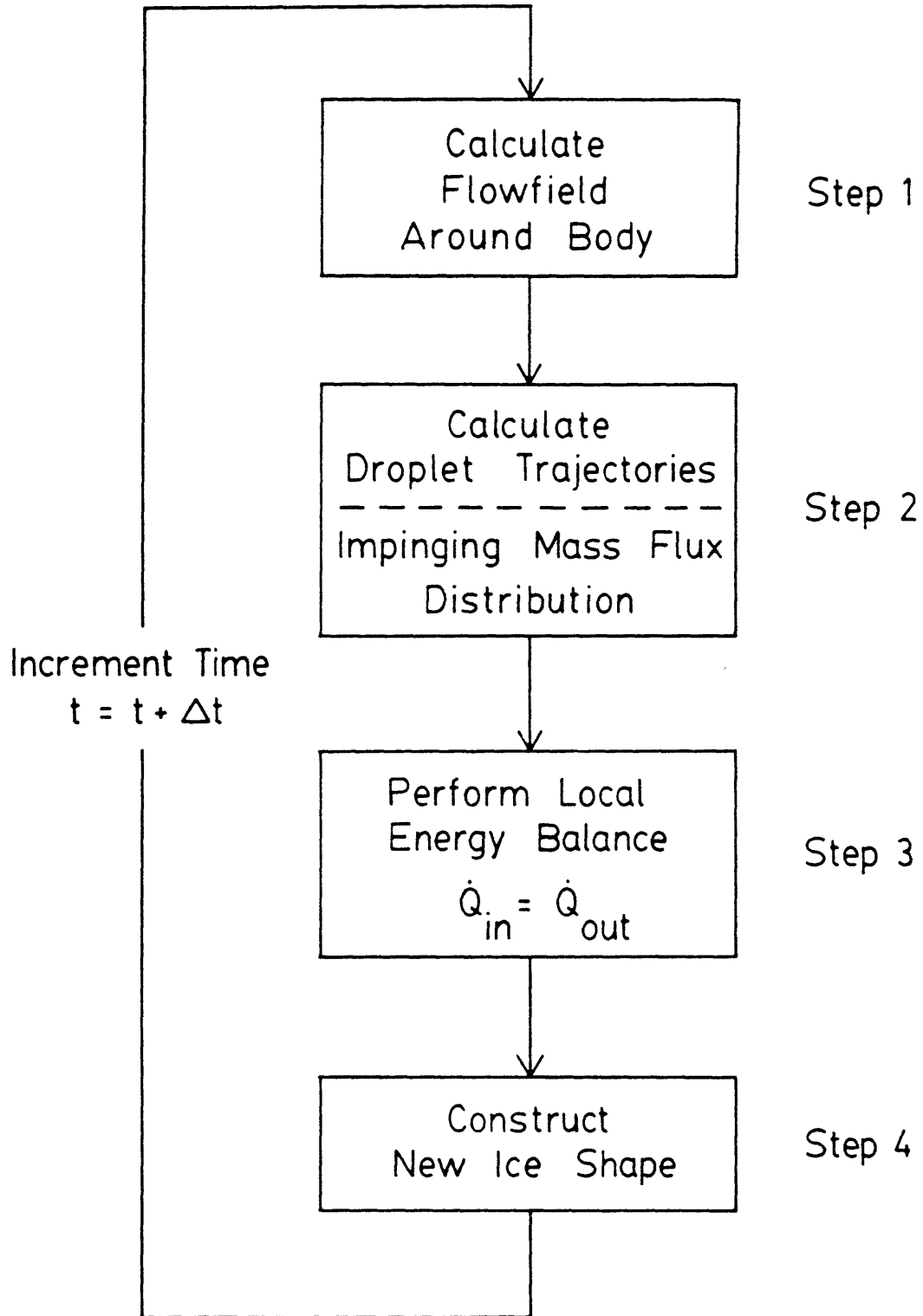


Fig. 1-4 Schematic breakdown of analytical ice accretion modeling procedure.

From these trajectory calculations the impinging mass flux distribution due to the droplets can then be determined around the body.

The third, and crucial step, involves a thermodynamic analysis of the freezing process at the icing surface. Typically a steady-state energy balance is applied to a series of small control volumes along the icing surface. For each control volume the heat of fusion released as the impinging droplets freeze is balanced by the rate at which heat can be removed from the control volume. The final step involves calculating the mass of ice formed at each location on the body as a result of satisfying this energy balance, and constructing the resulting ice shape. This entire process may then be repeated using the iced geometry as input for the flowfield calculation. Due to this form of time-stepped solution, and the inherent feedback relationship between the ice shape and flowfield, any errors in each of these four steps tend to propagate and may result in unrealistic ice shape predictions.

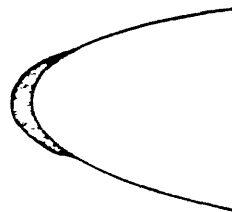
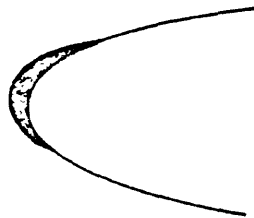
Experimental measurements⁶⁻⁸ have confirmed the accuracy of the flowfield and droplet trajectory calculations. For rime ice growth the droplets are assumed to freeze at the point of impact, and thus no thermodynamic analysis is necessary. In this case the ice shapes predicted are in good

agreement with experimentally measured ice growths^{3,5}, as can be seen in Figure 1-5 below.

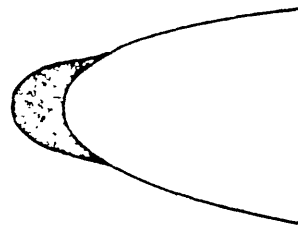
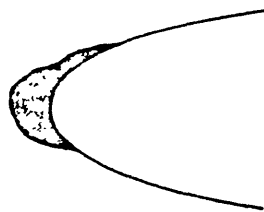
TEMP (°C)	LWC (g/m ³)	MVD (μ)	VEL (m/s)
-26.1	1.02	12	52.1

Experiment (IRT)

Calculated (LEWICE)



Accreted Ice Shape After 2 Minutes Exposure



After 5 Minutes

Fig. 1-5 Comparison of experimentally measured airfoil ice accretion and analytically predicted ice growth, for rime ice conditions. [From Ref. 3]

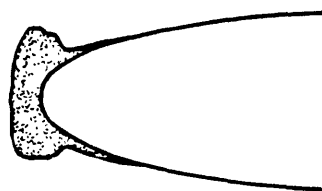
However, for glaze ice conditions the ice shapes predicted using the local energy balance method are extremely sensitive to the assumed convective heat transfer distribution over the body^{3,9,10}. Figure 1-6 illustrates this sensitivity, and shows the variation in glaze ice shapes predicted using different assumed surface roughness heights for the heat transfer calculation. Due, at least in part, to this sensitivity to the heat transfer distribution, and the lack of experimental data in this area, an analytic model capable of accurately predicting ice shapes throughout the glaze icing regime has not yet been demonstrated.

TEMP (°C)	LWC (g/m ³)	MVD (μ)	VEL (m/s)
-14.4	0.96	37.5	93.9

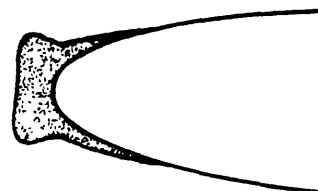
Rime feathers



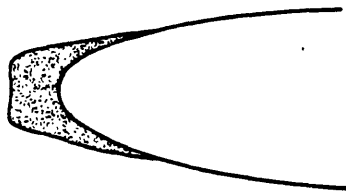
Experiment (IRT)



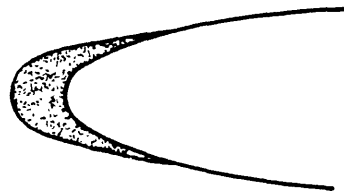
Roughness, $k_S = 0.5\text{mm}$



$k_S = 1.0\text{mm}$



$k_S = 2.0\text{mm}$



$k_S = 4.0\text{mm}$

Calculated (LEWICE)

Fig. 1-6 Effect of assumed surface roughness, k_S , on analytically predicted ice growth, for glaze ice conditions. [From Ref. 9]

Chapter 2

STEADY-STATE THERMODYNAMIC ANALYSIS OF AN ICING SURFACE

2.1 MODES OF ENERGY TRANSFER

The thermodynamic analysis presented here for a surface accreting ice follows the steady-state energy balance approach first proposed by Messinger¹¹. Figure 2-1 shows the modes of energy transfer associated with an icing surface. Six different forms of energy transport are considered.

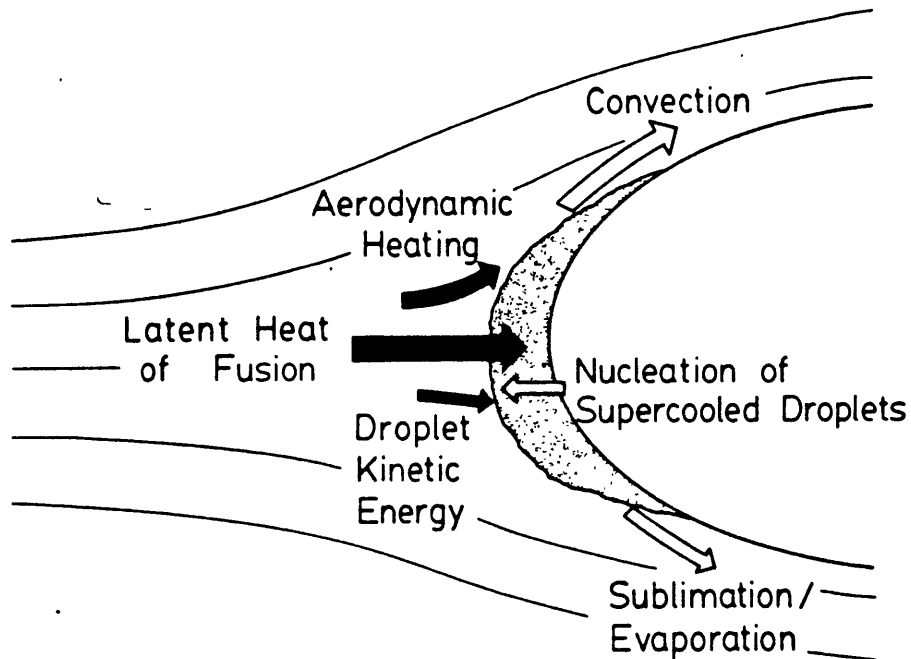


Fig. 2-1 Modes of energy transfer for an accreting ice surface.

Heat is added to the surface primarily due to the latent heat of fusion released as the droplets freeze. Heat is also added by aerodynamic heating, or "ram-rise", and, to an even smaller extent, by the kinetic energy of the impacting droplets. These three terms all represent heat added to the surface, and are schematically illustrated as black arrows in figure 2-1.

Heat is removed from the surface primarily by convection, and to a lesser extent, by either sublimation when the surface is dry, or by evaporation when liquid water is present and the surface is wet. Heat is also absorbed from the surface as the supercooled droplets impinge, nucleate and warm to 0°C. These three terms - convection, sublimation and/or evaporation, and droplet warming - represent heat removed from the surface, and are shown as white arrows in figure 2-1. All of these modes of energy transfer will be discussed in more detail following the development of the control volume analysis in the next section.

2.2 CONTROL VOLUME ANALYSIS FOR AN ICING SURFACE

In view of the complexity of the icing process, it is convenient to subdivide the icing surface into a series of small control volumes, as shown in figure 2-2.

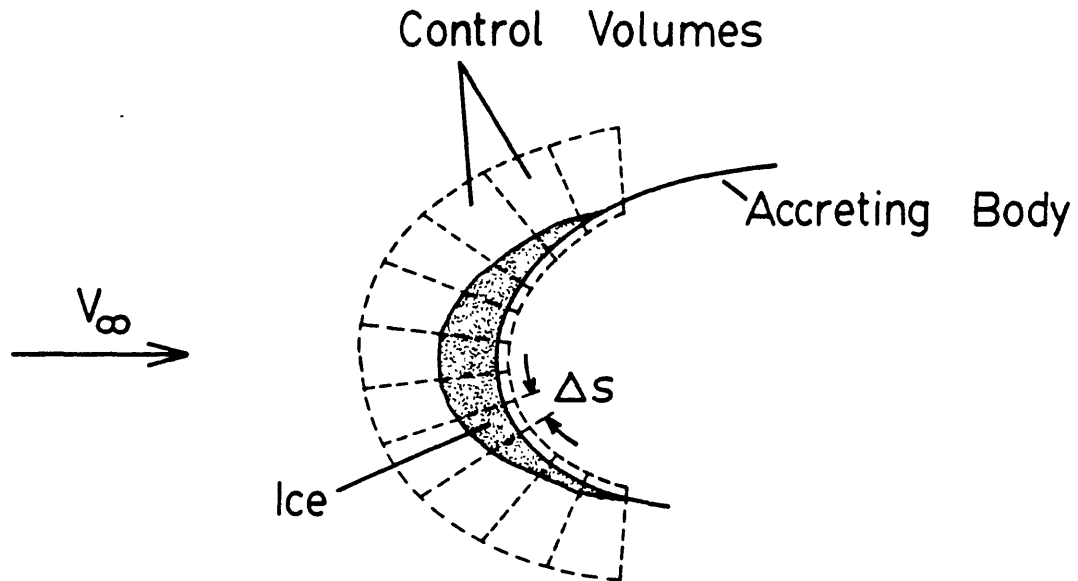


Fig. 2-2 Control Volume Definition.

If a sufficiently short time interval is considered, so that the flowfield is not significantly altered by the ice growth during that period, and if the ambient icing conditions remain constant throughout the time interval, then each control volume will experience quasi steady-state icing conditions. This quasi steady-state assumption is fundamental to the thermodynamic analysis presented here for the icing surface and again is only valid when:

1. The ice growth during the time period considered does not significantly alter the flowfield.
2. The ambient icing conditions do not vary significantly over the time period considered.
3. The control volume is sufficiently small so that spatial

variations may be neglected.

The effects of unsteady ambient icing conditions, frequently encountered in flight, are discussed in Chapters 5 and 6. The mass and energy balances appropriate to the quasi steady-state case are presented in the following sections.

2.2.1 CONTROL VOLUME MASS BALANCE

The mass flux per unit time (kg/s-m^2) due to impinging water droplets, $\dot{M}''_{\text{impinging}}$, varies with position on the accreting body and is given by,

$$\dot{M}''_{\text{impinging}} = \beta W V_{\infty} \quad (2.1)$$

Where the double prime superscript indicates per unit surface area on the icing surface, W is cloud liquid water content in grams/m^3 , V_{∞} is the freestream velocity and β is the "local collection efficiency" of the body. The local collection efficiency is defined as the ratio of the local mass flux due to the impinging water droplets to the droplet mass flux in the freestream, i.e.,

$$\beta = \frac{\text{Impinging droplet mass flux}}{\text{Freestream droplet mass flux}} \quad (2.2)$$

The local collection efficiency, β , is governed by the ratio of the impinging droplets inertia to the aerodynamic drag on them due to the freestream disturbance created by the body. For most aircraft icing regimes the local collection efficiency is primarily a function of the cloud droplet size, characterized by the droplet median volume diameter (MVD), and the size of the accreting body.

Figure 2-3 is a plot of the local collection efficiency for a cylinder. The local collection efficiency is plotted as a function of cylinder angle for several different cloud droplet diameters. The local collection efficiency is a maximum on the stagnation line ($\theta = 0^\circ$), and decreases with increasing cylinder angle. Both the impingement area and the local collection efficiency increase with droplet size, due to the higher inertia of the droplets. In general then, a small body moving rapidly through a cloud of large droplets will have a much higher collection efficiency than a large body moving slowly through a cloud of small droplets.

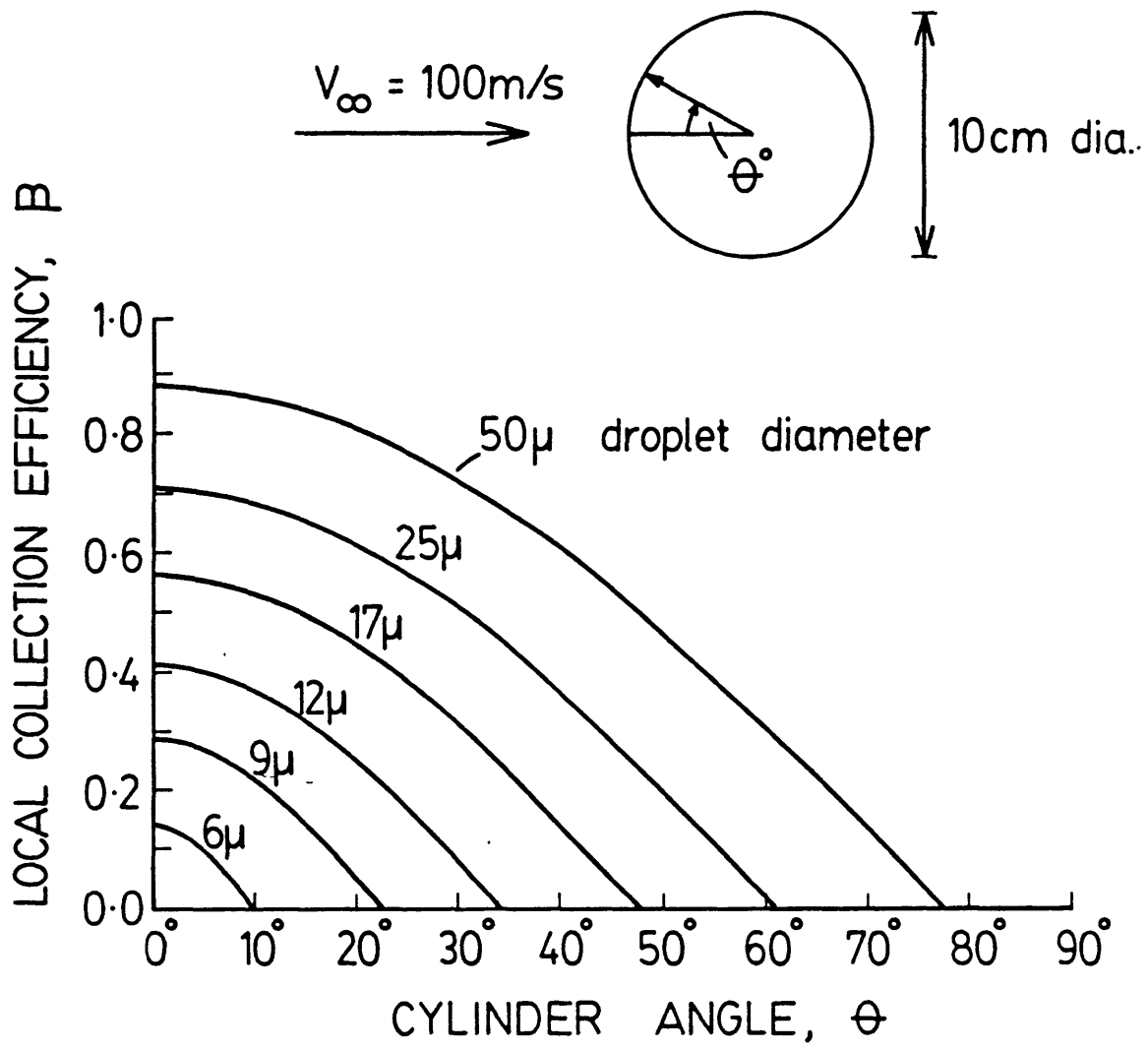


Fig. 2-3 Local collection efficiency for a 10 cm diameter cylinder, as a function of droplet size.

i) MASS BALANCE FOR DRY ICE GROWTH

When all the impinging droplets freeze on impact with the accreting surface, the ice surface is "dry". Figure 2-4 schematically illustrates this condition. The control volume mass balance equation is given by,

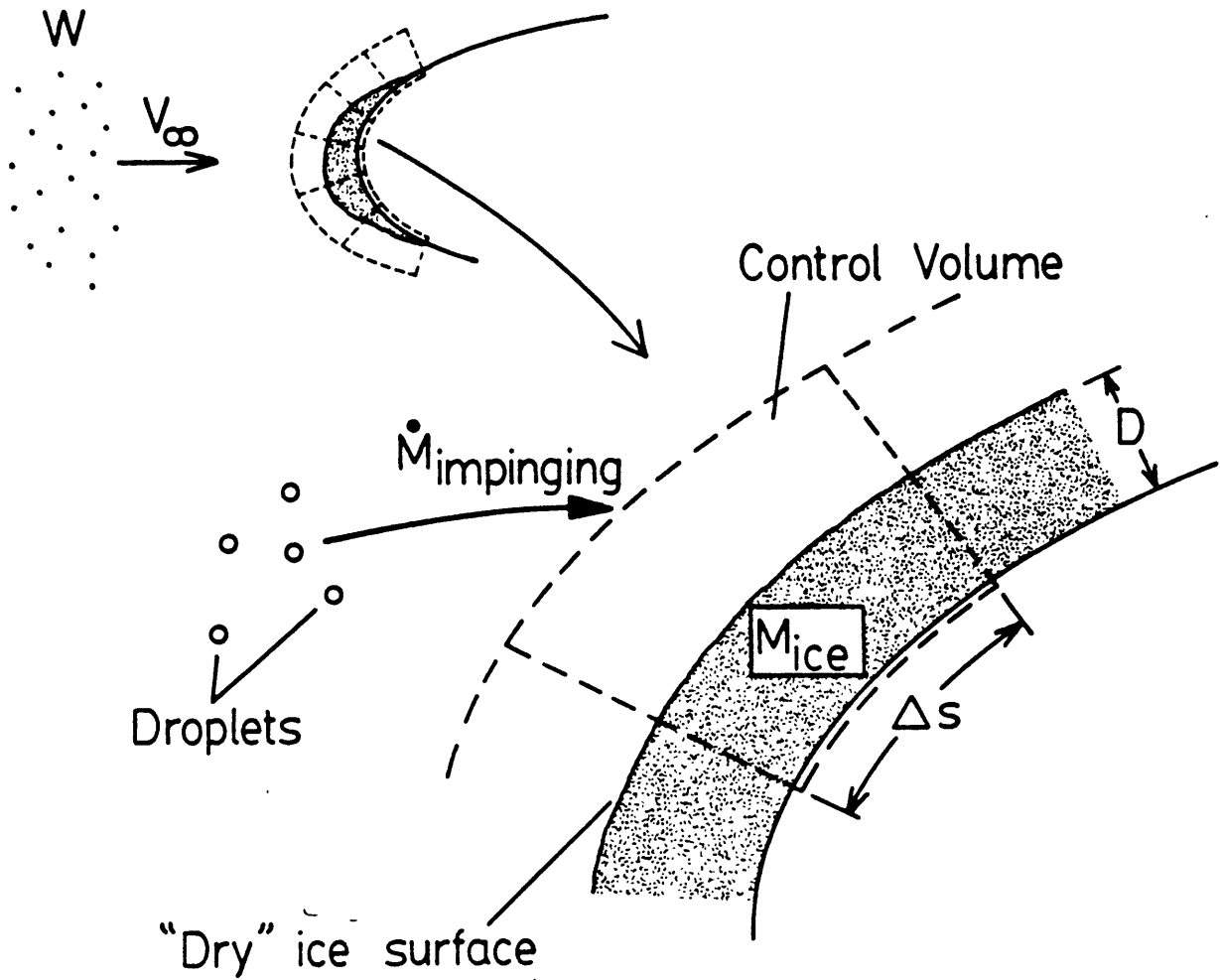
$$\dot{M}''_{ice} = \dot{M}''_{impinging} = \beta W V_{\infty} \quad (2.3)$$

Where again the double prime superscript indicates per unit surface area of the icing surface. Equation 2.3 simply states that the mass of ice formed per unit area per unit time, \dot{M}''_{ice} , is equal to the local mass flux per unit time due to the impinging droplets, $\dot{M}''_{impinging}$. In this equation, and throughout this analysis, the small contribution to the mass balance due to sublimation (or evaporation in the case of a wet ice surface) has been neglected.

The rate at which the local ice thickness, D , increases, is referred to as the ice accretion rate, \dot{D} . For dry ice growth, the ice accretion rate is given by,

$$\dot{D} = \dot{M}''_{ice} / \rho_{ice} = \beta W V_{\infty} / \rho_{ice} \quad (2.4)$$

Where ρ_{ice} is the density of the accreted ice.



$$\dot{M}_{ice}'' = \dot{M}_{impinging}'' = \beta W V_\infty$$

Fig. 2-4 Control volume mass balance for a dry ice surface.

ii) MASS BALANCE FOR WET ICE GROWTH

If the rate at which heat can be removed from the icing surface is insufficient to freeze all of the locally impinging droplets, the ice surface will become wet, as shown schematically in figure 2-5.

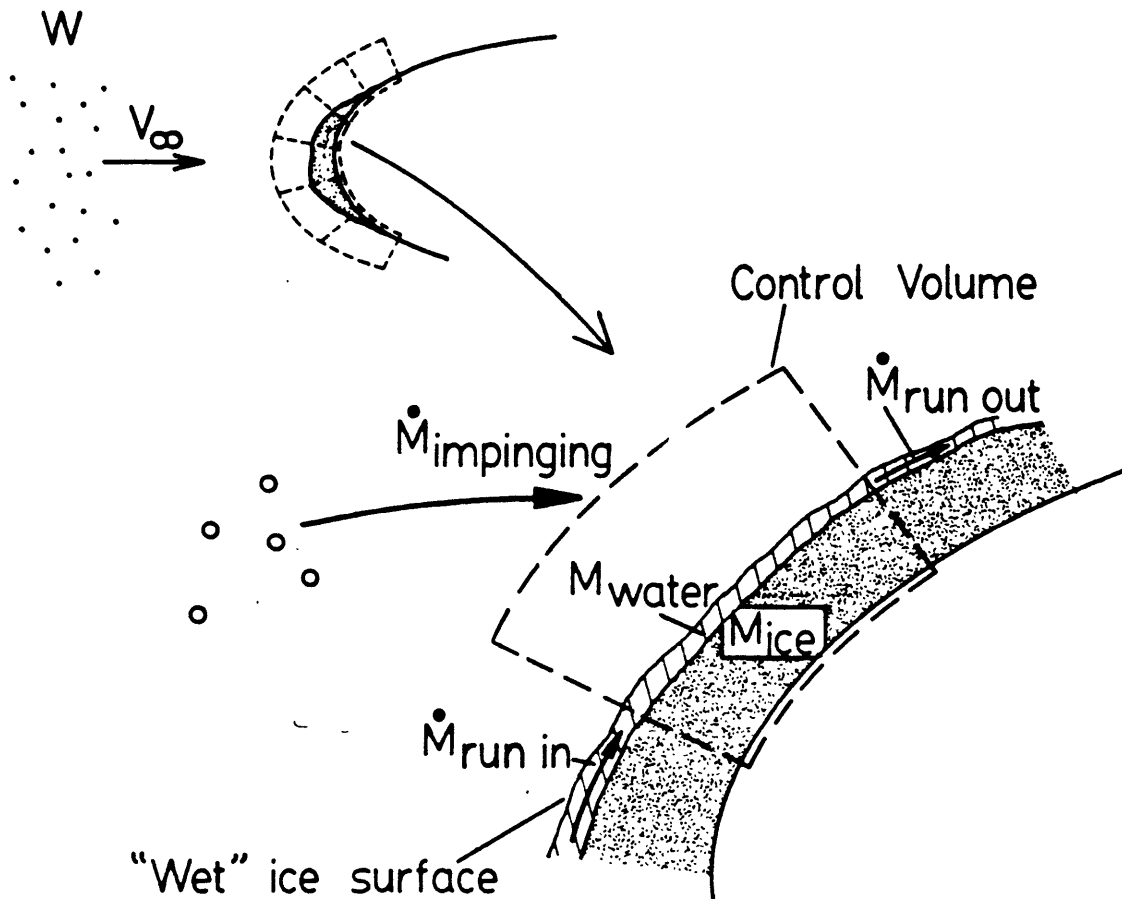
Liquid water on the ice surface will, in general, first appear in the stagnation region of the body, where the impinging mass flux is a maximum. In this model, liquid water formed on the icing surface is assumed to flow downstream from the stagnation region, driven by the external flowfield. This flow of liquid over the icing surface is known as "run-back".

The control volume mass balance in the case of a wet ice surface with run-back liquid present is thus,

$$\dot{M}_{ice} = \dot{M}_{impinging} + \dot{M}_{run\ in} - \dot{M}_{run\ out} \quad (2.5)$$

Where $\dot{M}_{run\ in}$ and $\dot{M}_{run\ out}$ represent the mass flows (kg/sec) into, and out of, the control volume due to run-back liquid (see figure 2-5). The mass of liquid in the control volume, M_{water} , is taken to be constant, i.e. it is assumed in this model that there is no accumulation of liquid in the control volume in the steady-state. The mass flux per unit time of droplets impinging on the local control volume, $\dot{M}''_{impinging}$,

is equal to $\beta W V_\infty$, as in the dry surface case. Now however, the run-back mass flows, $\dot{M}_{\text{run in}}$ and $\dot{M}_{\text{run out}}$, are unknown and must be determined from energy considerations. The next section considers the control volume energy balance, first for the dry surface case and then for the wet surface.



$$\dot{M}_{\text{ice}} \approx \dot{M}_{\text{impinging}} + \dot{M}_{\text{run in}} - \dot{M}_{\text{run out}}$$

Fig. 2-5 Control volume mass balance for a wet ice surface.

2.2.2 CONTROL VOLUME ENERGY BALANCE

As discussed in section 2.1, six modes of energy transfer to and from the icing surface are considered. The steady-state assumption requires that the rate at which energy is added to any control volume equals the rate at which it is removed. Thus the fundamental energy equation for the control volume is,

$$\dot{Q}''_{in} = \dot{Q}''_{out} \quad (2.6)$$

Where \dot{Q}''_{in} and \dot{Q}''_{out} respectively represent the energy added to, and removed from, the control volume, per unit area per unit time. Equation 2.6 may be expanded into its component energy terms as,

$$\dot{Q}''_{in} = \dot{Q}''_{freezing} + \dot{Q}''_{aero\ heating} + \dot{Q}''_{droplet\ k.e.} \quad (2.7)$$

$$\dot{Q}''_{out} = \dot{Q}''_{conv} + \dot{Q}''_{subl} + \dot{Q}''_{droplet\ warming} \quad (2.8)$$

The ice surface is assumed to attain a steady-state, locally uniform surface temperature, T_{surf} . If the ice surface is dry then the surface temperature must be less than, or just equal to, $0^{\circ}C$. If the ice surface is wet the surface temperature is assumed to be $0^{\circ}C$. Steady-state conduction into the icing surface is assumed to be zero, and

chordwise conduction between adjacent control volumes is neglected.

i) ENERGY BALANCE FOR DRY ICE GROWTH

With these assumptions and definitions, equations 2.7 and 2.8 may be expanded for the dry ice surface case as,

$$\dot{Q}''_{\text{freezing}} = \dot{M}''_{\text{imp}} [L_f + C_i(0^\circ\text{C} - T_{\text{surf}})] \quad (2.9)$$

$$\dot{Q}''_{\text{aero heating}} = h r v_\infty^2 / 2 c_p \quad (2.10)$$

$$\dot{Q}''_{\text{droplet k.e.}} = \dot{M}''_{\text{imp}} v_\infty^2 / 2 \quad (2.11)$$

$$\dot{Q}''_{\text{convection}} = h(T_{\text{surf}} - T_\infty) \quad (2.12)$$

$$\dot{Q}''_{\text{sublimation}} = h D_w L_s (\rho_{v,\text{surf}} - \rho_{v,\infty}) / k \quad (2.13)$$

$$\dot{Q}''_{\text{droplet warming}} = \dot{M}''_{\text{imp}} c_w \Delta T_\infty \quad (2.14)$$

Control volume energy transfer terms for a dry ice surface.

In these equations T_{surf} is the equilibrium surface temperature in degrees Centigrade and \dot{M}''_{imp} is the mass flux

per unit time of droplets impinging on the control volume, BWV_∞ . Using this expression for \dot{M}''_{imp} , and combining all the above equations (2.9 - 2.14), yields the steady-state energy balance equation for a dry ice surface,

$$\begin{aligned}
 BWV_\infty [L_f + C_i(0^\circ\text{C} - T_{surf}) + v_\infty^2/2] + hr v_\infty^2/2C_p = \\
 h[(T_{surf} - T_\infty) + D_w L_s (\rho_{v,surf} - \rho_{v,\infty})/k] + BWV_\infty C_w \Delta T_\infty
 \end{aligned}
 \tag{2.15}$$

Steady-state energy balance equation for a dry ice surface.

ii) ENERGY BALANCE FOR WET ICE GROWTH

In considering the energy balance for the wet surface case, it is convenient to define a quantity n , the "freezing fraction" as,

$$n \equiv \frac{\dot{M}_{ice}}{\dot{M}_{imp} + \dot{M}_{run\ in}} \tag{2.16}$$

The freezing fraction is thus the ratio of the mass of ice formed per unit time to the total mass of water entering the control volume, per unit time.

When the ice surface is dry the freezing fraction is always unity since $\dot{M}_{ice} = \dot{M}_{imp}$, and $\dot{M}_{run\ in}$ is zero since no

liquid is present on the ice surface. For a wet ice surface the freezing fraction must lie between zero and unity. For simplicity only the stagnation region energy balance will be considered for the wet surface case.

iii) STAGNATION REGION ENERGY BALANCE FOR WET ICE GROWTH

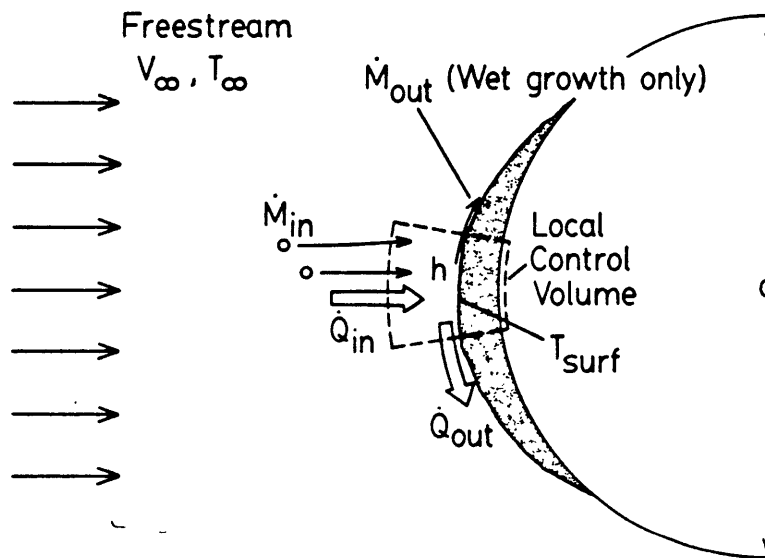


Fig. 2-6 Stagnation region control volume.

Figure 2-6 depicts the stagnation region control volume examined for the wet surface case. Since only the stagnation region is considered, the only liquid entering the control volume is due to impinging droplets, and no liquid runs into the control volume, i.e. $\dot{M}_{run\ in} = 0$. From equation 2.16,

the freezing fraction, n , is thus simply,

$$n = \dot{M}_{ice} / \dot{M}_{imp} \quad (2.17)$$

Although no liquid runs into the stagnation region, liquid may flow out of the control volume along the ice surface. Using the mass balance equation (2.5) for the wet surface, equation 2.17 may thus be written as,

$$n = \frac{\dot{M}_{imp} - \dot{M}_{run\ out}}{\dot{M}_{imp}} = 1 - \frac{\dot{M}_{run\ out}}{\dot{M}_{imp}} \quad (2.18)$$

For the wet surface, the energy balance is altered from the dry surface case in the following ways. The rate at which ice is formed, per unit surface area, \dot{M}''_{ice} , is reduced from the dry rate, $\dot{M}''_{imp} = \beta W V_{\infty}$, to,

$$\dot{M}''_{ice} = n \dot{M}''_{imp} = n \beta W V_{\infty} \quad (2.19)$$

The ice accretion rate, \dot{D} , for the wet surface is thus,

$$\dot{D} = \dot{M}''_{ice} / \rho_{ice} = n \beta W V_{\infty} / \rho_{ice} \quad (2.20)$$

The heat flux per unit time due to freezing, $\dot{Q}''_{\text{freezing}}$, can be obtained from equations 2.9 and 2.19 as,

$$\dot{Q}''_{\text{freezing}} = \dot{M}''_{\text{ice}}[L_f + C_i(0^\circ\text{C} - T_{\text{surf}})] \quad [2.9]$$

$$= n\beta W V_\infty L_f \quad (2.21)$$

Where L_f is the latent heat of fusion for water. Note that the equilibrium temperature, T_{surf} , for the wet surface is assumed to be 0°C , and thus there is no subsequent cooling of the accreted ice.

In addition, evaporation, rather than sublimation, now removes heat from the ice surface, and hence the latent heat of vaporization, L_v , is used in the energy balance equation,

$$\dot{Q}''_{\text{evap}} = hD_w L_v (\rho_{v,\text{surf}} - \rho_{v,\infty})/k \quad (2.22)$$

The four remaining energy transport terms in the energy balance - aerodynamic heating, droplet kinetic energy, convection, and droplet warming (nucleation) - are unchanged in the wet surface formulation. However, since the surface temperature, T_{surf} , is now assumed to be 0°C , both the convective and evaporative heat loss terms are evaluated for a surface at 0°C . With this, the energy balance equation for the wet surface may be written as,

$$\dot{Q}''_{\text{freezing}} + \dot{Q}''_{\text{droplet k.e.}} + \dot{Q}''_{\text{aero heating}} =$$

$$\dot{Q}''_{\text{conv}} + \dot{Q}''_{\text{evap}} + \dot{Q}''_{\text{droplet warming}} \quad (2.23)$$

$$BWV_{\infty}[nL_f + V_{\infty}^2/2] + hrV_{\infty}^2/2C_p =$$

$$h[(0^{\circ}\text{C} - T_{\infty}) + D_w L_v (\rho_{v,0^{\circ}\text{C}} - \rho_{v,\infty})/k] + BWV_{\infty} C_w \Delta T_{\infty} \quad (2.24)$$

Stagnation region energy balance equation for a wet ice surface.

iv) THRESHOLD CONDITION FOR TRANSITION FROM DRY TO WET ICE SURFACE IN STAGNATION REGION

Of particular interest is the condition for which the ice surface transitions from dry to wet. For the stagnation region control volume considered above, this transition must occur when the equilibrium surface temperature is 0°C and the freezing fraction is very slightly less than unity. For this case, the stagnation region energy balance equation (2.24) may be rearranged to yield a "critical impinging liquid water content", $(BW)_{\text{crit}}$, given by,

$$(BW)_{\text{crit}} = \frac{h[(0^{\circ}\text{C} - T_{\infty}) + D_w L_v (\rho_{v,0^{\circ}\text{C}} - \rho_{v,\infty})/k - rV_{\infty}^2/2C_p]}{V_{\infty}[L_f + V_{\infty}^2/2 - C_w \Delta T_{\infty}]} \quad (2.25)$$

For this limiting case between dry and wet growth, the freezing fraction has been taken to be unity. Equation 2.25 states that, for a given freestream airspeed, ambient temperature and local heat transfer coefficient, there exists a critical "effective" cloud liquid water content above which the icing surface will become wet. This effective liquid water content is the product of the local collection efficiency of the surface and the cloud liquid water content. Since the local collection efficiency is a strong function of the cloud droplet size, this parameter, $(\beta W)_{crit}$, may be regarded as primarily an icing cloud property.

From equation 2.25 it can be seen that the value of βW at which transition between wet and dry ice growth occurs depends on the magnitude of the local heat transfer coefficient, h . It should, therefore, be possible to obtain the local heat transfer coefficient over an icing surface by carefully measuring the impinging liquid water content for which the surface just becomes wet.

The approach taken in this thesis is to compare experimentally observed cases of wet and dry ice growth with the regimes of wet and dry ice growth predicted by a series of heat transfer coefficient models. This comparison of different physical heat transfer models (rough or smooth

surface, for example), enables the actual heat transfer processes occurring during natural and artificial icing conditions to be better understood and modeled.

2.3 COMPARISON OF HEAT TRANSFER MODELS

In order to compare different heat transfer coefficient models is convenient to express the local heat transfer coefficient, h , in terms of the non-dimensional Nusselt number, Nu , where,

$$Nu = h d/k \quad (2.26)$$

With d being the uniced diameter (or characteristic dimension) of the body, and k the thermal conductivity of air. It is common to model heat transfer coefficients in the form of a power law relationship between the Nusselt number and the Reynolds number, Re , as,

$$Nu = A Re^B = A (\rho_{\infty} V_{\infty} d / \mu_{\infty})^B \quad (2.27)$$

Where A and B are experimentally derived constants.

Using these relationships for the heat transfer coefficient (eqs. 2.26 & 2.27), allows the steady-state

energy balance equation for transition between wet and dry ice growth (eq. 2.25), to be rewritten as,

$$(BW)_{crit} = A k (\rho_{\infty}/\mu_{\infty})^B (V_{\infty}d)^{B-1} (T^*/L^*) \quad (2.28)$$

Where $(BW)_{crit}$ is the critical impinging liquid water content, above which the ice surface is expected to be wet. The constants A and B represent the convective heat transfer coefficient "model", or power law. The terms T^* and L^* introduced in equation 2.28 are defined below as,

$$T^* = [(0^{\circ}C - T_{\infty}) + D_w L_v (\rho_{v,0^{\circ}C} - \rho_{v,\infty})/k - rV_{\infty}^2/2C_p] \quad (2.29)$$

$$L^* = [L_f + V_{\infty}^2/2 - C_w \Delta T_{\infty}] \quad (2.30)$$

The term T^* can be thought of as representing the effective temperature difference (in $^{\circ}C$) between the icing surface and the freestream. This effective temperature difference thus controls the rate at which heat is removed from the icing surface by convection and evaporation. The effect of aerodynamic heating is also included in this temperature difference term.

In a similar way, the term L^* represents an effective heat of fusion (in J/Kg) "released" during the accretion process. This term combines the latent heat of fusion of water, L_f , the droplet specific kinetic energy, $V_{\infty}^2/2$, and

the effective heat absorbed due to droplet warming on impact, $C_w \Delta T_\infty$. Since the droplet kinetic energy and droplet warming terms are typically an order of magnitude smaller than the latent heat of fusion of water, the parameter L^* is, in most cases, essentially equal to L_f .

Equation 2.28 thus represents the wet/dry threshold for the stagnation region of a body, predicted by the steady-state energy balance analysis. If the impinging liquid water content is less than the value of $(\beta W)_{crit}$ in equation 2.28, then the ice surface is predicted to be dry; while if βW is greater than $(\beta W)_{crit}$ then the ice surface is expected to be wet.

From this equation it can be seen that $(\beta W)_{crit}$ depends on the assumed values of A and B in the heat transfer coefficient model. By measuring the locally impinging liquid water content, βW , and whether the resulting ice surface is wet or dry, it is thus possible to compare different heat transfer models and determine which physical model best predicts the observed wet or dry ice growth. The ultrasonic pulse-echo techniques used to perform these experimental measurements of ice accretion rate and ice surface condition are described in the next chapter.

Chapter 3

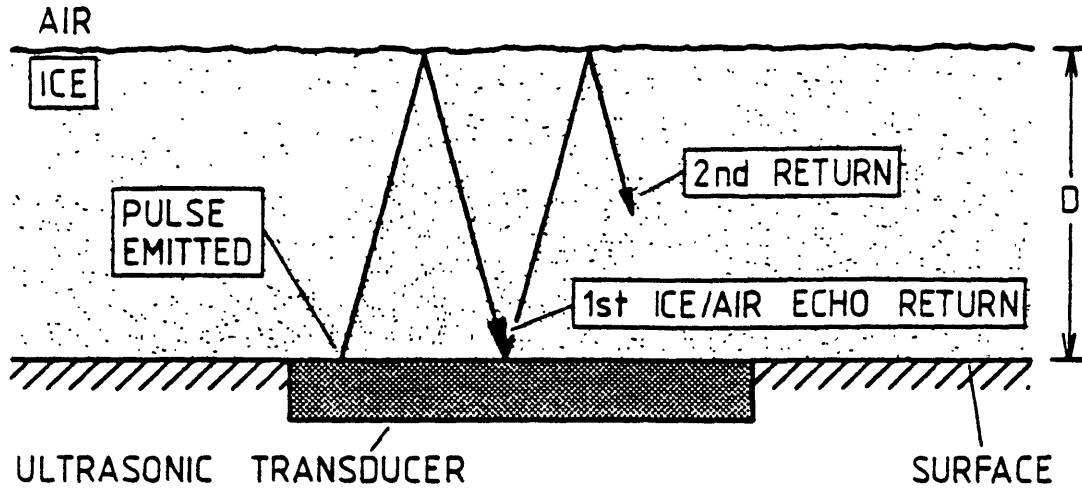
REAL-TIME MEASUREMENT OF ICE GROWTH USING ULTRASONIC PULSE-ECHO TECHNIQUES

3.1 ULTRASONIC PULSE-ECHO THICKNESS MEASUREMENT

Figure 3-1 illustrates the principle of ultrasonic pulse-echo thickness measurement for an icing surface. A small transducer mounted flush with the accreting surface emits a brief compressional wave, the ultrasonic "pulse", that travels through the ice as shown. Typical transducer frequencies used to generate the compressive wave are between 1 and 5 MHz. This pulse is reflected at the ice surface and returns to the emitting transducer as an echo signal. By measuring the time elapsed between the emission of the pulse and the return of the echo, T_{p-e} , the ice thickness over the transducer, D , may be calculated from the formula,

$$D = C T_{p-e}/2 \quad (3.1)$$

Where C is the speed of propagation of the compressional wave in ice.



$$D = \frac{C \cdot T_{p-e}}{2}$$

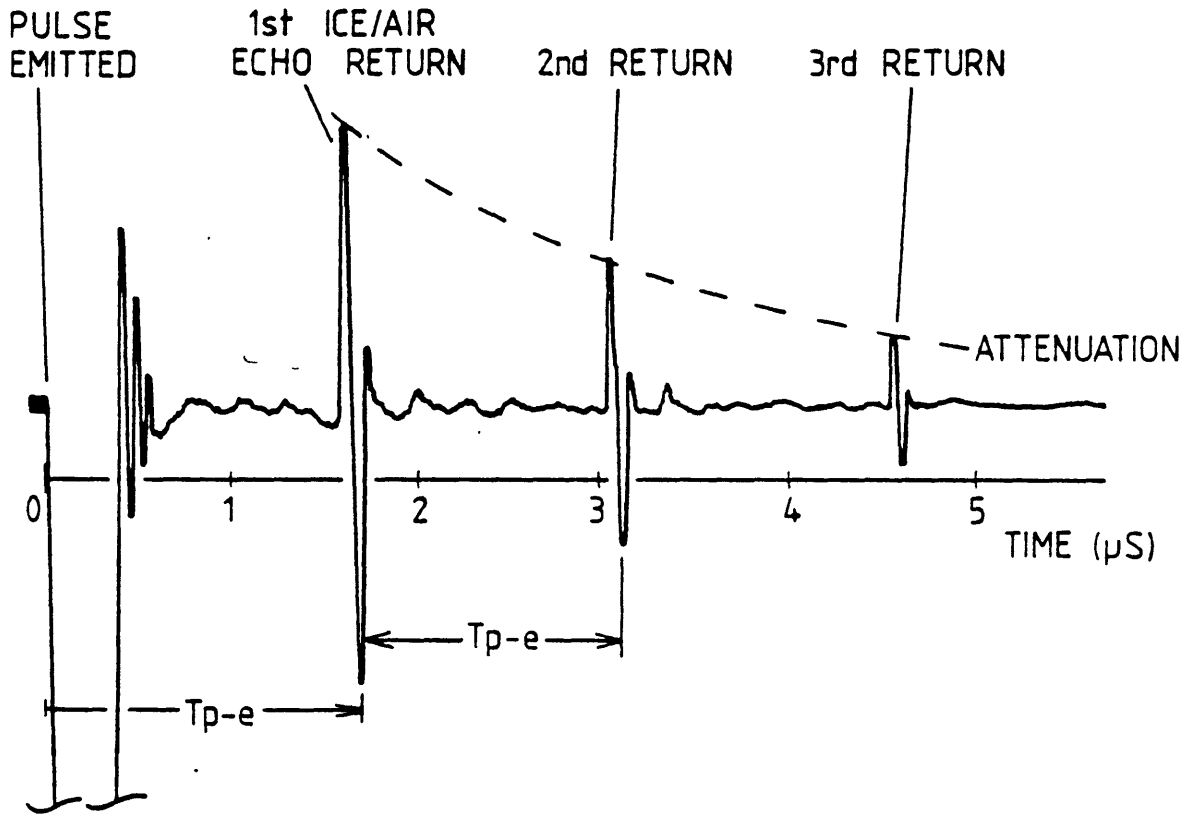


Fig. 3-1 Ultrasonic pulse-echo thickness measurement and typical ultrasonic pulse-echo signal in ice.

This speed of propagation has been shown (see Appendix A) to be insensitive to the different types of ice (glaze, rime and mixed) accreted at typical flight airspeeds; a value of 3.8mm/ μ sec has been used for all the results presented in this thesis. Experimental measurements of the variation in the speed of sound for different ice formations are contained in Appendix A, along with a more detailed discussion of the ultrasonic pulse-echo technique.

Figure 3-1 also shows a typical ultrasonic pulse-echo signal obtained from a stationary, i.e. non-accreting, ice surface. As indicated in the figure, the time elapsed between the emission of the pulse and the return of the echo from the ice surface is on the order of microseconds for the ice thicknesses of concern for aircraft icing (1mm-20mm). By repeatedly emitting pulses, the ice thickness can be constantly measured as ice accretes on the body. Pulses are typically emitted several thousand times a second, and hence essentially "real-time" measurement of the ice thickness is possible. In addition to obtaining the ice thickness from the pulse-echo transit time, the presence or absence of liquid water on the ice surface may be detected from the characteristics of the received echo signal. These signal characteristics are discussed in the next two sections.

3.2 ULTRASONIC SIGNAL CHARACTERISTICS FOR DRY ICE GROWTH

If all the droplets impinging at a given location on a body freeze on impact, the freezing fraction is unity and the ice surface formed will be "dry", as discussed in Chapter 2. This form of ice accretion will be referred to as dry ice growth, and is characteristic of rime ice formations at low temperatures.

Figure 3-2 illustrates the behaviour of the ultrasonic echo signal received during dry ice growth. The echo waveform simply translates in time as the ice thickness, and hence pulse-echo time, increase. The rate at which the echo signal translates is thus proportional to the ice accretion rate. This simple translation of the echo waveform is a result of the extremely brief time taken for the impinging droplets to freeze. The ice surface formed under these conditions is relatively smooth, and thus a well-defined echo waveform with a narrow echo width is typically received, as indicated in the figure.

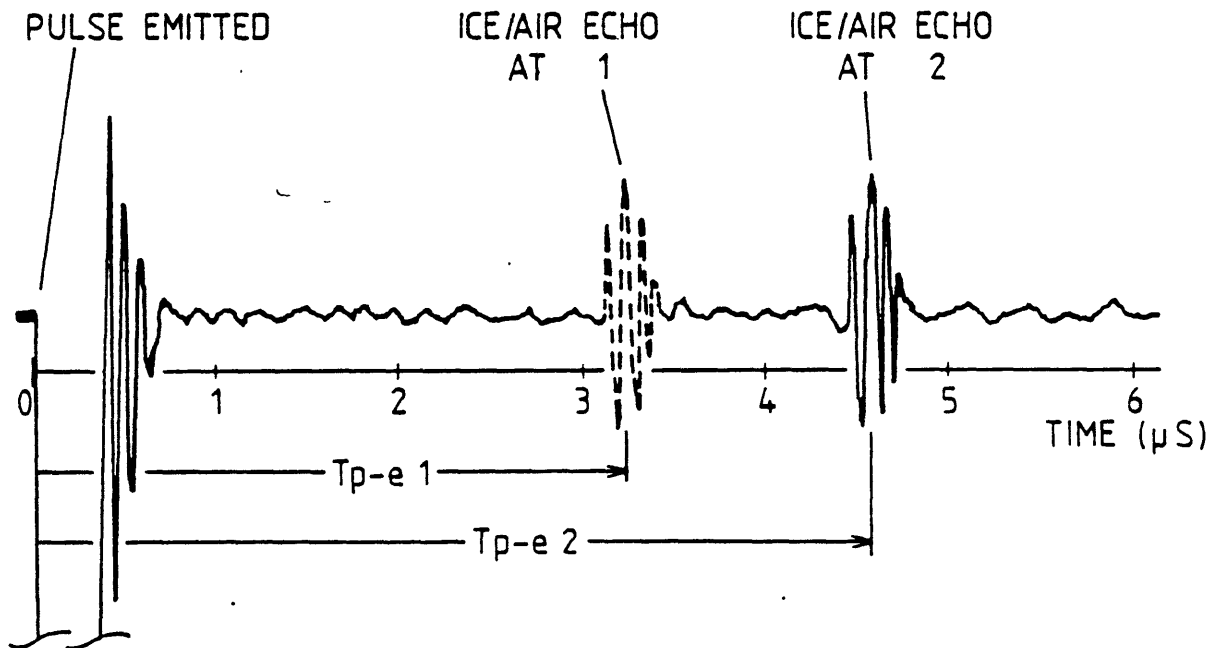
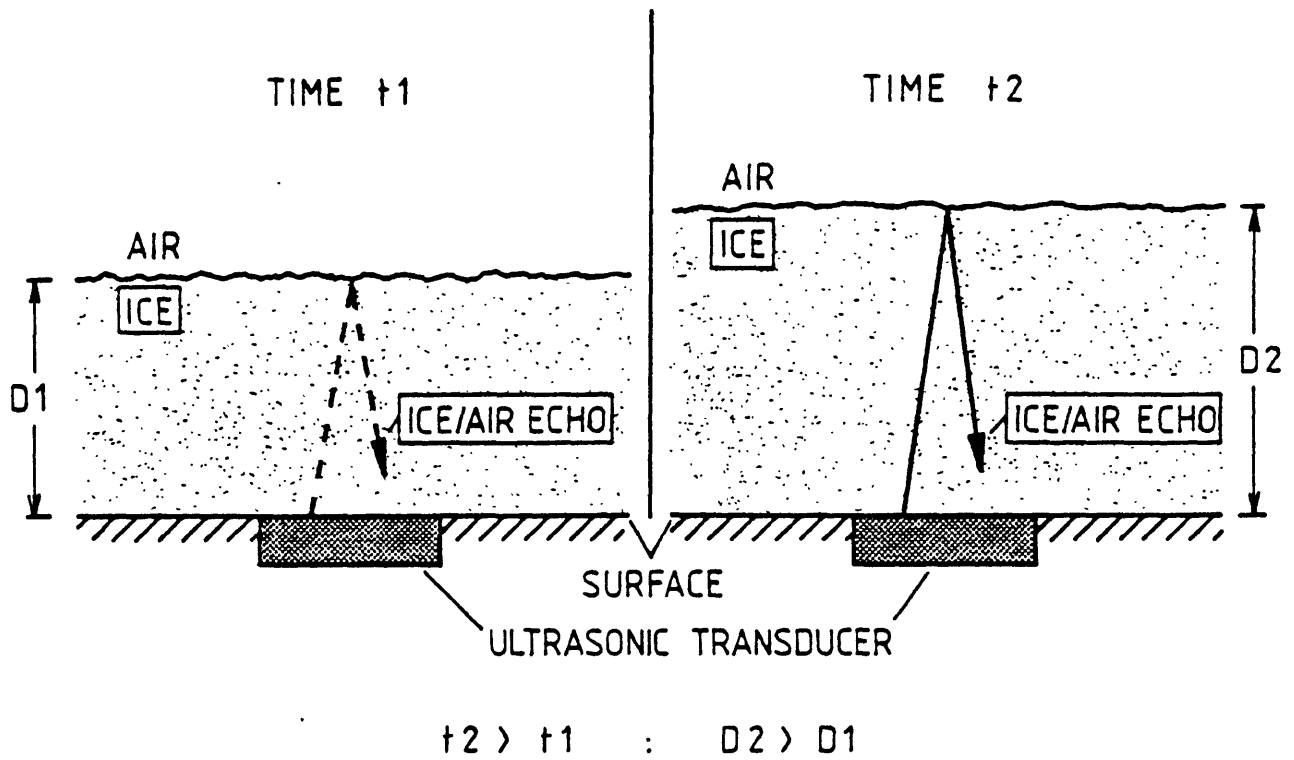


Fig. 3-2 Ultrasonic signal characteristics for dry ice growth.

3.3 ULTRASONIC SIGNAL CHARACTERISTICS FOR WET ICE GROWTH

If the heat transfer from the accreting surface is insufficient to completely freeze all the impinging droplets, the freezing fraction is less than unity and liquid water will be present on the ice surface. This form of ice accretion will be referred to as wet ice growth, and is characteristic of glaze and mixed ice formation at ambient temperatures just below 0°C.

During wet ice growth the ice surface is covered, at least partially, by a thin liquid layer. The emitted ultrasonic pulse thus encounters two separate interfaces, as shown in figure 3-3. The first interface encountered by the outgoing pulse is that between the ice and the water lying on the ice surface. This interface will be referred to as the ice/water interface. The other interface encountered is that between the liquid water and the ambient air, the water/air interface. Two echo signals are therefore received; the first from the ice/water interface, and a second, later echo from the water/air interface.

The first echoes received (labelled "A" to "B" in figure 3-3), are from the ice/water interface, and have a characteristically broader echo width than that received

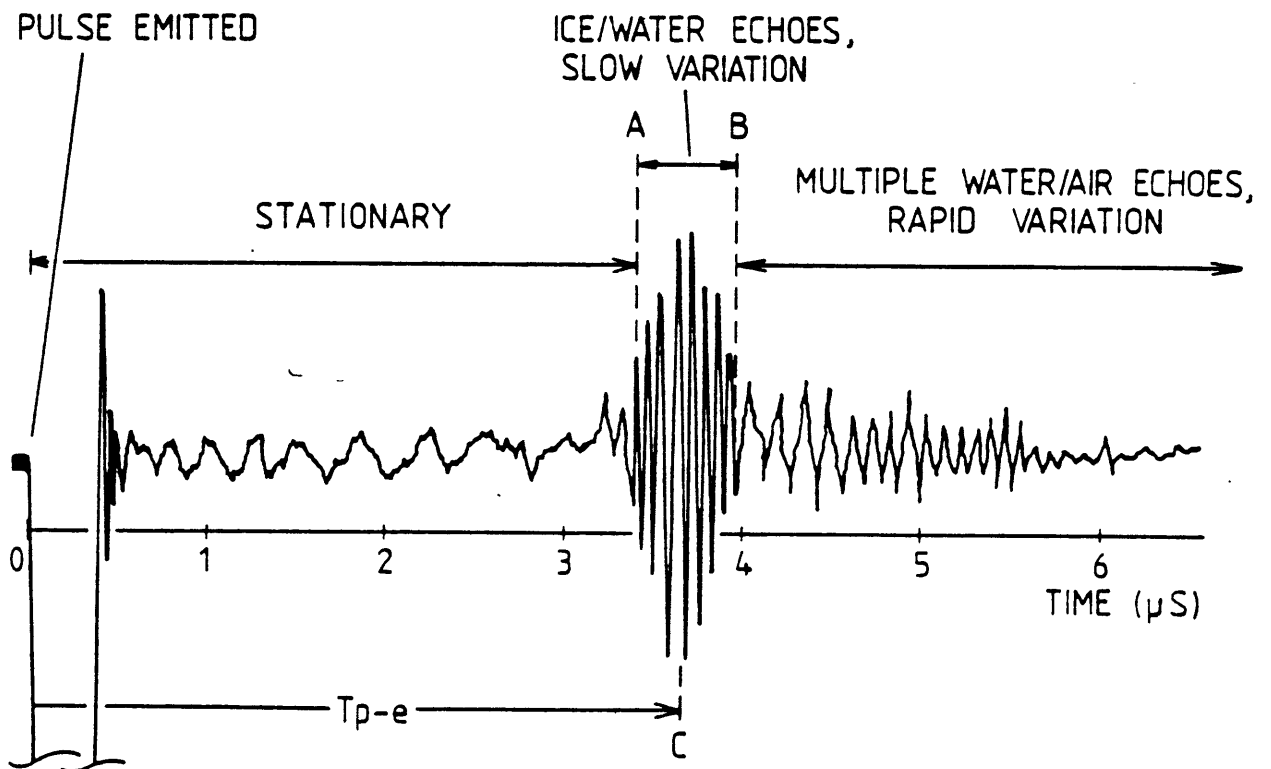
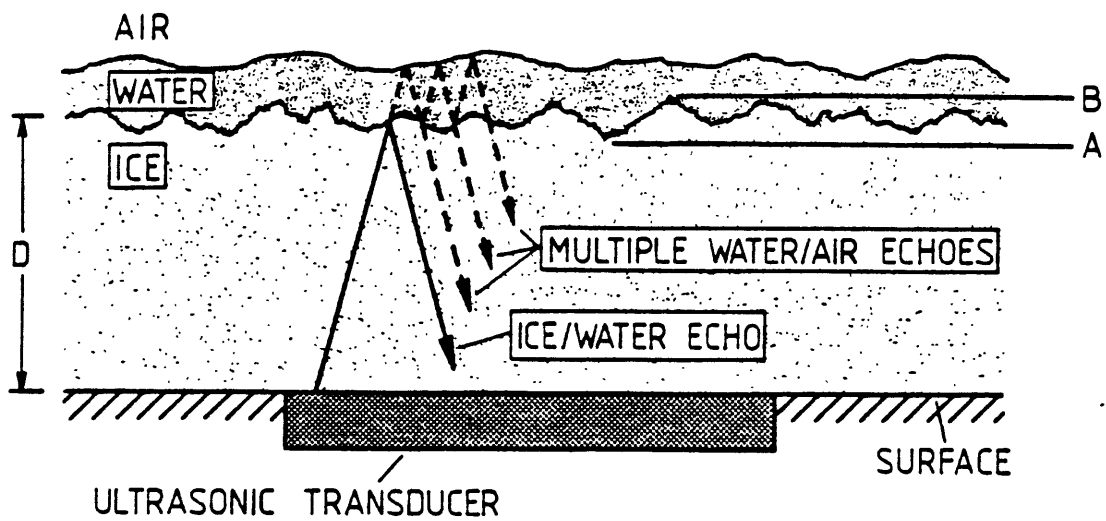


Fig. 3-3 Ultrasonic signal characteristics for wet ice growth.

during rime, or dry, ice growth. This broad echo width is due to the rougher ice surface characteristic of glaze, or wet, ice growth.

The rougher ice surface typically observed during wet ice growth is illustrated in figure 3-3. The variations in ice thickness (exaggerated for clarity), over the area of the transducer* increase the width of the received echo. The start of the echo return from the ice surface, labelled "A" in figure 3-3, represents the minimum ice thickness over the transducer. The last echo return from the ice surface, labelled "B", corresponds to the maximum ice thickness over the transducer. The central region of the ice surface echo, "C", was used as representative of the average local ice thickness for all the test results presented.

As in the dry growth case, these ice/water echoes translate in time as liquid freezes at the interface and the ice thickness increases. Now however, the freezing process is no longer "instantaneous", and the detailed shape of the ice/water echoes slowly varies as liquid freezes over the transducer.

*The ultrasonic transducers used typically had diameters of approximately 0.65 or 1.30 cm.

Following these ice/water echoes, many multiple echoes are received from the water/air interface, as illustrated in figure 3-3.

Since the water/air interface is effectively a perfect reflector, the pulse energy initially transmitted into the liquid is repeatedly reflected within this thin liquid layer (see figure 3-3), thus producing many multiple echoes. The shape of these multiple echoes constantly varies as the instantaneous local thickness and surface orientation of the liquid changes as a result of distortion by the impinging droplets and the external flowfield. Unlike the echoes received from the ice/water interface, the water/air echoes vary rapidly in time, allowing the presence of liquid on the icing surface to be easily discerned.

While the shape of the echoes received from the two interfaces both vary in time, these variations occur at different rates due to the different physical processes involved at the respective interfaces. The relatively slow variation of the first echoes received, from the ice/water interface, corresponds to a characteristic freezing time at that interface; while the much more rapid variation of the multiple echoes received from the water/air surface represents the rate at which the liquid surface is distorted by droplet impacts and aerodynamic forces.

3.4 SUMMARY

Ultrasonic pulse-echo techniques can be used to accurately and continuously measure ice thickness on an accreting surface. During wet ice growth, liquid on the ice surface produces a constantly distorting, reflective interface for the emitted ultrasonic pulse. As a result, the echoes received during wet growth display a rapid time variation that is absent when the ice surface is dry. Hence by examining the time variation of the echo signals received, the presence or absence of liquid on the ice surface may be clearly discerned.

Chapter 4

ICING OF A CYLINDER DURING ARTIFICIAL ICING CONDITIONS

4.1 OVERVIEW

This chapter describes experimental measurements of ice growth on a cylinder exposed to artificial icing conditions produced in the NASA Lewis Icing Research Tunnel. Ice thickness and surface condition (wet or dry) were measured for a variety of icing cloud conditions, using ultrasonic pulse-echo techniques. Sections 4.2 and 4.3 describe the experimental apparatus used and the cylinder installation and test procedure in the icing wind tunnel. Section 4.4 presents experimental results for different icing cloud conditions. Results are presented in the form of ice thickness versus icing time and ice accretion rate versus cloud temperature. The effects of exposure time and cloud temperature are compared and discussed. Ice accretion rates measured during wet and dry ice growth are used to infer freezing fractions for the stagnation region, and to examine liquid runback along the ice surface.

In Section 4.5, the ultrasonically measured wet or dry ice surface conditions and corresponding accretion rates are used to compare a series of assumed heat transfer

coefficients for the icing surface. The heat transfer coefficients used are the experimental measurements of Van Fossen et al., for a cylinder with a known surface roughness exposed to crossflow at different freestream turbulence levels¹². Results are presented in the form of wet/dry "threshold" curves for each heat transfer model, plotted together with experimentally observed wet and dry ice growth cases. Section 4.6 summarizes the important features of the experimentally observed ice growth behaviour in the Icing Research Tunnel. Conclusions about the heat transfer magnitude over the icing surface, based on the analysis in Section 4.5, are also presented.

4.2 EXPERIMENTAL APPARATUS

Figure 4-1 illustrates schematically the apparatus and experimental configuration used for these tests. The equipment employed consisted of four main components, listed below.

- (1) A cylinder instrumented with small ultrasonic transducers flush with the cylinder surface.
- (2) A pulser/receiver unit to drive the transducers.
- (3) An oscilloscope to display the pulse-echo signal.

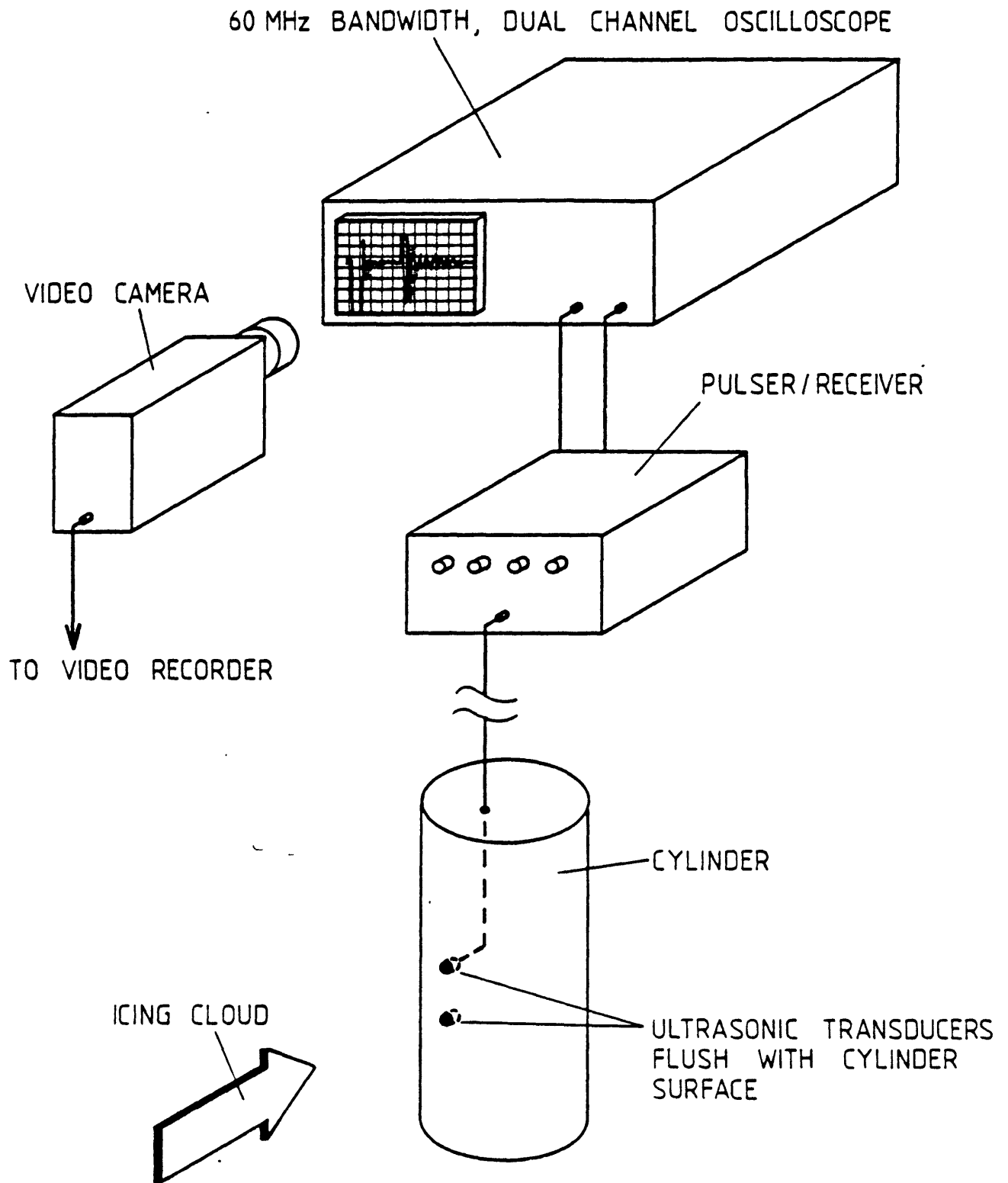


Fig. 4-1 Schematic of experimental apparatus configuration.

- (4) A video camera to record the pulse-echo signal displayed on the oscilloscope screen.

The test cylinder had a diameter of 10.2 cm (4.0"), and was approximately 30.5 cm (12.0") long. The cylinder material was aluminium with a wall thickness of 6.3 mm (0.25"). The cylinder stagnation line was instrumented with four ultrasonic transducers, mounted near the cylinder mid-section. All the transducers had plane, circular emitting faces and were mounted with the emitting face flush with the cylinder surface. The diameter of the transducer elements was either 6.3 or 12.7 mm (0.25" or 0.5"). The transducers were all of the broadband, heavily damped type, with center frequencies of either 1 MHz, 2.25 MHz or 5 MHz. The 5 MHz transducers provided the highest resolution, due to the shorter wavelength, and all results shown are for 5 MHz transducers.

The pulser/receiver unit provided the electrical signals necessary to generate the ultrasonic pulse and amplify the return echo received by the transducer. An oscilloscope was used to display the pulse-echo waveform. A high bandwidth (60 MHz) oscilloscope was required due to the 5 MHz centre frequency of the transducers. In order to obtain a permanent record of the time dependent pulse-echo waveform, a video camera was used to film the oscilloscope screen. A digital

clock within the camera's field of view allowed the cylinder exposure time to be simultaneously recorded.

4.3 ICING RESEARCH TUNNEL INSTALLATION AND TEST PROCEDURE

4.3.1 THE ICING RESEARCH TUNNEL

The icing wind tunnel used was the NASA Lewis Research Center's Icing Research Tunnel (IRT). The Icing Research Tunnel is a closed loop, refrigerated wind tunnel capable of generating airspeeds up to 134 m/s (300mph) over a test section area 1.83 m high and 2.74 m wide (6' x 9'). A large refrigeration plant allows total air temperatures as low as -34°C to be achieved. A spray bar system upstream of the test section is used to produce the icing cloud. The cloud liquid water content can be varied from 0.3 to 3.0 g/m³ and the droplet median volume diameter from 10 to 40 microns.

Although the icing cloud fills the entire test section, the cloud liquid water content varies over the test section area. A central region of nearly constant liquid water content exists, and is referred to as the "calibrated cloud" (see figure 4-2). The calibrated cloud region is approximately 0.6 m (2') high and 1.5 m (5') wide. The

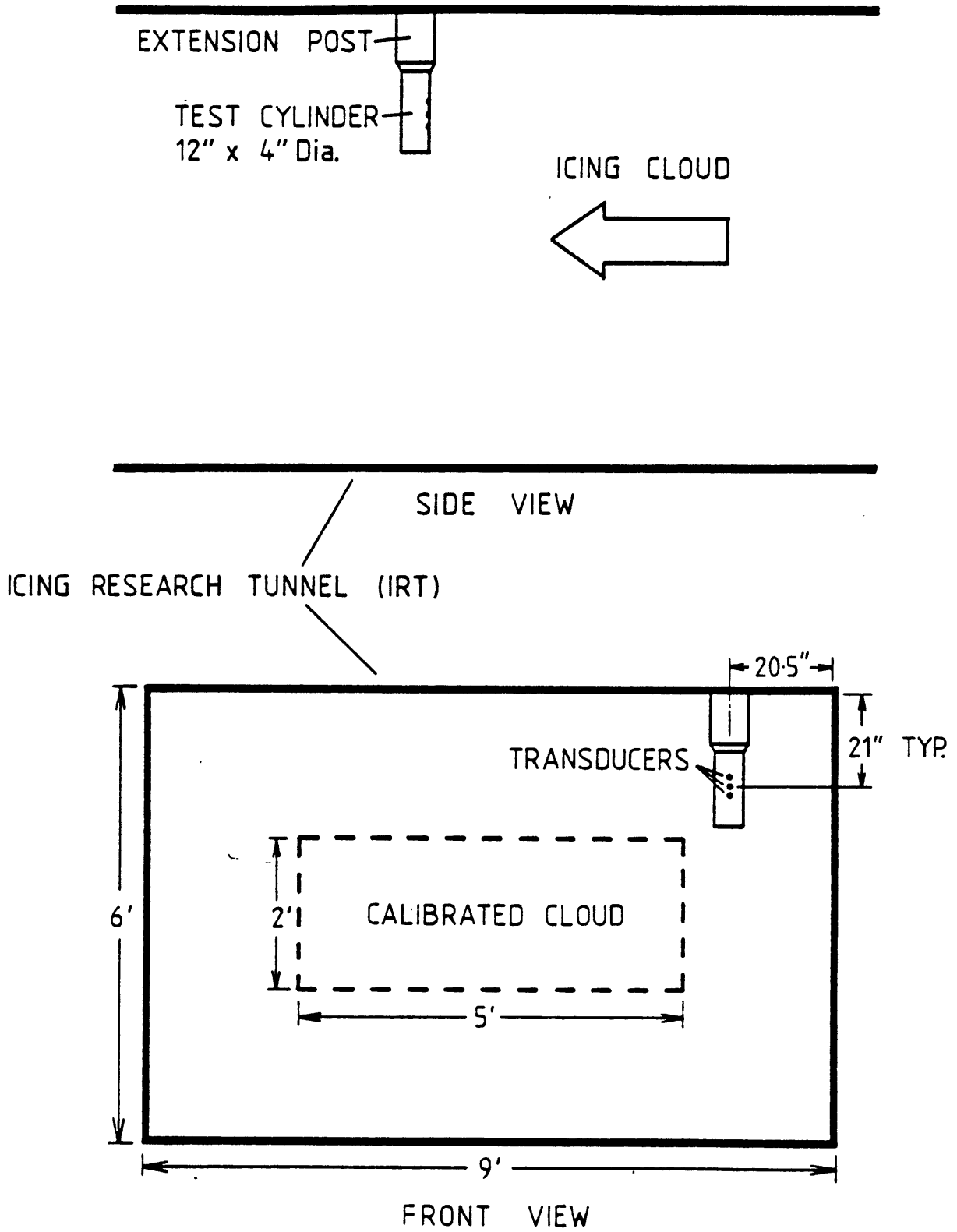


Fig. 4-2 Cylinder installation in Icing Research Tunnel.

liquid water content outside this region decreases, and is near zero close to the tunnel walls.

4.3.2 CYLINDER INSTALLATION

The test cylinder installation in the Icing Research Tunnel is shown in figures 4-2 and 4-3. The cylinder was suspended vertically on an extension post mounted in the roof of the IRT. However, in order to allow another experiment unobstructed access to the icing cloud, the cylinder did not fully extend into the calibrated region of the icing cloud. As a result, the liquid water content at the cylinder location was lower than that in the calibrated region. The freestream velocity, temperature, and droplet size distribution at the cylinder location were assumed to be equal to the calibrated region values¹³. Figure 4-3 is a photograph of the cylinder installation in the IRT test section, looking upstream. The test cylinder is in the top left hand corner of the photograph. The airfoil in the centre of the photograph occupies the calibrated region of the icing cloud, produced by the spray bar system visible in the background.

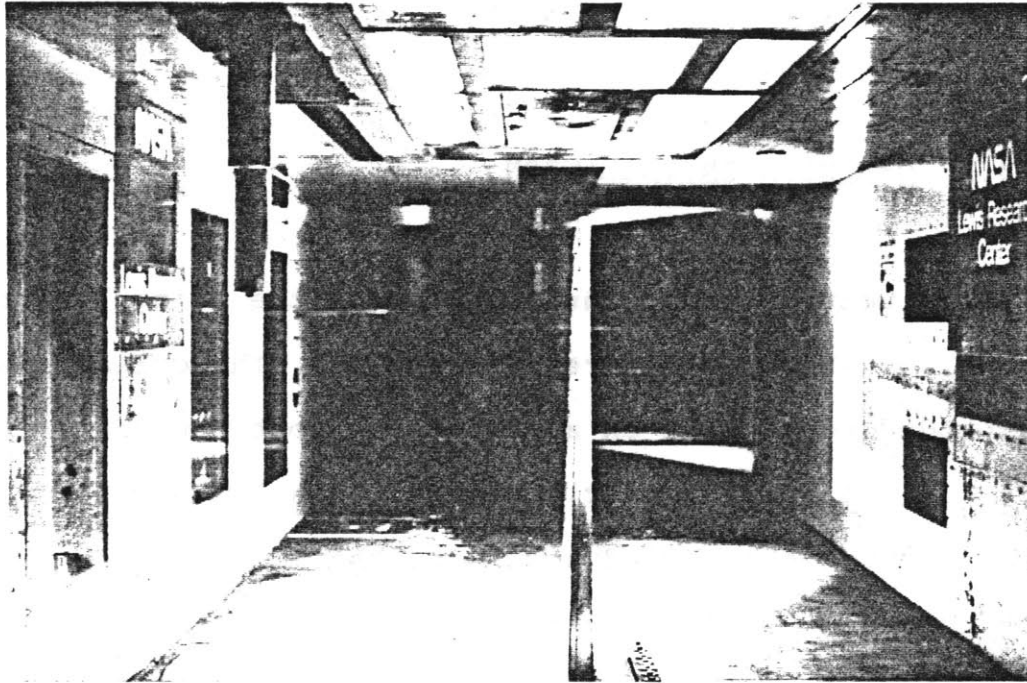


Fig. 4-3 Photograph of cylinder installation in IRT test section (looking upstream).

4.3.3 TEST PROCEDURE

The test procedure for each different icing condition simulated was as follows. With the water spray off, and the test section airspeed set, the tunnel temperature was lowered to the desired value. Once the tunnel temperature had stabilized, the water spray system was turned on in order to produce the icing cloud. The cloud liquid water content and median volume diameter were set by the spray bar

water flow rate and injection pressures.

The pulse-echo signals from the transducers mounted in the cylinder were recorded by the video camera as ice accreted on the cylinder. Typically the spray system was activated for a six minute period, after which it was turned off. Constant icing conditions were maintained throughout each exposure, or run. At the completion of each run, the iced diameter of the cylinder was measured at each transducer location, using a pair of outside calipers. The ice thickness over the transducers was inferred from this "mechanical" measurement. The cylinder was then completely de-iced in preparation for the next run.

4.3.4 TEST ICING CONDITIONS

Ice growth was measured using the ultrasonic pulse-echo technique for fifteen different icing cloud conditions, ranging from glaze to rime icing conditions. Table 4-1 lists the range of icing cloud characteristics for these tests.

Cloud Temperature (°C)	LWC* (g/m ³)	MVD (Microns)	Freestream Velocity (mph)
-4.0 to -28.6	0.38 to 1.54	12.0 to 20.5	110 to 230

Table 4-1 Range of icing conditions tested for cylinder in the Icing Research Tunnel.

*(Estimated from dry ice growth rate, all other values shown are calibrated cloud values.)

4.4 EXPERIMENTAL MEASUREMENTS OF ICE GROWTH DURING ARTIFICIAL ICING CONDITIONS

In this section, ultrasonic measurements of ice thickness and ice accretion rate are presented and compared for different icing conditions. The ice accretion rate on the stagnation line is shown to be a maximum for dry ice growth conditions, and to decrease when the ice surface becomes wet. This experimentally observed behaviour suggests that, under certain icing conditions, liquid runback from the stagnation region does occur.

4.4.1 COMPARISON OF ICE GROWTH DURING HEAVY AND LIGHT ICING CONDITIONS

Figures 4-4 and 4-5 are plots of ice thickness, measured with the ultrasonic system, versus exposure time. Ice growth is shown at three different icing cloud temperatures for "heavy" and "light" icing conditions.

The heavy icing conditions (figure 4-4) represent an icing cloud with a high liquid water content, 0.77 g/m^3 , and a relatively large median volume drop diameter of 20 microns. The light icing conditions (figure 4-5) represent an icing cloud with a lower liquid water content and smaller droplet size. The liquid water content for the light icing conditions, 0.38 g/m^3 , is half the heavy icing value, and the median volume drop diameter is reduced from 20 microns to 12 microns. The freestream velocity is 103 m/s (230mph) for both the heavy and light icing conditions.

Since the test cylinder was located outside the calibrated cloud (see Section 4.3), the values given for the icing cloud conditions are approximate. In particular, the liquid water content at the cylinder location was estimated to be 64% of the calibrated cloud value. This estimate is based on the cylinder ice accretion rates measured for dry ice growth; the experimental data used to derive this corrected liquid water content is contained in Appendix B.

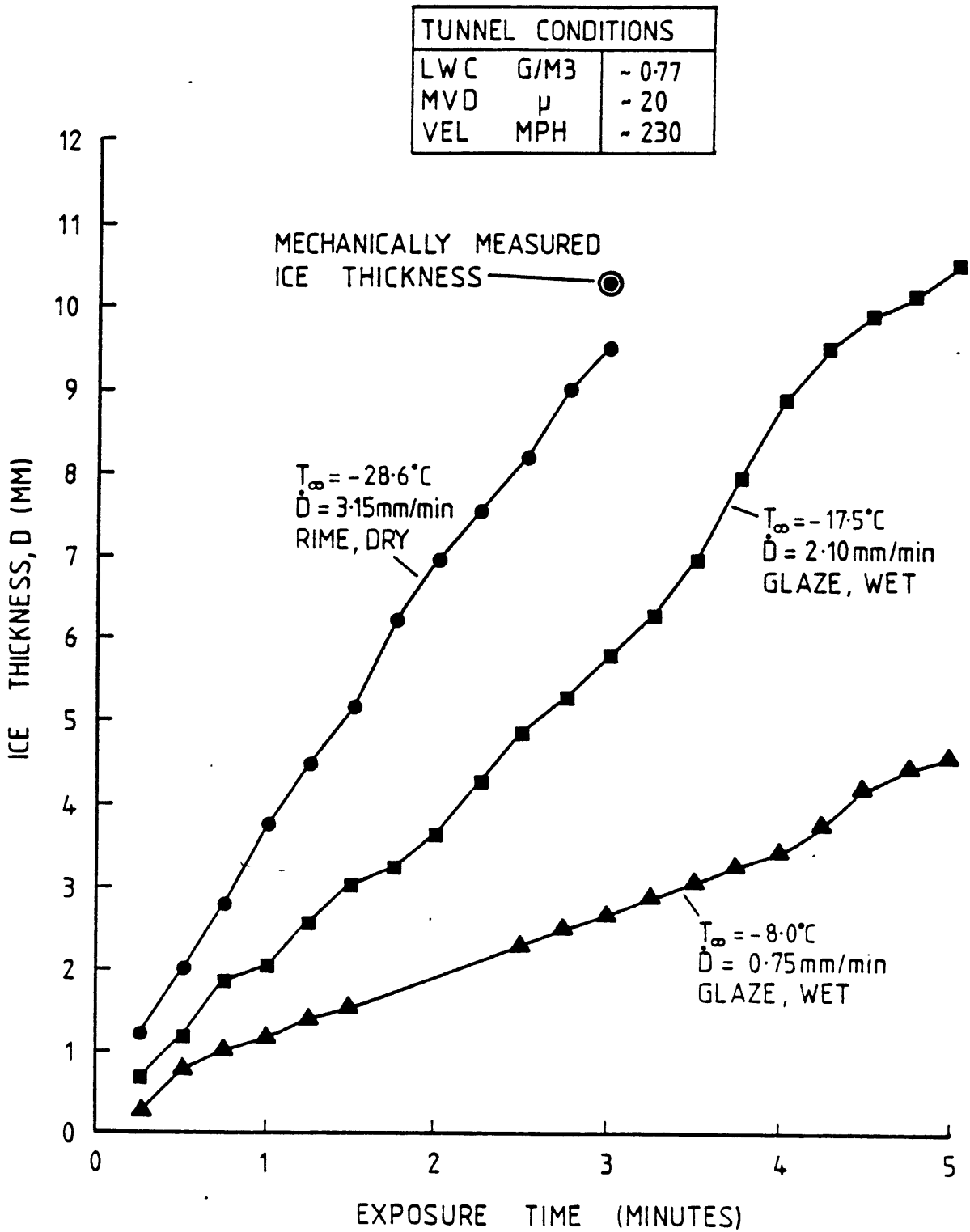


Fig. 4-4 Ice growth measured for "heavy" icing conditions.

TUNNEL CONDITIONS		
LWC	G/M3	~0.38
MVD	μ	-12
VEL	MPH	-230

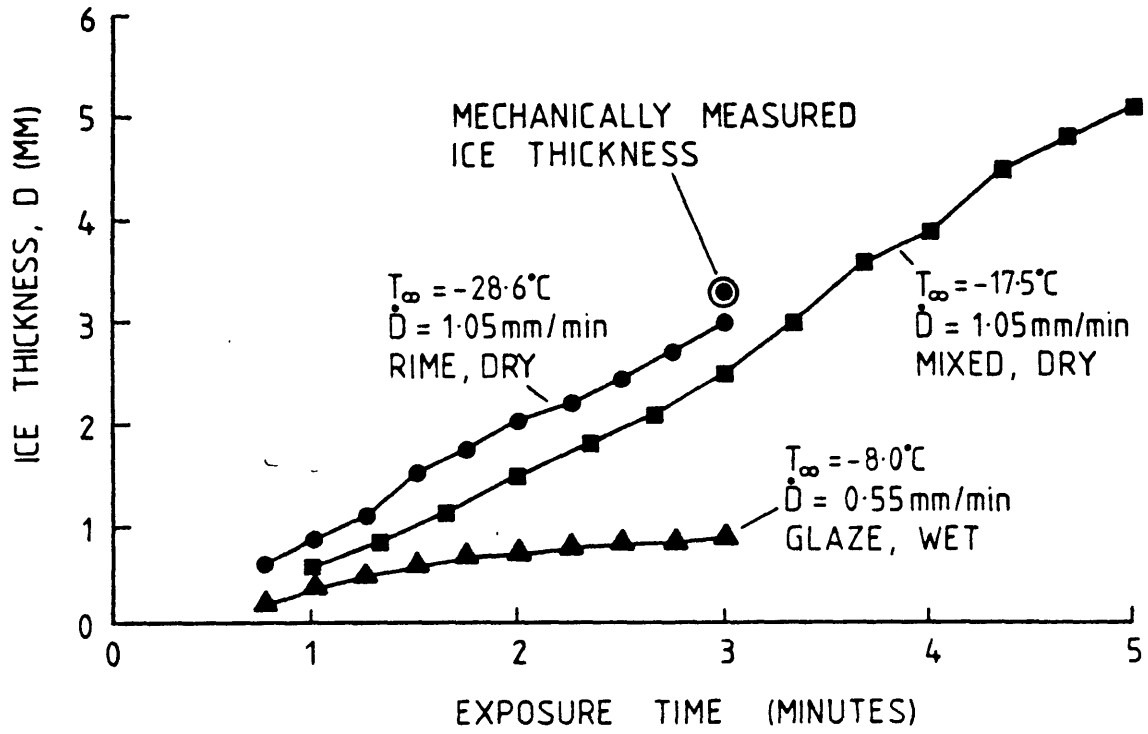


Fig. 4-5 Ice growth measured for "light" icing conditions.

As stated earlier, the freestream velocity, cloud temperature and droplet size distribution for the cylinder location were assumed to be approximately equal to the calibrated cloud values.

Figures 4-4 and 4-5 show the ultrasonically measured ice growth on the cylinder stagnation line for three different cloud temperatures, -8.0°C , -17.5°C and -28.6°C . The type of ice growth occurring, wet or dry, is also indicated for each exposure. The ultrasonic echo characteristics from the accreting ice surface were used to determine if the growth was wet or dry, as explained in Chapter 3. The caliper measured ice thickness at the completion of each exposure is also shown, if known. These mechanical measurements are seen to be in close agreement (± 0.5 mm) with the ultrasonically measured thicknesses, and confirm the accuracy of the pulse-echo measurement technique. The important features of the ice growth behaviour for the heavy and light icing conditions shown are discussed below.

i) EFFECT OF EXPOSURE TIME ON ICING RATE

The ice growth plots in figures 4-4 and 4-5 all show a relatively linear increase in ice thickness with exposure time; the ice accretion rate, given by the slope of the ice thickness curve, is therefore approximately constant

throughout each exposure. These constant accretion rates indicate that the icing process for each exposure was essentially steady-state, i.e. for the exposure times shown (3-5 min.), the ice accretion on the cylinder did not significantly change the flow-field and local collection efficiency in the stagnation region.

The ice accretion rate, \dot{D} , for an icing surface was derived in Chapter 2, and is given by,

$$\dot{D} = n\beta W V_{\infty} / \rho_{ice} \quad [2.20]$$

Where n is the local freezing fraction, β is the local collection efficiency and W is the cloud liquid water content. Both the cloud liquid water content and the freestream velocity, V_{∞} , were held constant throughout each exposure in the Icing Research Tunnel. Thus, assuming a constant ice density¹⁴, the ice accretion rate for the cylinder in the IRT is expected to be proportional to the product of the freezing fraction and the local collection efficiency,

$$\dot{D} \propto n\beta \quad (4.1)$$

For the dry ice growth cases observed in the IRT, the ice accretion rate is simply proportional to the local collection efficiency, since the freezing fraction is unity

for dry growth. The constant dry growth accretion rates measured (see figures 4-4 and 4-5) therefore imply a constant local collection efficiency on the cylinder stagnation line for those exposures. Thus it can be concluded that, for each of the dry growth exposures, the flowfield in the stagnation region of the cylinder was not significantly altered by the accreted ice.

The ice accretion rates observed on the cylinder stagnation line when the surface was wet also appear to be approximately constant throughout most of the exposure. However, there are some initial transient variations in the wet growth accretion rates. These variations are possibly due to a change in the local heat transfer coefficient, caused by increased surface roughness due to the accreted ice*. Note that for dry growth cases, transient variations in the local heat transfer coefficient will not produce corresponding variations in the ice accretion rate if the heat transfer magnitude is always sufficient to freeze all of the impinging droplets.

*Another possible cause of these initial variations in accretion rate are fluctuations in the tunnel liquid water content when the spray system is first turned on.

Following these initial variations, the accretion rates measured for the wet growth cases remain approximately constant for several minutes. During this "steady-state" period it thus appears that both the local collection efficiency, β , and the freezing fraction, n , remain substantially constant. This in turn implies that the flowfield and local heat transfer coefficient for the stagnation region were not appreciably altered as the ice accreted during this steady growth rate period.

Finally, the accretion rates for the wet growth cases in heavy icing conditions (-8.0°C and -17.5°C), both show an increase towards the end of the exposure. This increase in accretion rate is most likely an indication that the accreted ice has started to significantly alter the original flowfield.

ii) COMPARISON OF ICE ACCRETION RATES FOR HEAVY AND LIGHT ICING CONDITIONS

As discussed in the previous section, the ice accretion rates for each icing condition were observed to be relatively constant with exposure time. Table 4-2 summarizes all of the ice accretion rates measured for the heavy and light icing cases. In each case these are the average accretion rates for the steady-state growth period during

the exposure.

Icing Cloud	Cloud Temperature		
	-28.6°C	-17.5°C	-8.0°C
Heavy	3.15	2.10	0.75
Light	1.05	1.05	0.55

Table 4-2 Summary of ice accretion rates (in mm/min) measured for heavy and light icing conditions.

At each cloud temperature, the accretion rates measured under the heavy icing conditions are uniformly greater than those for the light icing conditions. For example, at the coldest cloud temperature, -28.6°C, the heavy icing accretion rate is 3.15 mm/min, while for the light icing conditions the accretion rate is only 1.05 mm/min.

The higher accretion rates at each cloud temperature for the heavy icing conditions are due to the greater impinging droplet mass flux under these conditions. The droplet mass flux per unit time impinging on the stagnation line of the cylinder, $\dot{M}''_{\text{impinging}}$, is given by,

$$\dot{M}''_{\text{impinging}} = \beta W V_{\infty} \quad [2.3]$$

The cloud liquid water content, W , for the heavy icing conditions, 0.77 g/m^3 , was twice that for the light icing conditions; and the cloud median volume diameter was 20 microns versus 12 microns for the light icing conditions. The local collection efficiency, β , is thus greater for the heavy icing conditions as a result of the larger cloud droplet diameter. The local collection efficiency was calculated (from Ref. 15) to be 0.61 for the heavy icing conditions and 0.40 for the light icing conditions. The droplet mass fluxes impinging on the cylinder stagnation line can thus be compared as,

$$\begin{aligned} \frac{\dot{M}''_{\text{impinging, heavy}}}{\dot{M}''_{\text{impinging, light}}} &= \frac{(\beta W V_{\infty})_{\text{heavy}}}{(\beta W V_{\infty})_{\text{light}}} \\ &= \frac{(0.61)(0.77)(102.8)}{(0.40)(0.38)(102.8)} \\ &= 3.05 \end{aligned} \tag{4.2}$$

This result is in excellent agreement with the experimentally measured dry growth accretion rates. For dry growth, the accretion rate is,

$$D = \dot{M}''_{\text{ice}} / \rho_{\text{ice}} = \beta W V_{\infty} / \rho_{\text{ice}} \tag{2.4}$$

Thus the measured rates of 3.15 mm/min and 1.05 mm/min for

the heavy and light icing conditions imply a droplet mass flux ratio of $3.15/1.05 = 3.0$, while the calculated value (eq. 4.2) is 3.05. This result therefore supports the assumption that the droplet size distribution at the cylinder location was not significantly different from that in the calibrated cloud region.

Referring again to Table 4-2, it can be seen that as the cloud temperature is increased, the ratio of the heavy and light icing growth rates decreases from the dry growth ratio of 3.0 at -28.6°C . For example, at -17.5°C the accretion rate has decreased from 3.15 mm/min to 2.10 mm/min for the heavy icing conditions, while the accretion rate for the light icing conditions is unchanged at 1.05 mm/min. The accretion rate for the heavy icing case has decreased because the ice growth is no longer dry at this warmer cloud temperature. These changes in accretion rate with cloud temperature, and the transition between dry and wet ice growth, are discussed in the next section.

iii) EFFECT OF CLOUD TEMPERATURE ON ICE ACCRETION RATE - WET AND DRY ICE GROWTH

The change in the stagnation region accretion rate, as a function of the cloud temperature and ambient icing conditions, is discussed in this section. These experimental

measurements of wet and dry ice growth, and the corresponding variations in accretion rate, form the basis for the comparison of different heat transfer models presented in Section 4.5. In addition, the observed accretion rate behaviour suggests that liquid runback from the stagnation region does indeed occur, at least during the initial icing period.

Figure 4-6 is a plot of average ice accretion rate versus cloud temperature for all of the heavy and light icing conditions tested. The type of ice growth occurring for each condition, wet or dry, is also indicated. In all cases the ultrasonic echo characteristics from the accreting ice surface were used to determine if the ice growth was wet or dry.

For both the heavy and light icing conditions, at the warmest cloud temperature, -8°C , the ice surface is wet and the accretion rate is low. However as the temperature of the icing cloud is progressively reduced, the accretion rate is observed to increase. Finally, when the cloud temperature is cold enough, all the impinging droplets are frozen on impact, the ice surface is dry, and the accretion rate is a maximum. Further decreases in cloud temperature beyond this point do not alter the accretion rate.

TUNNEL CONDITIONS		
	Heavy Icing	Light Icing
LWC g/m ³	0.77	0.38
MVD μ	20	12
VEL mph	230	230
Symbol	■	●

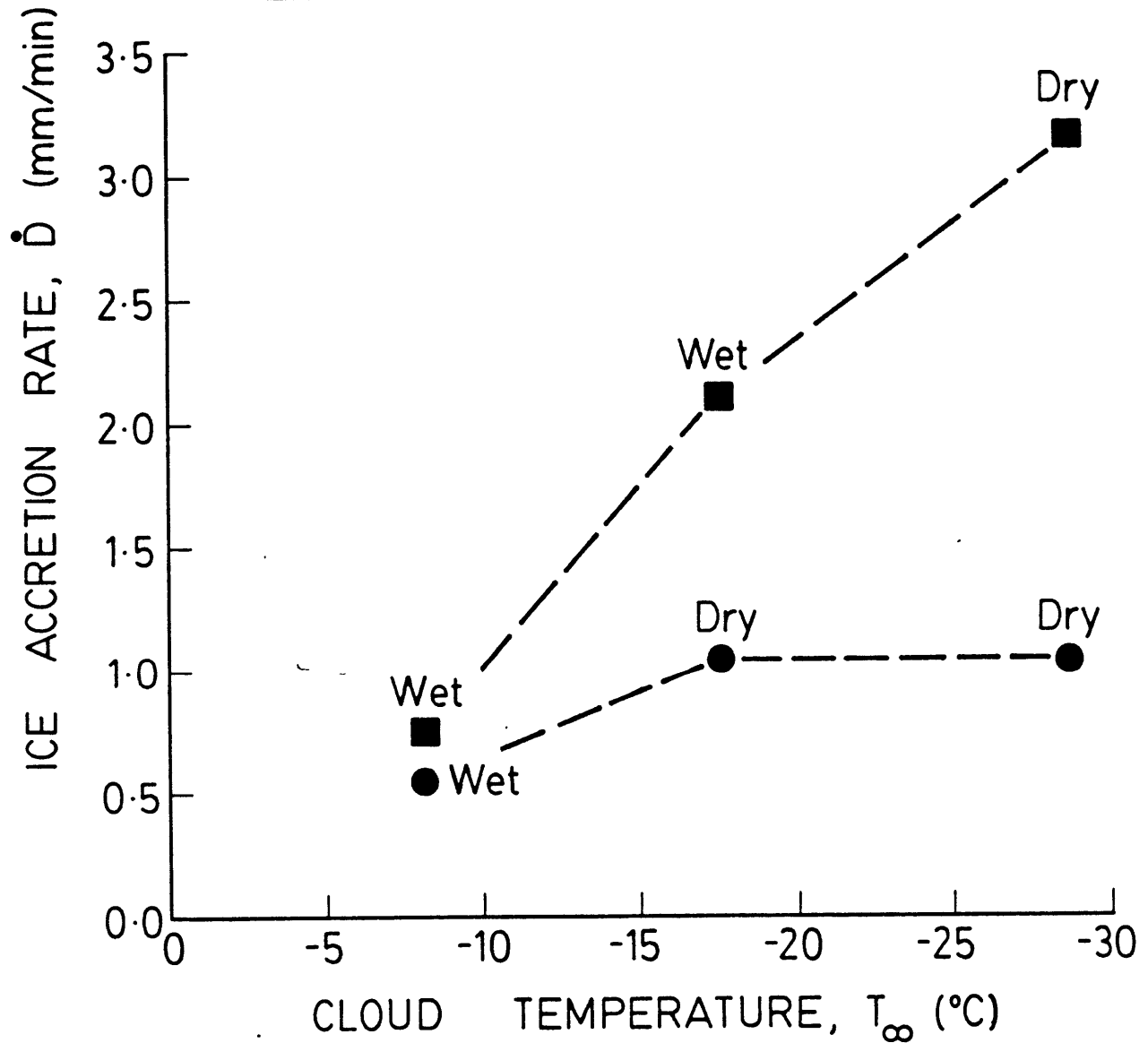


Fig. 4-6 Average ice accretion rate vs. cloud temperature for "heavy" and "light" icing conditions in the Icing Research Tunnel.

For example, for the light icing conditions, at -8°C , the accretion rate is 0.55 mm/min , and the growth is wet; at -17.5°C the ice growth is dry and the accretion rate has increased to 1.05 mm/min . When the cloud temperature is further reduced, to -28.6°C , the rate remains 1.05 mm/min . Thus, for these light icing conditions, the transition from wet to dry ice growth occurs between -8°C and -17.5°C .

For the heavy icing conditions, the accretion rates shown in figure 4-6 indicate that the growth rate increased from 0.75 mm/min at -8.0°C to 2.10 mm/min at -17.5°C . However, in contrast to the light icing case, the ice growth is still wet at this temperature, due to the higher impinging mass flux per unit time. When the cloud temperature is reduced to -28.6°C , the accretion rate increases further, to 3.15 mm/min . The heat transfer from the surface at this cloud temperature is sufficient to freeze all of the impinging mass flux, and the ice growth is therefore dry.

The lower accretion rates observed during wet ice growth can be explained as follows. For wet ice growth to occur in the cylinder stagnation region, the heat transfer from the icing surface must be insufficient to completely freeze all the locally impinging water droplets. As a result, liquid water must form on the ice surface. The ice accretion rate

for the stagnation region, \dot{D} , is then given by,

$$\dot{D} = n\beta W V_{\infty} / \rho_{ice} \quad [2.20]$$

Where n is the freezing fraction for the stagnation region, and β the local collection efficiency. The freezing fraction must lie between zero and unity for wet ice growth, and represents the incomplete freezing of the locally impinging droplet mass flux per unit time, $\beta W V_{\infty}$. Since the freezing fraction is less than unity during wet ice growth, the accretion rate on the stagnation line will thus be lower than the dry growth rate ($n = 1$).

For wet growth in the stagnation region, a freezing fraction of less than unity is simply a result of mass conservation: a fraction, n , of the impinging droplet mass flux freezes and forms ice, and the remaining fraction, $1-n$, produces liquid on the ice surface. Note that this argument does not involve any assumption about the liquid behaviour on the icing surface, e.g. runback.

The behaviour of liquid water on the icing surface during wet ice growth is not well understood, and there is little experimental data in this area. Implicit in many of the steady-state icing models used to predict ice growth is the assumption that liquid formed on the icing surface immediately flows downstream. This form of runback

assumption has recently been questioned¹⁶. However, an examination of the ultrasonic echo characteristics from the icing surface, and the corresponding accretion rates, shows that liquid runback probably does occur during the initial icing period.

iv) LIQUID RUNBACK FROM THE STAGNATION REGION

As described in Chapter 3, ultrasonic echoes are received from both the ice/water and water/air interfaces during wet ice growth. In principle, the thickness of the liquid water on the ice surface may be determined by the same time of flight technique used to measure the ice thickness, i.e. by measuring the time interval between the ice/water echo return and the water/air return. Due to distortion of the liquid surface by impinging droplets and aerodynamic forces, it is difficult in practice to accurately measure the liquid thickness using this technique. However, water thicknesses on the order of a millimeter can be discerned, even when this type of surface distortion is present. Any significant accumulation of unfrozen liquid in the stagnation region (>1 mm) should therefore be discernible from the ultrasonic echo signals recorded.

From figure 4-6, the accretion rate measured for the heavy icing case at -8.0°C is 0.75 mm/min , and the ice surface is observed to be wet. At -28.6°C the surface is dry, as indicated by the ultrasonic echo characteristics, and the accretion rate is 3.15 mm/min . Since the freezing fraction is unity for dry growth, the freezing fraction for the wet growth case at -8°C can be expressed as the ratio of the wet growth rate (eq. 2.20) to the dry growth rate, i.e.,

$$\begin{aligned}
 n &= \frac{\dot{D}_{\text{wet}}}{\dot{D}_{\text{dry}}} = \frac{0.75\text{ mm/min}}{3.15\text{ mm/min}} \\
 &= 0.24 \qquad \qquad \qquad (4.3)
 \end{aligned}$$

Equation 4.3 states that, for the heavy icing conditions, and a cloud temperature of -8.0°C , the heat transfer from the stagnation region of the cylinder is only sufficient to freeze 24% of the droplet mass flux impinging in the stagnation area. Thus 76% of the mass flux impinging forms liquid on the ice surface. If all of this liquid remained in the stagnation region, and did not flow downstream over the ice surface, the water thickness would be expected to increase at a steady-state rate of 2.2 mm/min .

Referring back to figure 4-4, it can be seen that the ice accretion rate for this icing condition (-8°C) remains

constant for over three minutes. With little, or no liquid runback from the stagnation region, the water thickness would therefore be several millimeters towards the end of the exposure. No liquid thicknesses on the order of a millimeter or more were detected from the ultrasonic measurements during any of the tests conducted in the Icing Research Tunnel. Therefore, based on the lower ice accretion rates measured during wet growth, and the absence of any significant accumulation of water in the stagnation region, it appears almost certain that runback from the stagnation region did occur.

4.5 COMPARISON OF DIFFERENT LOCAL CONVECTIVE HEAT TRANSFER MODELS FOR AN ICING SURFACE IN THE ICING RESEARCH TUNNEL

4.5.1 STAGNATION REGION HEAT TRANSFER AND ICE SHAPE PREDICTION

A clear understanding of the heat transfer magnitude in the stagnation region is essential for accurate ice shape prediction by quasi steady-state icing models.

These models assume that all the impinging liquid not frozen in the stagnation region flows downstream into adjacent control volumes (see figure 2-2 for control volume definition). Therefore, errors in the assumed stagnation region heat transfer coefficient may significantly affect the calculated mass flux distribution around the body during wet growth. If, for example, the stagnation region heat transfer coefficient used is lower than the "actual" value, then the amount of liquid runback from the stagnation region will be overpredicted during wet growth. This in turn may erroneously result in liquid runback from the adjacent control volumes, when in fact the "correct" condition is dry growth. The ice shapes predicted in such cases will be in poor agreement with the experimentally observed shapes; particularly when the feedback process inherent in the time-stepped flowfield and droplet trajectory calculations is taken into account.

4.5.2 HEAT TRANSFER COEFFICIENT MODELS FOR THE ICING SURFACE & THE EXPERIMENTAL MEASUREMENTS OF VAN FOSSEN ET AL.

In Chapter 2, a steady-state energy balance for the stagnation region was used to derive a quantity $(\beta W)_{crit}$, the "critical impinging liquid water content", relating the threshold between dry and wet ice growth to the local

convective heat transfer coefficient, h . Thus it was observed that, by measuring the locally impinging liquid water content at which the ice surface just became "wet", the heat transfer coefficient for the icing surface could be determined from the steady-state heat balance equation.

The limited time available for testing in the Icing Research Tunnel, and as a result the limited number of icing conditions tested, prevented a precise determination of the wet/dry threshold in this way. Instead, the ultrasonically measured wet and dry ice growth data are used to compare the wet and dry ice growth regimes predicted by different assumed local heat transfer coefficients in the steady-state energy balance equation.

The heat transfer coefficients compared are the experimental measurements of Van Fossen et al. of the convective heat transfer distribution about a cylinder¹². These measurements were recently conducted in support of the NASA Lewis icing research program. Heat transfer distributions were measured for both a bare cylinder and a cylinder with simulated glaze and rime ice accretions. Only the bare cylinder heat transfer data is compared here, since all of the ultrasonic wet/dry ice growth measurements are for the initial icing period, when the appropriate geometry is still that of a bare cylinder.

Four different convective heat transfer "models" for the cylinder stagnation region are compared. These models correspond to the heat transfer coefficients measured by Van Fossen et al. for the cylinder stagnation region. This "model" approach allows the relative importance of freestream turbulence and surface roughness on the heat transfer characteristics in icing conditions to be compared.

The four heat transfer coefficient models represent two different freestream turbulence levels, 0.5% and 3.5%, and either a smooth or rough cylinder surface. The 0.5% freestream turbulence level was the minimum achievable for the Van Fossen experiments, while the 3.5% level was selected to characterize the higher turbulence level believed to exist in the Icing Research Tunnel. A wooden cylinder, 6.6 cm in diameter, was used. To simulate a rough ice surface, the cylinder surface was also roughened with grains of sand with an average element height above the surface of 0.33 mm.

The heat transfer data in the Van Fossen study is presented in the form of power law relationships between the non-dimensionalized heat transfer coefficient, the Nusselt number, Nu , and the Reynolds number for the cylinder, Re ,

$$Nu = A Re^B \quad (4.4)$$

Where A and B are experimentally derived constants for each different heat transfer model. The power law relationships representing each of the four models considered are contained in Table 4-3 below.

Surface roughness	Freestream turbulence level	
	0.5%	3.5%
Smooth	$1.2436 \text{ Re}^{0.4774}$	$0.7636 \text{ Re}^{0.5183}$
Rough	$0.6632 \text{ Re}^{0.5533}$	$0.2460 \text{ Re}^{0.6444}$

Table 4-3 Nusselt number power law relationships, $\text{Nu} = A \text{ Re}^B$, used as models for the stagnation region heat transfer on a cylinder exposed to artificial icing conditions in the Icing Research Tunnel.
[From Van Fossen et al., NASA TM-83557.]

4.5.3 COMPARISON OF HEAT TRANSFER MODEL RESULTS

In this section the experimentally measured wet and dry ice growth data are compared with the wet and dry growth regimes predicted by the four different heat transfer models.

Figure 4-7 shows the ultrasonically measured ice growth for the six "heavy" and "light" icing conditions tested in the Icing Research Tunnel (Section 4.4). Impinging liquid water content, BW , is plotted versus cloud temperature. The impinging liquid water content on the cylinder stagnation line was determined from the ultrasonically measured dry growth accretion rates, \dot{D}_{dry} , for the heavy and light icing conditions,

$$BW = \dot{D}_{dry} \rho_{ice} / V_{\infty} \quad (4.5)$$

In all cases the ice density, ρ_{ice} , was taken to be that of the pure substance, i.e. 917 kg/m^3 . Note that since only the cloud temperature was varied, the impinging liquid water content is a constant for the heavy and light icing conditions. The impinging liquid water contents were measured to be 0.47 g/m^3 for the heavy icing conditions and 0.16 g/m^3 for the light icing conditions. The freestream velocity is 102.8 m/s (230 mph) for all six runs shown.

Also plotted in figure 4-7 are the wet/dry threshold curves calculated from the steady-state energy balance for the stagnation region (eq. 2.28). Four curves are shown, corresponding to the four different heat transfer models (0.5% and 3.5% freestream turbulence; smooth or rough surface). All of these curves were calculated for a

Cylinder Dia. = 0.102m		
Freestream Vel. = 102.8m/s		
Icing Condition	LWC (g/m ³)	MVD (μ)
Heavy, ○	0.77	20
Light, △	0.38	12

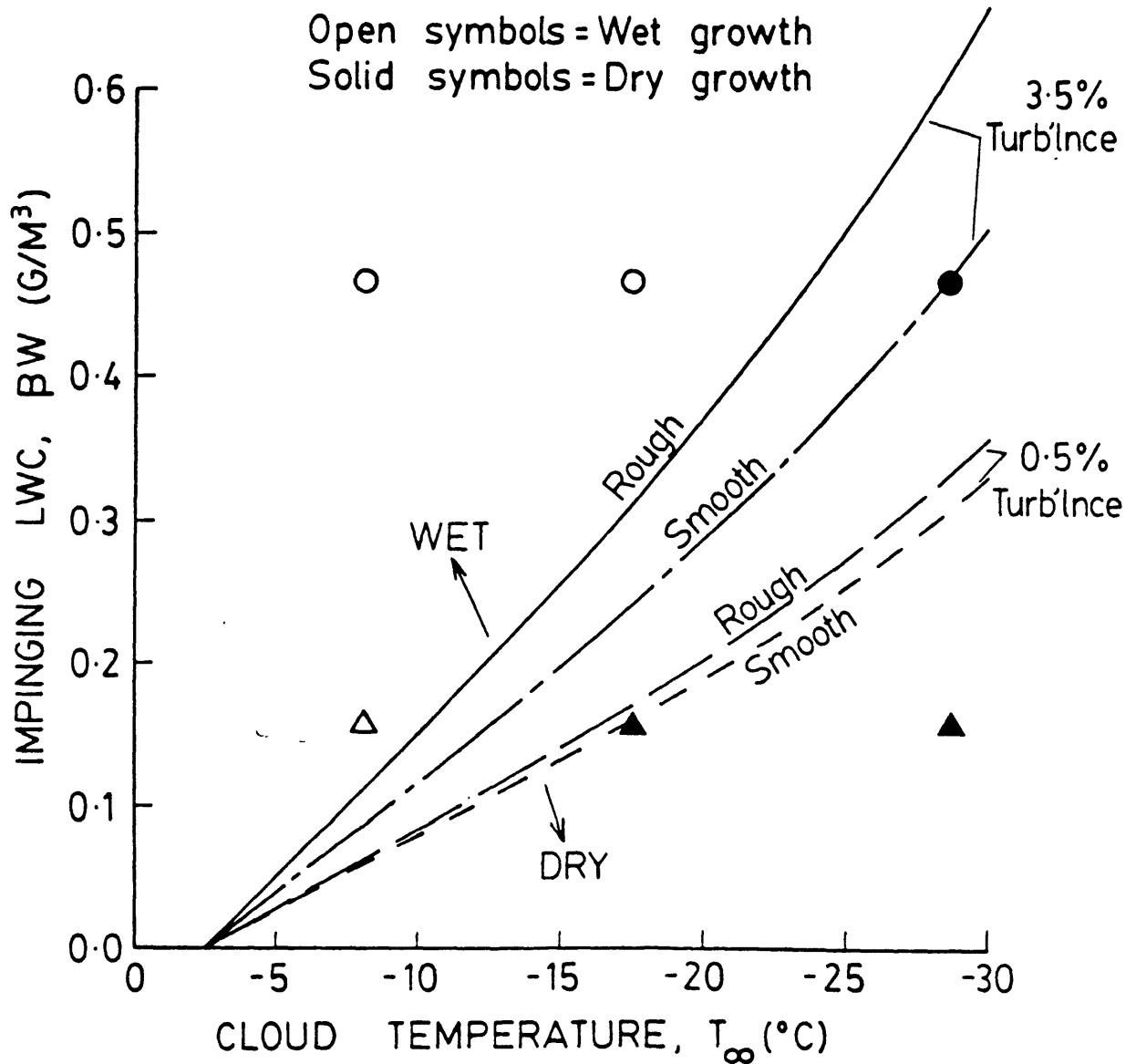


Fig. 4-7

Plot of impinging liquid water content versus cloud temperature, showing ultrasonically measured wet/dry ice growth and theoretical wet/dry threshold curves.

freestream velocity of 102.8 m/s and a cylinder diameter of 0.102 m.

Each of these threshold curves thus represents the impinging liquid water content calculated to produce transition from dry to wet ice growth, as a function of the icing cloud temperature. The "critical" impinging liquid water content, $(\beta W)_{crit}$, at which this transition occurs, depends on the convective heat transfer from the icing surface. Hence the four different heat transfer models predict different wet/dry thresholds. For each threshold curve, the ice growth is predicted to be dry if the impinging liquid water content is less than the critical value, $(\beta W)_{crit}$, calculated for that cloud temperature. If the impinging liquid water content exceeds this critical value then the ice growth is predicted to be wet.

Comparing the four threshold curves (figure 4-7), it can be seen that the heat transfer models that best predict the experimentally observed pattern of wet and dry ice growth are the 3.5% turbulence level models. Although all four models correctly predict the three experimentally observed wet growth cases, both of the 0.5% turbulence level models incorrectly predict wet growth for the heavy icing condition at -28.6°C , when dry growth was experimentally observed.

The wet/dry threshold curves for both of these 0.5% turbulence models imply transition from dry to wet ice growth at a significantly lower impinging liquid water content level than that for the heavy icing dry growth observed at -28.6°C . Since the wet/dry thresholds predicted by these heat transfer models are lower than that suggested by the observed wet/dry pattern, it appears that the 0.5% freestream turbulence level models underpredict the actual heat transfer magnitude from the icing surface.

The implied heat transfer coefficients are higher for the 3.5% turbulence level models, and hence the threshold curves for these models predict transition from dry to wet growth at higher impinging liquid water contents than the 0.5% turbulence level models. The rough surface, 3.5% turbulence model clearly predicts dry growth for the heavy icing case at -28.6°C . However this dry growth point lies on the wet/dry threshold predicted by the smooth surface model, and thus the heat transfer may again be slightly underpredicted by this model.

Based on this steady-state analysis, it appears that the heat transfer from the stagnation region is significantly higher than that predicted by the 0.5% freestream turbulence level heat transfer coefficients. The heat transfer model that best predicts the experimentally measured wet/dry ice

growth behaviour is the 3.5% turbulence level, rough surface model,

$$\text{Nu} = 0.2460 \text{ Re}^{0.6444} \quad (4.6)$$

This heat transfer model (eq. 4.6) was used to compare other wet/dry ice growth behaviour, measured for different tunnel icing conditions. Figure 4-8 is similar to figure 4-7, with impinging liquid water content, βW , plotted versus icing cloud temperature. Two separate plots are shown in the figure, corresponding to two different tunnel freestream velocities. The upper plot shows ultrasonic wet/dry ice growth measurements for a freestream velocity of 71.5 m/s (160 mph) and the lower plot for a velocity of 49.2 m/s (110 mph). The impinging liquid water contents for the experimental points shown were again inferred from the ultrasonically measured dry growth accretion rates. For those cases where no dry growth was observed, the impinging liquid water content was obtained by direct calculation of the local collection efficiency, β .

The wet/dry threshold curves calculated using the 3.5% turbulence, rough surface heat transfer model are also shown for the two different freestream velocities. For impinging liquid water contents less than the calculated transition value, $(\beta W)_{\text{crit}}$, dry growth is predicted, and this area is shaded in the figure for each plot.

Symbol	LWC (g/m ³)	MVD (μ)
○	1.06	20.5
△	0.52	14
□	1.50	18
▽	0.75	14

Open symbols = Wet growth
Solid symbols = Dry growth

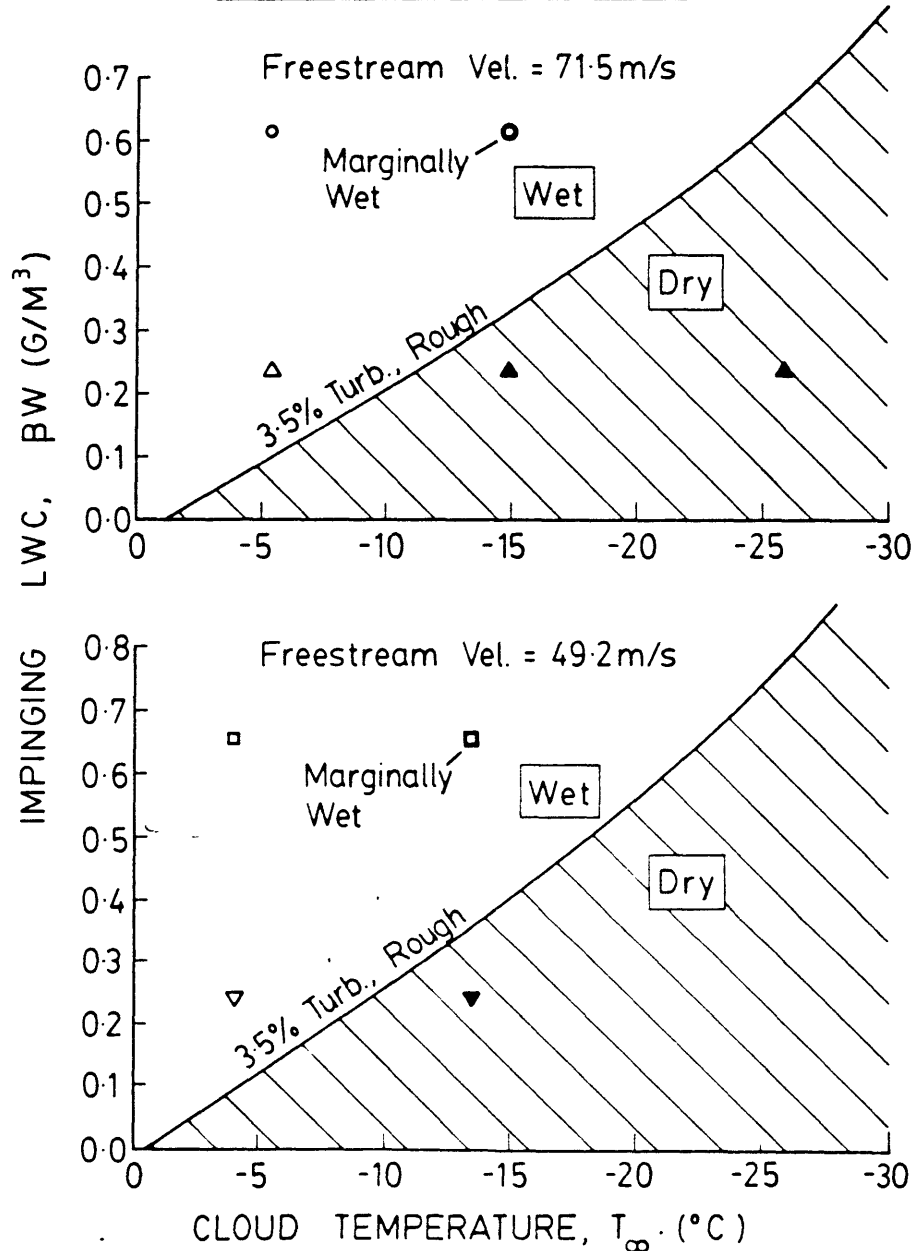


Fig. 4-8

Plot of impinging liquid water content versus cloud temperature, showing ultrasonically measured wet/dry ice growth and theoretical wet/dry threshold curves.

All three experimentally observed dry growth points fall within the dry growth regimes calculated using the 3.5% turbulence; rough surface model. In addition, the two points characterized as marginally wet (based on the ultrasonic echo signals received during the ice growth), suggest that the heat transfer over the ice surface may in fact be even greater than that implied by this heat transfer model.

4.6 SUMMARY OF ICE GROWTH BEHAVIOUR AND HEAT TRANSFER CHARACTERISTICS

Ultrasonic measurements of ice growth in the stagnation region of a cylinder exposed to different icing conditions in the IRT have provided the following information:

1. After any initial transient variations, the stagnation region ice growth exhibits a "steady-state" period, during which time the accretion rate is essentially constant.
2. For dry ice growth, the accretion rate is directly proportional to the impinging liquid water content, and is hence determined by the cloud liquid water content and the local collection efficiency.

3. As the cloud temperature increases, wet ice growth is observed in the stagnation region. The accretion rate for wet growth is lower than the dry growth rate at colder cloud temperatures.
4. By comparing the wet and dry growth accretion rates the local freezing fraction may be inferred. The low freezing fractions experimentally encountered at warm cloud temperatures, suggest liquid runback from the stagnation region during this initial growth period.
5. Ultrasonic measurements of wet and dry ice growth can be compared with wet and dry ice growth regimes theoretically predicted using the quasi steady-state energy balance.
6. Using the steady-state energy balance, heat transfer coefficients have been compared as models for the convective heat transfer in the cylinder stagnation region. Based on the predicted wet/dry thresholds, the heat transfer occurring during initial ice growth appears to be best modeled by Van Fossen's 3.5% freestream turbulence, rough surface heat transfer measurements for a bare cylinder. There are, however, some experimental indications that the actual heat transfer magnitude may be slightly in excess of that predicted by this model.

Chapter 5

ICING OF A CYLINDER IN NATURAL ICING CONDITIONS

5.1 OVERVIEW

This chapter presents experimental measurements of ice growth on a cylinder exposed to natural icing conditions in flight. Ultrasonic measurements of ice thickness and ice surface condition (wet or dry) are analyzed and compared to similar measurements obtained for the icing wind tunnel tests (Chapter 4).

Sections 5.2 and 5.3 outline the experimental apparatus used and the cylinder installation on the flight test aircraft. The test procedure for each in-flight exposure of the cylinder is also described in Section 5.3. Typical natural icing cloud conditions and experimentally observed ice growth behaviour are discussed in Section 5.4. Ultrasonic measurements are presented showing both wet and dry ice growth occurring as a result of in-flight variations in the cloud liquid water content.

Section 5.5 compares the ultrasonically measured wet and dry ice growth behaviour for each flight with that predicted

using the steady-state energy balance and the four heat transfer models described in Chapter 4. The heat transfer magnitude in the cylinder stagnation region is generally inferred to be lower for the natural icing conditions encountered in flight than for the icing conditions produced in the Icing Research Tunnel. However, variations in the implied heat transfer magnitude are observed, and may be due to different turbulence levels associated with natural icing clouds.

5.2 EXPERIMENTAL APPARATUS

The experimental apparatus employed to measure ice growth in natural icing conditions was similar to that described in Chapter 4 for the icing wind tunnel tests (see figure 4-1). The test cylinder for the flight tests had a diameter of 11.4 cm (4.5 in.), and was instrumented with two 5 MHz ultrasonic transducers. The transducers were mounted on the stagnation line, flush with the cylinder surface. Both transducers had diameters of 0.6 cm, and were located near the midsection of the 38.1 cm long cylinder.

A pulser/receiver unit was used to drive the ultrasonic transducers, and the resulting pulse-echo signals were displayed on an oscilloscope. The oscilloscope screen was again videotaped with a camera to provide a permanent record

of these time dependent signals. A digital clock mounted to the oscilloscope screen was used to record the cylinder exposure time. Figure 5-1 shows the video camera and oscilloscope installed in the icing research aircraft.

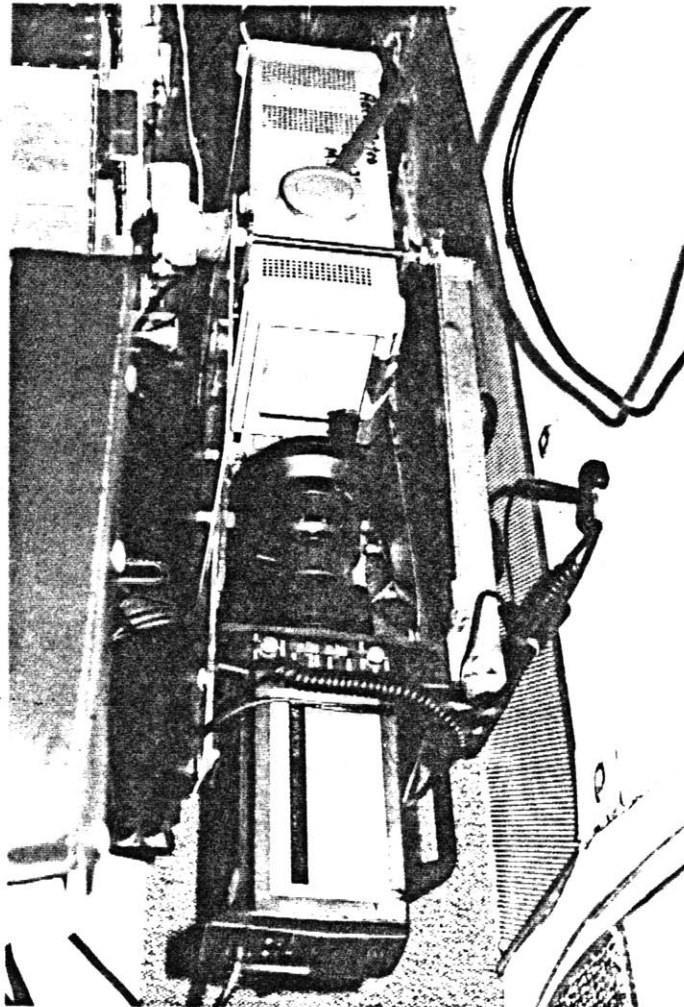


Fig. 5-1 Photograph of the video camera and oscilloscope installation on the floor of the NASA Lewis Icing Research Aircraft.

5.3 NATURAL ICING FLIGHT TESTS

5.3.1 CYLINDER INSTALLATION ON THE ICING RESEARCH AIRCRAFT

The natural icing flight tests were conducted from the NASA Lewis Icing Research Aircraft, a De Havilland DHC-6 Twin Otter. The test cylinder was mounted vertically on an experiment carrier platform that could be raised through the roof of the aircraft, thus exposing the cylinder to the natural icing cloud. Figure 5-2 illustrates this configuration, with the cylinder extended into the freestream above the aircraft. The cylinder was mounted on an extension post, enabling the instrumented cylinder midsection to be located 53.3 cm into the freestream when deployed. The freestream disturbance, due to the aircraft flowfield, was thus small at the cylinder midsection. Figure 5-3 is a photograph (looking aft along the roof of the aircraft), showing the cylinder in its fully extended position.

5.3.2 ICING RESEARCH AIRCRAFT INSTRUMENTATION

The icing research aircraft (figure 5-2) was equipped with several icing cloud instruments, used to measure the ambient natural icing conditions encountered in flight.

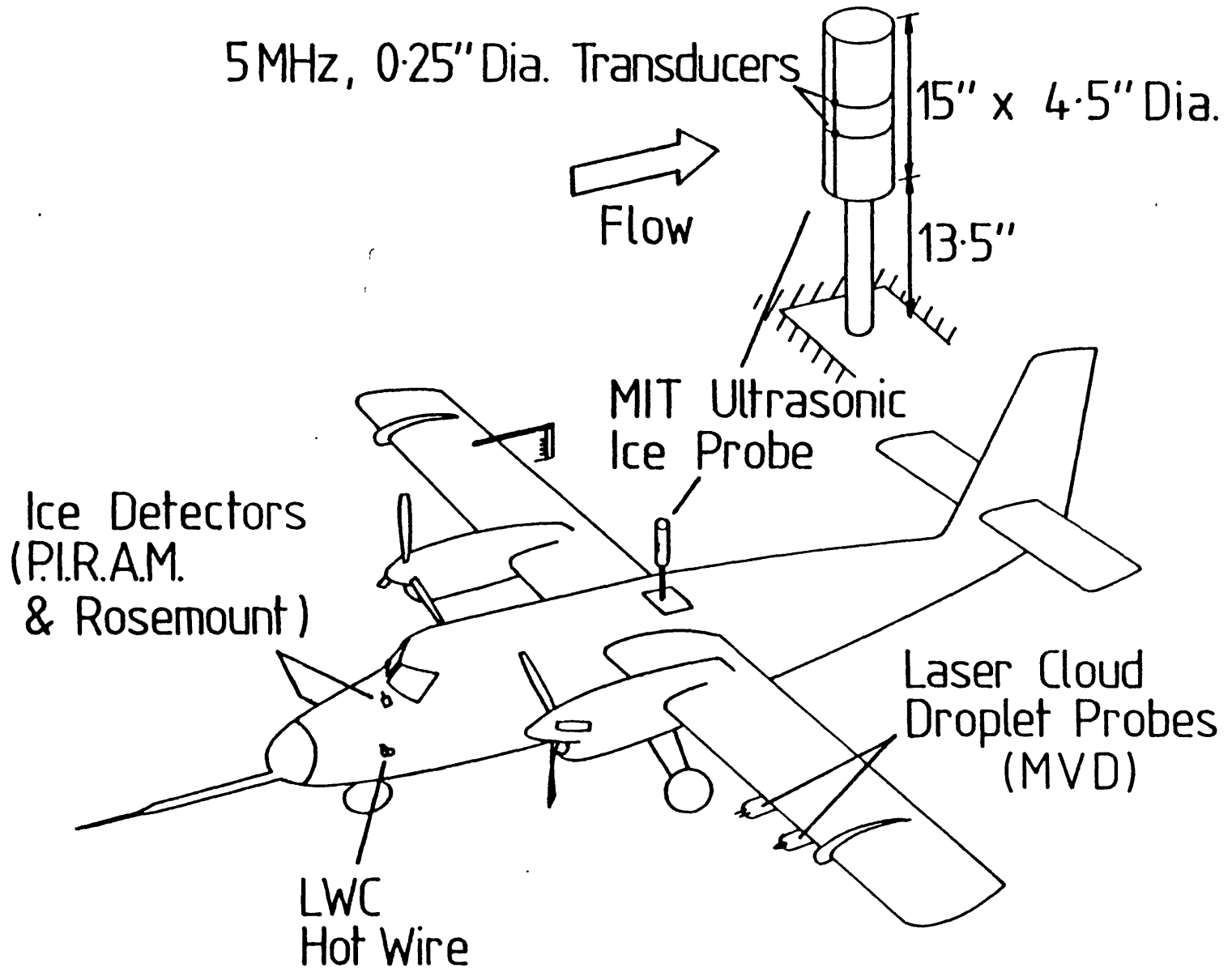


Fig. 5-2 Cylinder installation on the NASA Lewis Icing Research Aircraft.

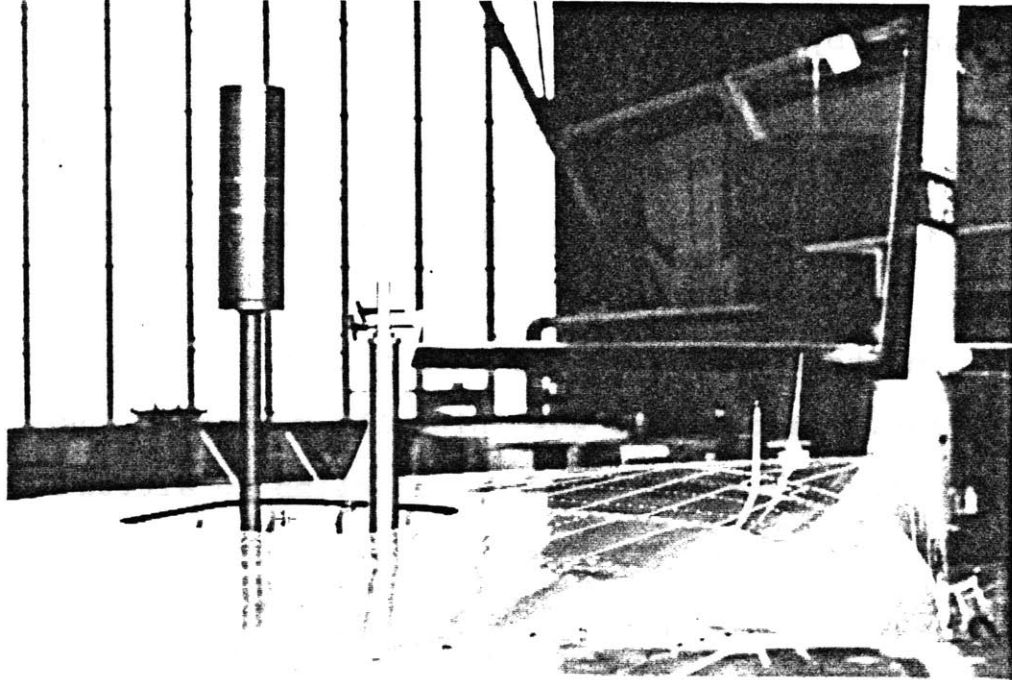


Fig. 5-3 Photograph showing the test cylinder extended above the roof of the icing research aircraft.

In particular, the cloud liquid water content measurements presented for each flight were obtained from a Johnson-Williams hot-wire probe mounted near the nose of the aircraft. A Particle Measuring Systems forward scattering spectrometer probe (FSSP) was used to measure the cloud droplet size distribution, from which the droplet median volume diameter was later calculated. This probe (FSSP) was mounted under the port wing of the aircraft. An onboard data acquisition system sampled and recorded measurements from these icing cloud instruments throughout each flight. Other

aircraft and flight data (airspeed, altitude etc.) were also recorded by this system.

5.3.3 FLIGHT TEST PROCEDURE IN NATURAL ICING CONDITIONS

The test procedure for each flight conducted was as follows. The cylinder was initially retracted inside the aircraft during the take-off and climb to altitude. Once icing conditions were encountered, a "holding" pattern was established at that altitude, if possible. Typically, this altitude was between 3000 and 8000 feet.

With the aircraft within the icing cloud layer, the experiment carrier was raised, thus exposing the cylinder to the icing cloud. A limit switch on the experiment carrier allowed icing cloud data recorded during the flight to be synchronized with the cylinder exposure time. The cylinder was exposed throughout the entire icing encounter, which typically lasted from 10 to 50 minutes. The pulse-echo signals received from the ultrasonic transducers on the cylinder stagnation line were continuously displayed and recorded by the oscilloscope/camera system during the exposure.

At the completion of the icing encounter the cylinder was retracted into the aircraft. The iced diameter of the

cylinder was then measured at each transducer location, using outside calipers; the total ice thickness accreted during the exposure was inferred from this measurement.

Four research flights (85-22 to 85-25) were conducted with the cylinder and ultrasonic system during the period March 30-April 2, 1985.

5.3.4 SUMMARY OF TIME-AVERAGED NATURAL ICING CONDITIONS AND CYLINDER ICE ACCRETIONS

Figure 5-4 contains a summary of the time-averaged icing conditions during each of the four in-flight exposures of the test cylinder. The shape of the accreted ice at the completion of the exposure (from photographs of the iced cylinder), is also sketched for each flight.

The ice thicknesses measured on the cylinder stagnation line at the end of the exposure are indicated for the both the ultrasonic system and the outside caliper measurement. As in the icing wind tunnel tests, the ultrasonic pulse-echo thickness measurements are within ± 0.5 mm of the caliper readings, confirming the speed of sound is relatively constant for ice formed under typical flight icing conditions.

TIME - AVERAGED ICING CONDITIONS						
FLIGHT NUMBER	EXPOSURE TIME (MIN:SEC)	TEMP (°C)	LWC (GM/M3)	MVD (μ)	VEL (MPH)	ALTITUDE (FEET)
85-22	20:41	-5.4	0.36	11.9	157	2728
85-23	47:08	-3.3	0.18	11.4	147	3404
85-24	10:07	-14.6	0.46	14 est.	161	6480
85-25	36:40	-15.1	0.19	14.1	167	7019

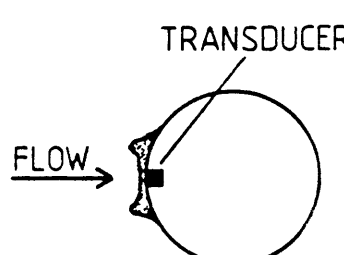
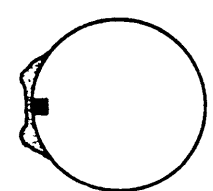
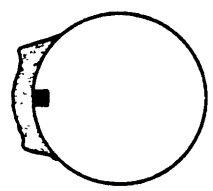
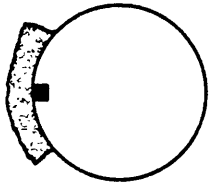
FLIGHT NUMBER	ULTRASONICALLY MEASURED ICE THICKNESS (MM)	MECHANICALLY MEASURED ICE THICKNESS (MM)	ICE SHAPE
85-22	3.1	2.7	
85-23	3.3	ICE SLID OFF	
85-24	8.9	8.7	
85-25	VIDEO TAPE DAMAGED	9.6	

Fig. 5-4 Summary of time-averaged icing conditions and cylinder ice accretions for flight tests.

However, while constant icing conditions were maintained for each exposure in the Icing Research Tunnel, the natural icing conditions encountered in flight varied throughout each exposure. These unsteady icing conditions, and the different ice growth behaviour observed as the ambient conditions changed, are discussed in the next section.

5.4 ICE GROWTH BEHAVIOUR OBSERVED DURING NATURAL ICING CONDITIONS

From the ice thicknesses indicated in figure 5-4 and the corresponding exposure times, it can be seen that the average ice accretion rates observed during the natural icing flight tests were much lower than those obtained in the Icing Research Tunnel tests. For example, only during the exposure on flight 85-24 did the average accretion rate on the cylinder stagnation line exceed 0.3 mm/min. These lower overall accretion rates (ice thickness/exposure time) are primarily due to the lower average liquid water contents encountered in these flight tests.

Figure 5-5 shows the ice thickness measured with the ultrasonic system plotted against exposure time for flight 85-24. Also shown are the time-averaged icing conditions during the 10 minute exposure. The cloud temperature for this exposure was relatively cold (-14.6°C), and rime

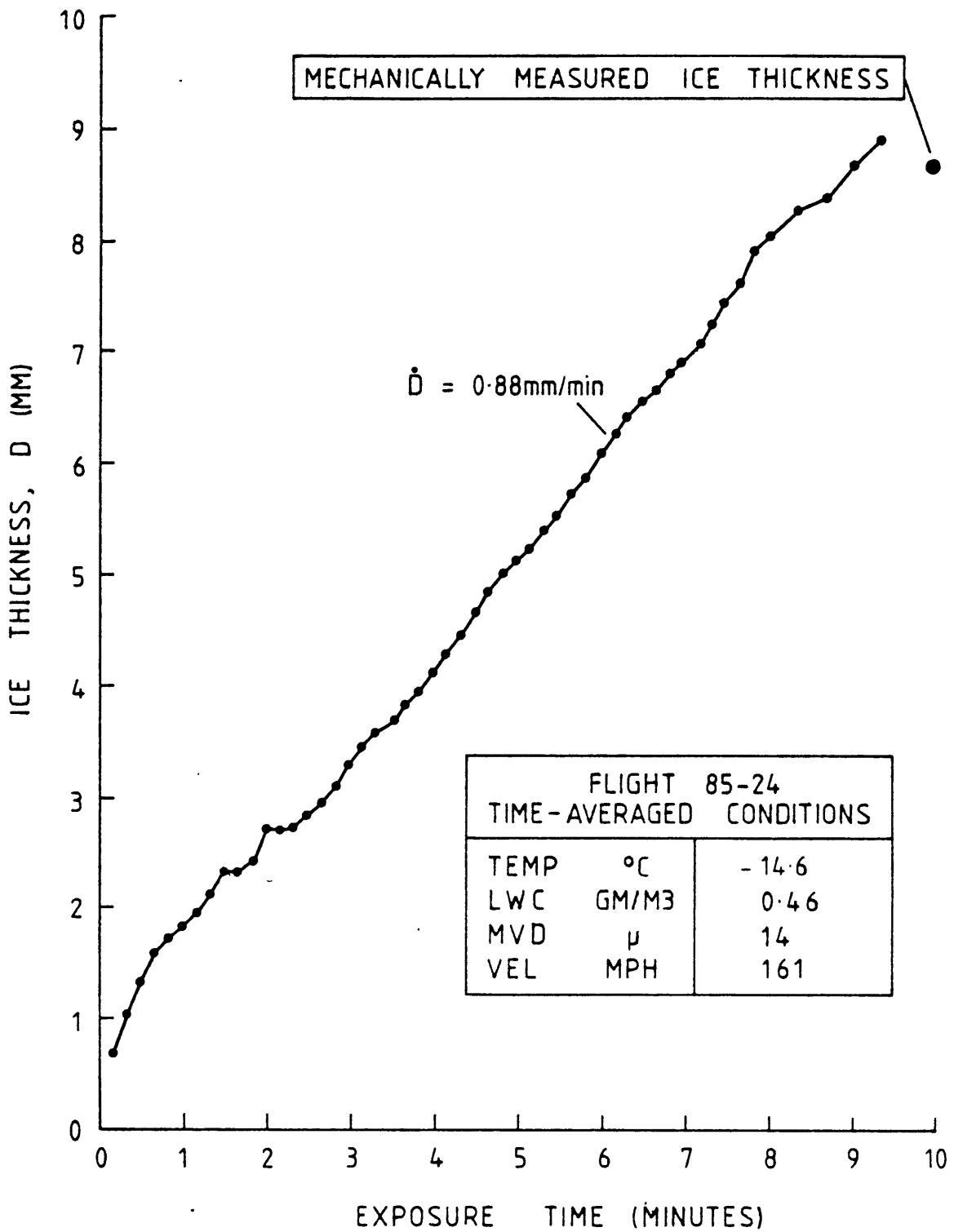


Fig. 5-5 Ice thickness vs. exposure time for flight 85-24.

ice formation was observed for most of the exposure. The average accretion rate was determined to be 0.88 mm/min, from the slope of the ice thickness curve.

The ice thickness measured during flight 85-24 (figure 5-5) increases fairly linearly with exposure time. This linear or "steady-state" ice growth behaviour was also observed during the tests conducted in the Icing Research Tunnel. However while the ambient icing conditions were constant for the icing wind tunnel tests, the icing conditions varied throughout each in-flight exposure. The linear increase in ice thickness with exposure time observed for the in-flight exposure is therefore of particular interest, and suggests that, under certain icing conditions the time fluctuations in cloud properties may not significantly influence the accretion behaviour. The variations in icing cloud properties, observed in flight, are discussed below.

Figure 5-6 is a plot of the flight data recorded during the cylinder exposure on flight 85-22. The ambient icing conditions (cloud temperature, liquid water content and median volume diameter), measured by the aircraft's icing cloud instrumentation, are plotted versus the cylinder exposure time. Also shown are the aircraft airspeed and altitude for the exposure period.

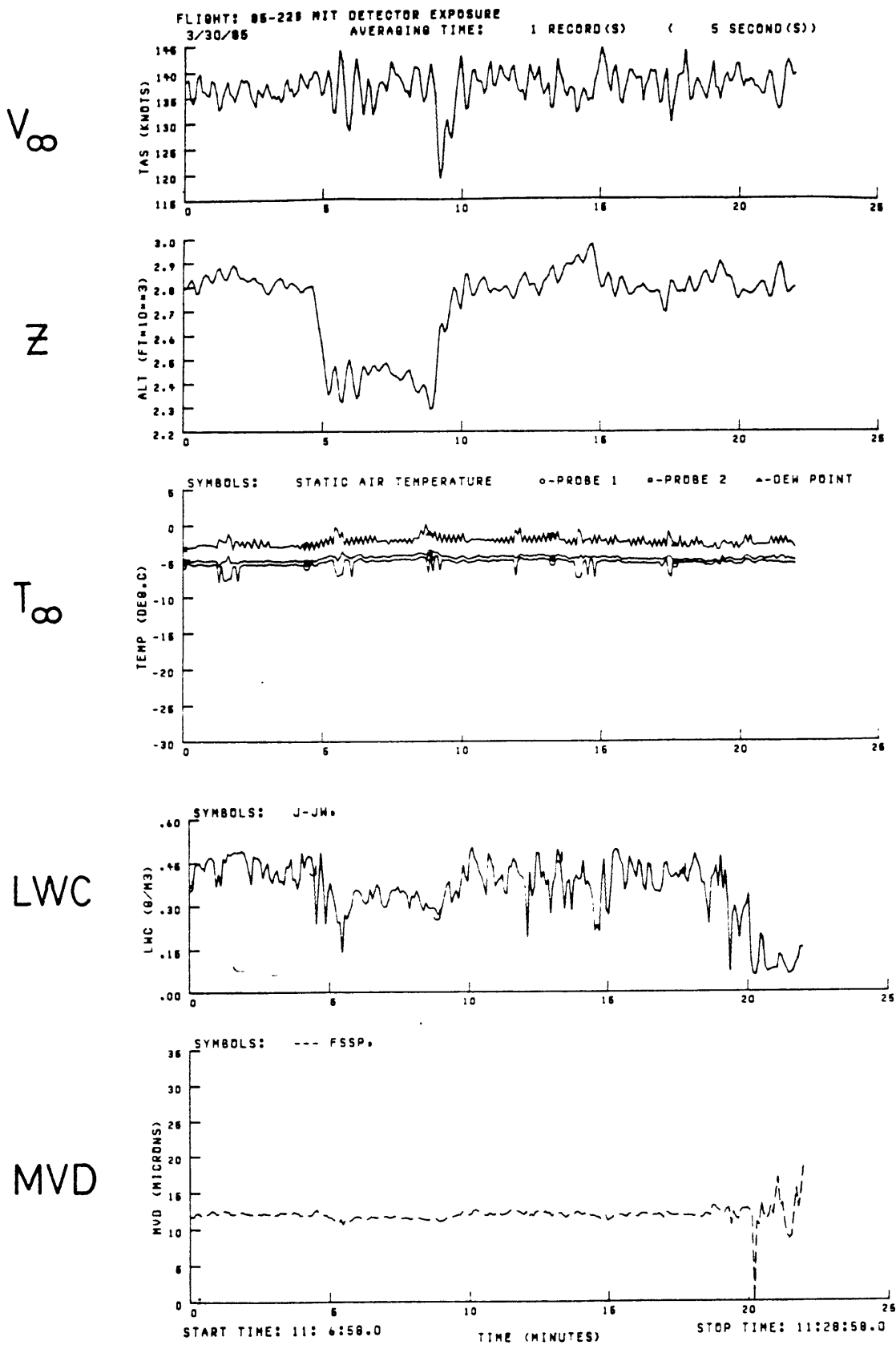


Fig. 5-6 Typical icing cloud and flight data for cylinder exposure period (flight 85-22).

From the figure, it can be seen that the airspeed and altitude were held fairly constant during the exposure, as desired. The static air temperature is also seen to be relatively constant throughout the exposure. Typically, these three parameters - airspeed, altitude and cloud temperature - were not observed to vary significantly during the four cylinder exposures conducted.

However, the cloud liquid water content did vary considerably throughout each exposure. For example, the liquid water content (measured by the Johnson-Williams hot-wire probe), varied from less than 0.15 g/m^3 to over 0.5 g/m^3 during the cylinder exposure on flight 85-22 (see figure 5-6). The fluctuations in cloud liquid water content shown in figure 5-6, are characteristic of all the exposures conducted in natural icing conditions.

Although the cloud droplet median volume diameter measured (FSSP) during the cylinder exposure for flight 85-22 was relatively constant (MVD = 12 microns), this was not the case for all the exposures. For example, the droplet median volume diameter measured for flight 85-25 varied from 11 to 21 microns during the course of the 37 minute cylinder exposure.

These variations in both the cloud liquid water content, and the droplet size distribution, produce corresponding

fluctuations in the liquid water content impinging on a body in natural icing conditions. As a result, periods of wet and dry ice growth may occur as the impinging liquid water content, BW , varies.

Figure 5-7 is a plot of the measured cloud liquid water content versus cylinder exposure time, for flight 85-24. Also shown are experimentally observed periods of wet, dry and transitional ice growth on the cylinder stagnation line. The ultrasonic echo signals during natural icing conditions displayed the same characteristics as those observed in the icing wind tunnel tests, and were again used to determine the type of ice growth. The ice growth was categorized as transitional when the time variation in the detailed shape of the ultrasonic echo signal was between that characteristically observed for wet or completely dry ice growth.

From the figure, it can be seen that dry ice growth was observed for cloud liquid water contents below 0.4 g/m^3 , while wet growth occurred for sustained liquid water contents above approximately 0.55 g/m^3 . At the lower liquid water content levels ($<0.4 \text{ g/m}^3$), the heat transfer from the stagnation region is sufficient to freeze all the locally impinging mass flux due to the cloud droplets.

Dry = Dry ice growth Wet = Wet ice growth Tr. = Transitional ice growth

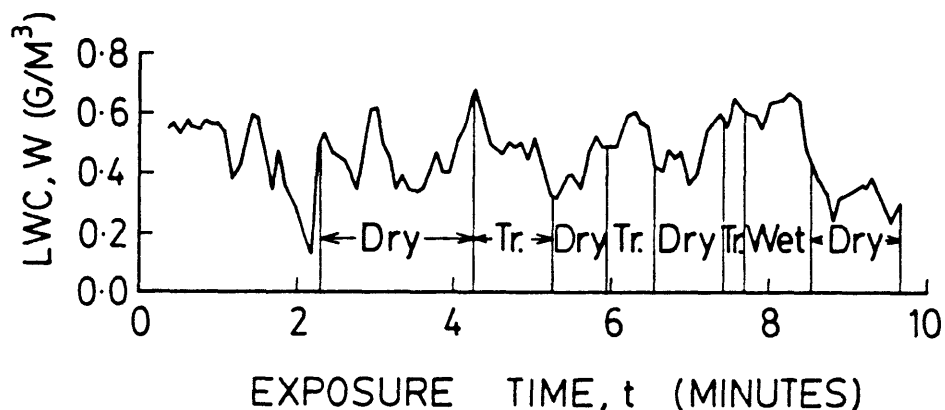


Fig. 5-7 Plot of liquid water content versus exposure time for flight 85-24 showing fluctuations in natural icing cloud liquid water content and wet, dry and transitional ice growth periods measured using ultrasonic system.

However when the liquid water content exceeds a critical value, the rate of heat removal from the ice surface is insufficient to freeze all the impinging mass flux, and liquid forms on the ice surface. The "critical" impinging liquid water content at which this wet growth begins depends on the local heat transfer coefficient for the icing

surface, as discussed in Chapters 2 & 4. The ultrasonically measured wet and dry ice growth periods may thus be used in conjunction with the icing cloud data to compare different heat transfer coefficient models applicable to natural icing conditions. This comparison of heat transfer models for the cylinder stagnation region is discussed in the next section.

5.5 COMPARISON OF HEAT TRANSFER COEFFICIENT MODELS FOR THE STAGNATION REGION OF A CYLINDER IN NATURAL ICING CONDITIONS

The analysis presented in this section follows closely that outlined in Chapter 4 for the icing wind tunnel tests. The four heat transfer models compared are again the high and low (3.5% & 0.5%) freestream turbulence, rough or smooth surface, cylinder stagnation region heat transfer coefficients measured by Van Fossen et al¹².

However, while constant ambient icing conditions were maintained during each exposure in the icing wind tunnel tests, the natural icing cloud conditions in the flight tests varied throughout each exposure. Therefore, in order to use the quasi steady-state energy balance to compare predicted wet/dry thresholds with the experimentally observed wet and dry ice growth, a simple steady-state "time constant" was estimated. This time constant approach was

taken to minimize the effects of transient thermal behaviour not accounted for in the steady-state energy balance.

A time constant of 10 seconds was selected, based on both the transient thermal response of a thin ice layer, and the frequency response of the Johnson-Williams hot-wire probe (~5 seconds¹⁷). Thus only cloud liquid water contents sustained for more than 10 seconds were used in the comparison with the wet/dry threshold curves calculated using the steady-state energy balance.

Figure 5-8 is a plot of impinging liquid water content versus cloud temperature. The experimentally observed, "steady-state" wet, dry and transitional ice growth regimes for the four cylinder exposures on flights 85-22 to 85-25, are plotted. The impinging liquid water content, βW , was determined from the cloud liquid water content measured by the Johnson-Williams hot-wire probe, and by direct calculation of the local collection efficiency. The local collection efficiency on the cylinder stagnation line was calculated¹⁵ for a monodisperse droplet distribution with a droplet diameter equal to the median volume diameter measured by the FSSP laser probe. The error in the collection efficiency calculated with this single droplet size assumption is considered small relative to the uncertainties present in the measurements of cloud liquid water content and droplet size distribution^{6,18}.

Cylinder Dia. = 0.114m	
Av. Freestream Vel. = 71.4 m/s	
Av. Altitude = 1613m	
Symbol	Flight No.
△	85-22
▽	85-23
○	85-24
□	85-25

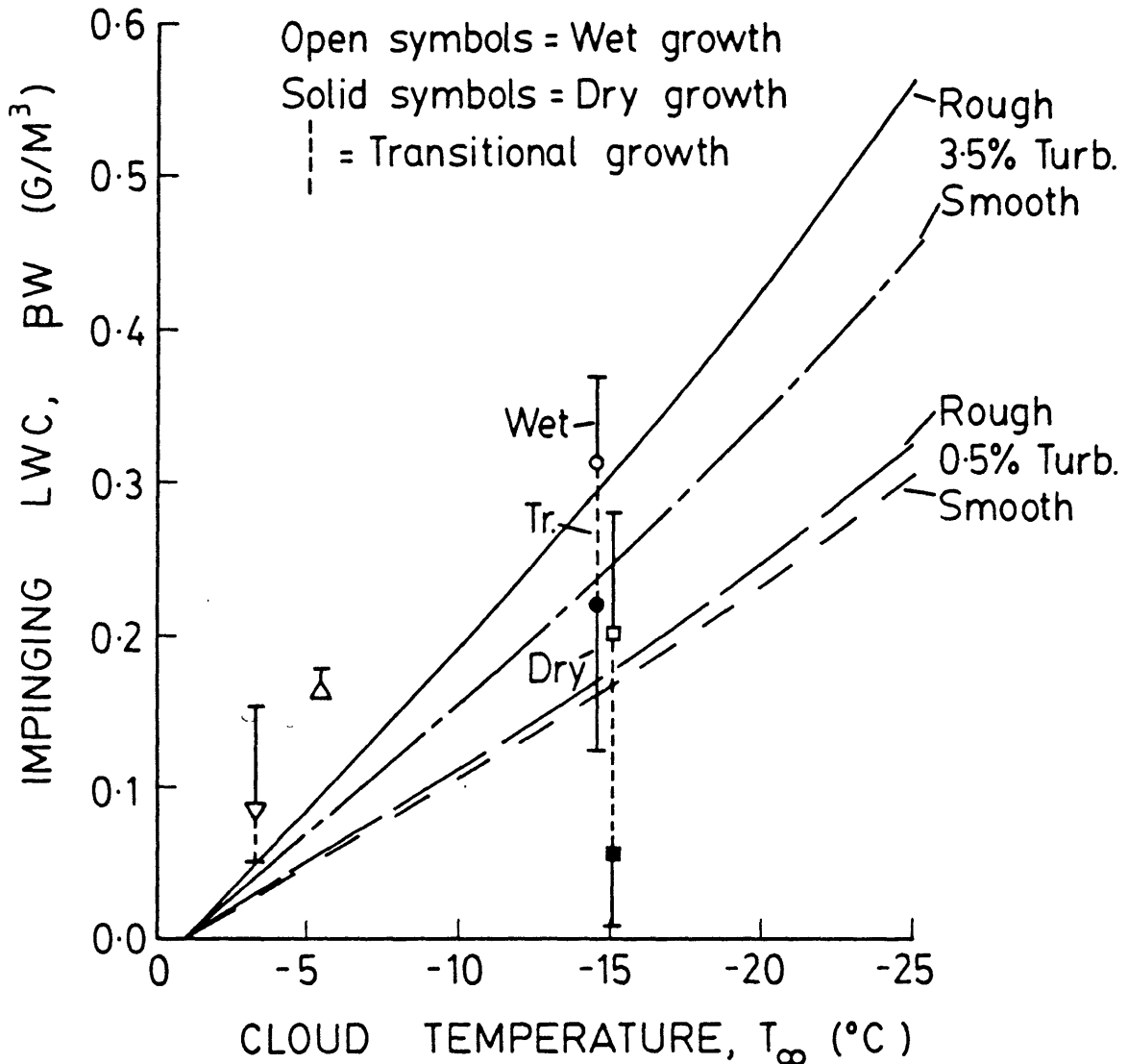


Fig. 5-8

Plot of impinging liquid water content versus cloud temperature showing wet, dry and transitional ice growth observed during flight tests, and theoretical wet/dry threshold curves

Also shown in figure 5-8 are the four wet/dry threshold curves calculated for the different heat transfer coefficient models described earlier. These curves were calculated for the test cylinder diameter, 11.4 cm, and for the average airspeed and altitude for the four exposures, 71.4 m/s and 1613 m, respectively (160 mph and 5290 ft).

The wet ice growth observed during flights 85-22 and 85-23 occurred at relatively warm cloud temperatures, and all four heat transfer models predict wet growth for these conditions.

On flight 85-24, the experimentally observed range of wet and dry ice growth is correctly predicted by the 3.5% turbulence level heat transfer coefficients. The wet/dry thresholds calculated for both the rough and smooth surface, 3.5% models, lie within the experimentally determined "transitional" ice growth band between dry and wet growth. The low (0.5%) turbulence heat transfer coefficient models appear to underestimate the heat transfer magnitude for this flight, since dry growth was experimentally observed at impinging liquid water contents above the wet/dry threshold predicted by these heat transfer models.

In contrast to flight 85-24, the high freestream turbulence (3.5%) models appear to overpredict the heat transfer magnitude for flight 85-25, and the low (0.5%)

turbulence models correctly predict the observed wet and dry ice growth ranges. From figure 5-8 it can be seen that both the rough and smooth surface heat transfer coefficients at the 3.5% turbulence level imply dry growth (based on the steady-state energy balance analysis), when wet growth was experimentally observed.

For this exposure (85-25), the low turbulence heat transfer coefficient models appear appropriate, since the wet/dry thresholds calculated for both of these coefficients correctly predict the observed wet growth regime. In fact, since dry growth was only observed at very low impinging liquid water contents ($<0.05 \text{ g/m}^3$), the actual heat transfer from the icing surface may have been even lower than that suggested by the 0.5% turbulence level models.

This result is significant, since it implies the heat transfer magnitude in flight may, in some cases, be lower than that for an equivalent icing surface in the Icing Research Tunnel. As discussed earlier, the magnitude of the heat transfer coefficient in the stagnation region is of critical importance, since it determines the threshold between dry and wet ice growth. Any difference therefore, between the heat transfer magnitude in the Icing Research Tunnel and in flight, could result in different ice growth behaviour for seemingly identical "ambient" icing conditions. These differences in ice growth behaviour would

be most pronounced during wet growth, with different local freezing fractions and possibly different degrees of liquid runback. The implication is that, under certain icing conditions, the ice accretions formed in flight and in the Icing Research Tunnel would be different. Since the purpose of the icing wind tunnel is to provide a natural icing simulation capability, this situation would clearly be undesirable, unless a correction can be applied to allow for different heat transfer magnitudes.

The experimental results shown in figure 5-8 also indicate that there may be some variation in the convective heat transfer magnitude encountered during flight through different icing clouds. For example, during flights 85-24 and 85-25, the cloud temperatures, liquid water contents and droplet sizes encountered were roughly comparable, and yet different ranges of wet and dry ice growth were experimentally observed. This can be seen in figure 5-8 as the observed wet and dry growth ranges for these two flights overlap at the same impinging liquid water content level (0.2 g/m^3). The implication is that the heat transfer from the icing surface differed between these two flights, both at nominally similar icing conditions, but conducted on different days, through different natural icing clouds. One plausible explanation for this apparent variation in the convective heat transfer are differences in the turbulence levels associated with different cloud formations, e.g.

convective versus stratiform clouds.

5.6 SUMMARY OF ICE GROWTH BEHAVIOUR AND HEAT TRANSFER
ANALYSIS FOR NATURAL ICING CONDITIONS

During flight through natural icing clouds the icing conditions are not constant. The most significant variation is seen in the cloud liquid water content, although the cloud temperature and droplet size distribution may also vary. Fluctuations in the cloud liquid water content can result in periods of both wet and dry ice growth occurring during a single icing cloud encounter.

Although ice growth was only measured for four exposures in natural icing conditions, on at least one of these exposures (85-24) the ice thickness was observed to increase approximately linearly with exposure time. This constant accretion rate behaviour, despite fluctuations in the cloud liquid water content, suggests that for relatively cold cloud temperatures the time-averaged value of the cloud liquid water content may be appropriate to characterize the natural icing encounter. However at warmer cloud temperatures, fluctuations in the cloud liquid water content may be important in determining periods of wet ice growth.

Based on the wet/dry ice growth behaviour observed during the four flight tests conducted, it appears that the heat transfer magnitude appropriate for an icing surface in flight may be lower than that inferred for the Icing Research Tunnel.

The heat transfer during the initial icing period has been found to vary between that suggested by the 3.5% freestream turbulence level and 0.5% turbulence level heat transfer coefficients of Van Fossen et al.. A similar analysis showed the heat transfer for the Icing Research Tunnel tests was best modeled by the 3.5% turbulence level coefficients. The difference in heat transfer magnitude may thus be due to a higher freestream turbulence level in the Icing Research Tunnel. Considering the upstream spray bar system used in the Icing Research Tunnel, a higher freestream turbulence level in the tunnel test section than at the cylinder location above the aircraft, might be expected.

In addition to the generally lower heat transfer magnitude inferred from the flight test results, variations in the heat transfer magnitude were also observed for flights conducted on different days. These variations may again be associated with the freestream turbulence level, since different cloud formations have characteristically different turbulence levels associated with them.

All of these results highlight the variability of natural icing cloud conditions and the inherent difficulty in accurately simulating these conditions in an icing wind tunnel. However, the differences observed in the implied heat transfer magnitude for the Icing Research Tunnel and natural icing conditions dictate that care should be taken in extrapolating results from icing wind tunnel tests to "similar" natural icing conditions.

Chapter 6

SUMMARY AND CONCLUSIONS

Chapter 1 provided background information on aircraft icing. Icing conditions were defined and typical icing cloud parameters given. The effects of ice accretion on aircraft performance were briefly outlined and illustrated. The rationale for developing analytic models to predict ice accretion was explained, and the steps involved in the modeling procedure described. It was shown that the ice shapes predicted by these analytic models can be extremely sensitive to the assumed heat transfer distribution over the body under certain ambient icing conditions. The lack of experimental heat transfer data for real ice surfaces has hindered the successful development of these models, as have fundamental questions about the behaviour of liquid water on the ice surface.

In Chapter 2 a quasi steady-state energy balance for the accreting surface was described. The energy balance considers six modes of energy transport to and from the icing surface, and is largely based on the earlier work of Messinger¹¹. The assumptions implicit in both the quasi steady-state approach and the energy balance itself were

discussed. The mass and energy balance equations were derived for both dry and wet ice growth conditions, the latter for the stagnation region only. An expression defining the threshold between wet and dry ice growth was obtained in terms of a critical impinging liquid water content and the local heat transfer coefficient for the ice surface.

The ultrasonic pulse-echo techniques employed to measure ice growth in artificial and natural icing conditions were described in Chapter 3. The time of flight principle used in ultrasonic pulse-echo thickness measurement was explained, and it was shown that a continuous thickness measurement can be achieved by repeatedly emitting pulses at a high pulse repetition rate. The ultrasonic echo signals received from accreting ice surfaces were then described. The presence of liquid water on the ice surface during wet ice growth was shown to produce a unique time variation in the received echo signal, thus allowing the ultrasonic echo characteristics to be used to distinguish between wet and dry ice growth.

Chapter 4 described experimental measurements of ice growth in the stagnation region of a 10.2 cm diameter cylinder exposed to icing conditions produced in an icing wind tunnel. The ambient icing conditions for these tests in the Icing Research Tunnel were constant for each test run

conducted. Plots of ice thickness versus exposure time were presented for two different icing cloud sets, characterized as "heavy" and "light" icing conditions. In all cases these plots showed a "steady-state" period in which the ice thickness increased relatively linearly with exposure time.

For the exposures during which the ice growth was observed to be dry, this constant accretion rate behaviour was inferred to indicate that the local collection efficiency, and hence the flowfield, were unchanged by the ice accretion during this initial icing period. The exposures for which the ice surface was determined to be wet also exhibited a similar period of constant growth rate. In these cases (wet growth), the constant accretion rate was most likely an indication that both the local collection efficiency and the local heat transfer from the icing surface were essentially unchanged as the ice accreted during this initial icing period.

The effect of cloud temperature on the ice growth behaviour was also investigated. At warm cloud temperatures the ice surface was observed to be wet and the measured accretion rates were low. However, as the cloud temperature was progressively reduced, the accretion rate increased to a maximum value and then remained constant despite further decreases in the cloud temperature. At the "warm" cloud temperatures, the heat transfer from the ice surface was

insufficient to freeze all the impinging droplet mass flux, and hence the freezing fraction was less than unity, and the accretion rate low. As the temperature "potential" is increased between the wet ice surface at 0°C and the icing cloud, the heat transfer from the surface increases, thus increasing the accretion rate. Finally, when the heat transfer is sufficient to freeze all the impinging droplets on impact, the ice growth is dry and the accretion rate a maximum.

By comparing the low accretion rates, measured at the warm cloud temperatures, with the higher dry growth accretion rates, the freezing fractions for the wet growth cases were inferred. These implied freezing fractions, and the ultrasonic echo characteristics observed for these wet growth cases, indicated that liquid runback from the stagnation region did occur during the initial icing period for these wet growth cases.

Also contained in Chapter 4 was a comparison of the experimentally measured wet and dry ice growth conditions with the regimes of wet and dry ice growth predicted by the steady-state energy balance presented in Chapter 2. Specifically, four different heat transfer coefficient models were compared in the energy balance equation. The four models used were from experimental heat transfer measurements by Van Fossen et al. for the stagnation region

of a cylinder.

The results of this comparison showed that the heat transfer in the stagnation region of the test cylinder during icing conditions in the Icing Research Tunnel was best modeled by a heat transfer coefficient measured with a high (3.5%) freestream turbulence level. Heat transfer coefficients with a lower associated freestream turbulence level (0.5%) incorrectly predicted wet growth and therefore underestimated the actual heat transfer from the icing surface.

Chapter 5 presented measurements of ice growth in the stagnation region of an 11.4 cm diameter cylinder exposed in flight to natural icing conditions. Unlike the constant icing conditions maintained during each exposure in the icing wind tunnel tests, the icing conditions in flight were observed to vary throughout each exposure. The cloud liquid water content in particular characteristically fluctuated significantly. These fluctuations in liquid water content resulted in periods of dry, wet and transitional ice growth within the same exposure.

Despite these fluctuations in cloud liquid water content, a roughly linear increase in ice thickness with exposure time was observed for one exposure at a relatively cold cloud temperature. Although more experimental data is

needed, this result seems to indicate that, in some cases, the time-averaged liquid water content may adequately represent a natural icing encounter. However at warmer cloud temperatures, fluctuations in the liquid water content may be of greater importance.

A similar heat transfer analysis was conducted on the experimentally measured wet and dry ice growth data obtained in the flight tests as was performed for the Icing Research Tunnel data. The same (Van Fossen et al.) heat transfer coefficients were used in the steady-state energy balance equation to predict wet and dry ice growth regimes. The results of this comparison showed that the heat transfer magnitude for the icing surface in flight may be lower than that inferred for the Icing Research Tunnel. The heat transfer coefficient that best modeled the flight data appeared to lie between that associated with a high (3.5%) freestream turbulence and that for the lower, 0.5%, turbulence level investigated.

In addition, the results of the heat transfer analysis indicated that the magnitude of the heat transfer occurring in natural icing conditions may vary from day to day, despite similar icing conditions. This variation may be due to different turbulence levels associated with different icing cloud formations.

The results of the natural icing tests highlight the variations inherent in all natural icing encounters. Ice growth may vary from wet to dry within a single natural icing cloud as the impinging liquid water content fluctuates. The use of an average liquid water content to represent a particular natural icing condition may thus be inaccurate for some icing conditions, particularly for warm cloud temperatures. In addition, the potentially different heat transfer characteristics for icing wind tunnel studies and natural icing conditions dictates that care be taken in extrapolating results from icing wind tunnels to "similar" natural icing conditions.

REFERENCES

1. Olsen, W.A., Jr., Shaw, R., and Newton, J., "Ice Shapes and the Resulting Drag Increase for an NACA 0012 Airfoil." NASA TM 83556, 1984.
2. Gibbings, D.C., "Development for Helicopter Flight in Icing Conditions." AGARD CP-299, 1981.
3. MacArthur, C.D., "Numerical Simulation of Airfoil Ice Accretion." AIAA-83-0112, January 1983.
4. Lozowski, E.P., Stallabrass, J.R., and Hearty, P.F., "The Icing of an Unheated Non-Rotating Cylinder in Liquid Water Droplet-Ice Crystal Clouds." National Research Council of Canada (NRC) Report LTR-LT-86, February 1979.
5. Bragg, M.B., Gregorek, G.M., and Shaw, R.J., "An Analytical Approach to Airfoil Icing." AIAA-81-0403, January 1981.
6. Chang, H.P., Kimble, K.R., Frost, W., and Shaw, R.J., "Influence of Multidroplet Size Distribution on Icing Collection Efficiency." AIAA-83-0110, January 1983.
7. Gelder, T.F., Smyers, W.H., Jr., and Von Glahn, U., "Experimental Droplet Impingement on Several Two-Dimensional Airfoils with Thickness Ratios of 6 to 16 Percent." NACA TN 3839, December 1956.
8. Hansman, R.J., "The Effect of the Atmospheric Droplet Size Distribution on Airfoil Ice Accretion." AIAA-84-0108, January 1984.
9. Ruff, G.A., "Development of an Analytical Ice Accretion Prediction Method (LEWICE)." Sverdrup Technology, Inc., LeRC Group Progress Report, February 1986.
10. Kirchner, R.D., "Aircraft Icing Roughness Features and Its Effect on the Icing Process." AIAA-83-0111, January 1983.
11. Messinger, B.L., "Equilibrium Temperature of an Unheated Icing Surface as a Function of Airspeed." Journal of the Aeronautical Sciences, January 1953, pp 24-42.
12. Van Fossen, G.J., Simoneau, R.J., Olsen, W.A., and Shaw, R.J., "Heat Transfer Distributions Around Nominal Ice Accretion Shapes Formed on a Cylinder in the NASA Lewis Icing Research Tunnel." AIAA-84-0017, January 1984.

13. Personal communication with P.J. Perkins, Sverdrup Technology, Inc., Middleburg Heights, OH, January 1986.
14. Macklin, W.C., "The Density and Structure of Ice Formed by Accretion." Quarterly Journal of the Royal Meteorological Society, Vol. 88, No. 375, January 1962.
15. Brun, R.J., Lewis, W., Perkins, P.J., and Serafini, J.S., "Impingement of Cloud Droplets on a Cylinder and Procedure for Measuring Liquid-Water Content and Droplet Sizes in Supercooled Clouds by Rotating Multicylinder Method." NACA TR-1215, 1955.
16. Personal communication with W.A. Olsen, NASA Lewis Research Center, Cleveland, OH, March 1986.
17. Neel, C.B., Jr., and Steinmetz, C.P., "The Calculated and Measured Performance Characteristics of a Heated-Wire Liquid-Water-Content Meter for Measuring Icing Severity." NACA TN-2615, 1952.
18. Ide, R.F., and Richter, G.P., "Comparison of Icing Cloud Instruments for 1982-1983 Icing Season Flight Program." AIAA-84-0020, January 1984.

Appendix A

Measurement of Ice Accretion Using Ultrasonic Pulse-Echo Techniques

R. John Hansman Jr.* and Mark S. Kirby†
Massachusetts Institute of Technology, Cambridge, Massachusetts

Results of tests to measure ice thickness using ultrasonic pulse-echo techniques are presented. Tests conducted on simulated glaze ice, rime ice, and ice crystals are described. Additional tests on glaze and rime ice samples formed in the NASA Lewis Icing Research Tunnel are also described. The speed of propagation of the ultrasonic wave used for pulse-echo thickness measurements is found to be insensitive to the type of ice structure, and is determined to be 3.8 mm/μs. An accuracy of ±0.5 mm is achieved for ice thickness measurements using this technique.

Nomenclature

- a = radius of transducer element
- C = speed of propagation of ultrasonic wave
- D = thickness
- E = Young's modulus
- I = intensity of incident wave
- I_r = intensity of reflected wave
- R = reflection coefficient
- T = pulse-echo time
- Z = acoustic impedance
- λ = wavelength
- ν = Poisson's ratio
- ρ = density

Introduction

AIRCRAFT icing remains one of the most severe aviation weather hazards. A system to measure aircraft ice accretion and accretion rate in real time could directly reduce this hazard. Real-time measurement of ice accretion rate can provide the pilot with a quantitative evaluation of icing severity. Therefore, the effectiveness of changes in flight path to minimize ice accretion can be determined. In addition, by measuring ice accretion on critical components such as wings, engine inlets, propellers, or rotor blades, an ice accretion measurement system can be used to automatically activate and optimally control ice protection systems. Although many schemes have been suggested for measuring aircraft ice accretion,^{1,2} there remains a need for the development of a practical system capable of performing real-time, in situ measurement of ice accretion. The purpose of this study is to evaluate the feasibility and potential performance of an ice detection system using pulsed ultrasonic waves to measure ice thickness over a small transducer mounted flush with the aircraft surface. Since the technique of ultrasonic "pulse-echo" thickness measurement produces a real-time ice thickness signal, the ice accretion rate may be determined by electronically differentiating this thickness measurement with respect to time.

Theoretical Background

Ultrasonic Pulse-Echo Thickness Measurement

An ultrasonic transducer containing a piezoelectric element is mounted flush with the aircraft surface on which the ice

Received Nov. 25, 1984; presented as Paper 85-0471 at the AIAA 23rd Aerospace Sciences Meeting, Reno, Nev., Jan. 14-17, 1985; revision received Feb. 20, 1985. Copyright © American Institute of Aeronautics and Astronautics, Inc., 1985. All rights reserved.

*Assistant Professor, Aeronautics and Astronautics, Member AIAA.

†Research Assistant, Aeronautics and Astronautics.

thickness is to be measured. An ultrasonic pulse is emitted from the transducer and travels upward through the ice in a direction parallel to the emitting axis of the transducer (see Fig. 1). When this pulse reaches the ice/air interface above the transducer, it is reflected from the interface back down into the ice layer. This "echo" from the ice/air interface then returns to the aircraft surface where it is detected by the transducer, which now acts as a receiver. The velocity of the pulse-echo signal through the ice layer is determined solely by the density and elastic constants of the ice, and, hence, by measuring the time elapsed between the emission of the pulse and the return of the echo from the ice/air interface, the ice thickness D may be calculated from the following formula:

$$D = CT/2 \quad (1)$$

where C is the velocity of the pulse-echo signal in ice (speed of sound in ice), and T the time elapsed between the pulse emission and echo return from the ice/air interface.

Speed of Propagation

The "pulse" produced by the ultrasonic transducer is a short-duration compression wave (longitudinal wave). The

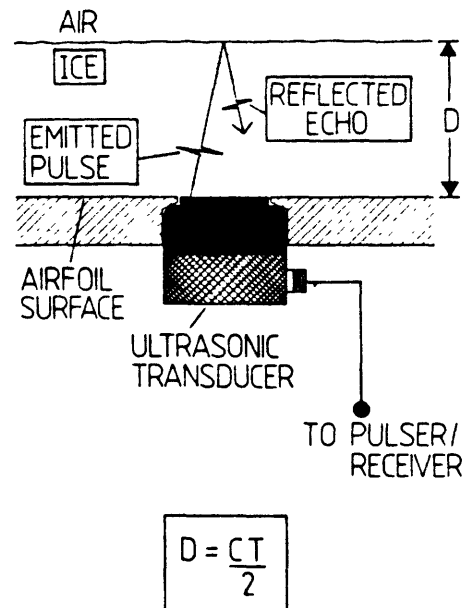


Fig. 1 Ultrasonic pulse-echo thickness measurement.

velocity C at which such a compression wave propagates through a solid medium is theoretically predicted¹ to be

$$C = \sqrt{\frac{E(1-\nu)}{\rho(1+\nu)(1-2\nu)}} \quad (2)$$

where E is the Young's modulus for the medium, ν the Poisson's ratio, and ρ the density of the medium. Hence, the pulse-echo signal propagates through a solid medium at a constant velocity that depends only on the density and elastic constants of the medium.

Reflection of Ultrasonic Signal from Ice/Air Interface

The ultrasonic pulse is reflected back toward the transducer (as the echo signal) at the ice/air interface (Fig. 1) because of the difference in the acoustic impedances of ice and air. The acoustic impedance, Z , of a medium is defined as the product of the medium's density, ρ , and the speed of sound in the medium, C , given by Eq. (2); hence,

$$Z = \rho C \quad (3)$$

The reflection coefficient, R , for an interface is defined⁴ as the ratio of the intensity of the reflected wave, I_r , to that of the incident wave, I_i , and is given by

$$R = \frac{I_r}{I_i} = \left(\frac{Z_1 - Z_2}{Z_1 + Z_2} \right)^2 \quad (4)$$

where Z_1 and Z_2 are the acoustic impedances of the two media forming the interface. From this equation it can be seen that the intensity of the reflected wave, or echo signal, depends on the acoustic impedance mismatch between the two media. Since both the density and speed of sound in air are considerably lower than those for solids, the acoustic impedance mismatch for a solid/air interface is large, resulting in strong reflection at a solid/air interface. For an ice/air interface the reflection coefficient is calculated to be greater than 0.99, i.e., more than 99% of the incident wave energy is reflected at an ice/air interface.

Coupling

For the vibration of the transducer element to be transmitted into a solid medium, a "coupling" mechanism between the transducer and the solid must be available. Although it is often necessary to use a fluid to provide this coupling mechanism, no such fluid is required for ice thickness measurement since the ice is atomically bonded to the transducer face and, therefore, is constrained to vibrate with the transducer element.

Ultrasonic Field Shape

At the high frequencies (5-20 MHz) used for pulse-echo ice thickness measurement, the wavelength λ in the ice is typically small (< 1 mm) compared to the radius a of the radiating transducer element. Under these conditions the ultrasonic wave propagates from the transducer as a collimated beam of the same diameter as the transducer element. This beam, or near-field region, extends for a distance given by the ratio a^2/λ , after which the wave diverges in the far-field region. Typical near-field ranges are approximately 2 in. for a 0.5-in.-diam, 5-MHz transducer and 1 in. for a 0.25-in.-diam, 10-MHz transducer.

Attenuation

Attenuation of the received echo signal can be divided into three components: absorption and scattering within the ice, and reflection at the ice/air interface. Absorption occurs as part of the vibrational energy of the wave is stored as heat by the ice molecules and then lost through irreversible heat

transfer within the ice layer. Scattering is caused by any inclusions within the ice (such as air bubbles), since, by definition, these inclusions have a different acoustic impedance to that of the ice and, therefore, present spurious reflective interfaces to the incident ultrasonic wave. The third factor affecting the received strength of the echo signal is the shape of the ice/air interface itself. While almost 100% of the incident wave energy is reflected at the ice/air interface, the shape of the interface determines the direction(s) of reflected wave propagation. Rough ice surfaces will reflect the incident wave diffusely, while ice surfaces that are not parallel to the transducer face will cause the echo signal to propagate at an angle to the emitting axis of the transducer. In both cases the intensity of the echo received by the transducer will be diminished over that received from an identical ice thickness with a flat, parallel ice/air surface.

Experimental Apparatus

Three components comprised the pulse-echo thickness measurement system tested: a transducer, a pulser/receiver unit, and an oscilloscope (Fig. 2). The function and important performance characteristics of each of the components are outlined below. The experimental apparatus constructed to simulate and test the application of this pulse-echo system to ice accretion measurement is then described.

Transducer

The transducer used to produce and receive the ultrasonic pulse-echo signal was a broadband, highly damped contact transducer. This type of transducer allows maximum signal penetration in attenuating and scattering materials such as rime and glaze ice. Excellent thickness resolution is also possible with this type of transducer. A single transducer was used for all of the tests described. The transducer tested had a center frequency of 5 MHz and an element diameter of 0.5 in.

Pulser/Receiver

The pulser/receiver provides the electrical signals necessary for the operation of the transducer in a pulse-echo mode. The pulser section of the pulser/receiver supplies the transducer element with a short, high-voltage pulse of controlled energy.

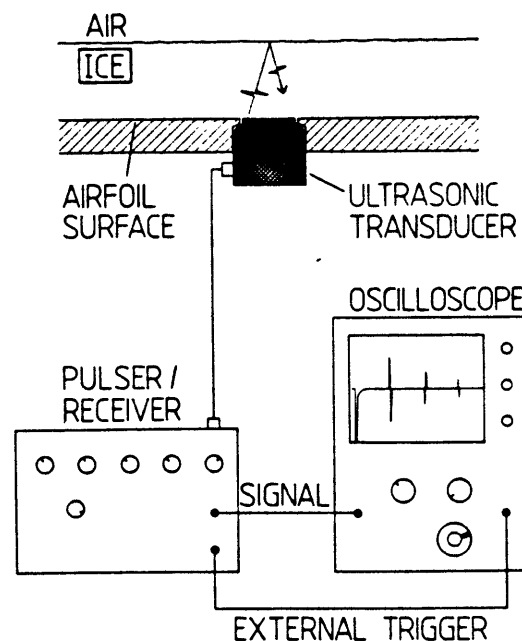


Fig. 2 Ultrasonic pulse-echo system.

This voltage pulse causes the transducer element to vibrate, thus producing the ultrasonic pulse utilized in pulse-echo thickness measurement. The voltage applied to the transducer element is typically on the order of 200 V. The voltage pulse is reapplied to the transducer element several hundred times per second to produce a "continuous" pulse-echo thickness reading. The receiver section amplifies and conditions the small echo voltage produced by the transducer element itself. The typical gain required is approximately 40 dB. In addition, the pulser-receiver provides a synchronizing voltage used to trigger an oscilloscope sweep momentarily before the main voltage pulse is applied to the transducer element. For experimental purposes, an oscilloscope was used to observe the pulse-echo signal characteristics in different ice formations and measure the pulse-echo time. Figure 3 shows a typical pulse-echo trace obtained from a 5.0-mm-thick ice layer.

Experimental Apparatus

To allow ice to be frozen over the transducer face and the pulse-echo system tested, the apparatus shown in Fig. 4 was used. A circular 9-in.-diam aluminum plate served as a test surface on which the ice accretion was to be measured. The transducer was mounted in the center of this plate with the transducer face flush with the plate surface. An 8-in.-diam plexiglas cylinder could be used to contain water poured onto the plate surface when it was desired to freeze liquid water over the face of the transducer (in order to simulate glaze ice). A removable plexiglas lid could be fitted over this cylinder; the purpose of the lid was to provide a reference level from which the ice thickness over the plate surface could be accurately measured by inserting a steel probe graduated in millimeters through one of a grid of small holes drilled into the lid. The aluminum plate was also instrumented with two

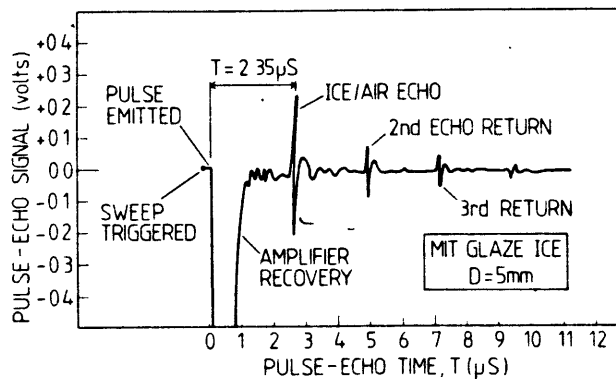


Fig. 3 Typical pulse-echo trace for ice.

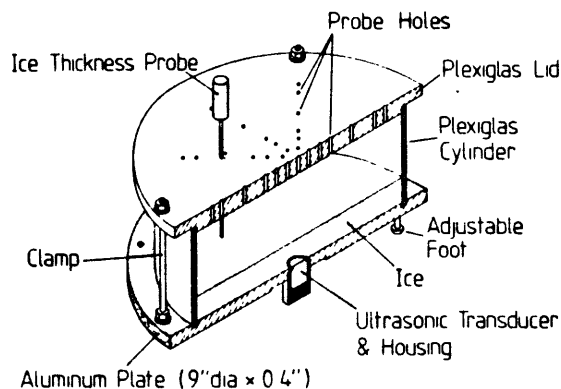


Fig. 4 Experimental apparatus.

chromel/alumel thermocouples to monitor the plate-ice temperature.

Testing

In order to calibrate the configured pulse-echo system, aluminum and plexiglas samples of different thicknesses were measured using the ultrasonic pulse-echo technique. By comparing the measured speed of sound in the material,

$$C = 2D/T \quad (5)$$

with well-established values, the error in the obtainable pulse-echo thickness measurements was determined to be less than 5% for equivalent ice thicknesses from 1 to 30 mm. Testing of the pulse-echo system comprised two consecutive series of trials. The first series consisted of tests performed on ice formed at MIT. Both glaze and rime ice structures were simulated and ice thicknesses from 1.5 to 31 mm were tested. Additional tests were also performed on ice crystal formations. The second series of tests utilized ice samples obtained from the Icing Research Tunnel (IRT) at NASA Lewis Research Center. Glaze and rime ice formations from 4.5- to 15-mm thick were tested in this series of tests.

MIT Glaze Ice Simulation Tests

Glaze ice was simulated by pouring water into the plexiglas cylinder/plate apparatus (Fig. 4) to a depth approximately equal to the desired ice thickness, and then the apparatus was placed in a cold box thermostatically maintained at -20°C . Once the water was completely frozen, the pulse-echo time T was recorded from the oscilloscope display. The apparatus was then removed from the cold box so the ice thickness could be measured with the graduated probe as described earlier. The ice thickness was always recorded within 1 min of removal from the cold box and no appreciable rise in ice temperature (as indicated by the plate thermocouples) took place between the recording of the pulse-echo time and the corresponding ice thickness measurement.

MIT Rime Ice Simulation Tests

To simulate rime ice, the aluminum plate containing the ultrasonic transducer was first placed in the cold box. Once the plate had reached its steady-state temperature (typically -18°C), water droplets at 0°C were sprayed onto the plate/transducer face using a misting nozzle connected to a small electric pump and ice/water reservoir (Fig. 5). The droplets were sprayed intermittently rather than continuously to prevent the ice temperature from significantly increasing as a result of the heat of fusion released by the freezing water droplets. Droplets were typically observed to freeze within 2 s of impact with the plate surface. Measurement of the pulse-echo time and ice thickness was made in a manner similar to that described for the glaze ice simulation tests.

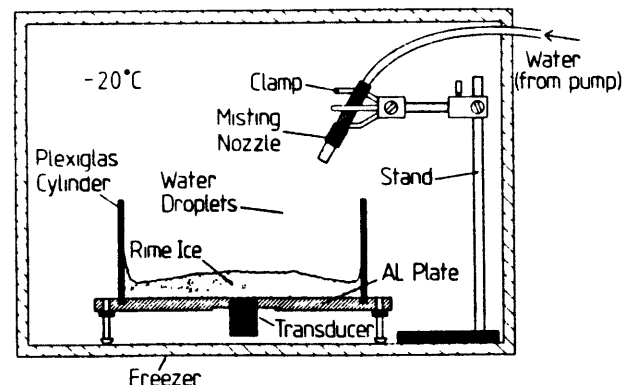


Fig. 5 Rime ice simulation method.

MIT Ice Crystal Tests

To simulate a limiting case for air entrapment within an ice structure and investigate the propagation of an ultrasonic wave through such a structure, ice crystals were compacted over the plate/transducer surface. The structure thus formed contained air gaps on the order of 1-3 mm between individual ice crystals. As in the previous simulations, pulse-echo time and ice thickness were recorded for these ice formations.

NASA Lewis Ice Tests

The second series of tests conducted with the pulse-echo system involved ice samples obtained from airfoil sections installed in the NASA Lewis Icing Research Tunnel. The ice samples were obtained under a variety of documented tunnel/icing cloud conditions and shipped in dry ice to MIT, where the tests with the pulse-echo system were conducted. In order to bond the ice samples to the flat transducer surface, a thin film (<0.1 mm) of water at 0°C was applied to the "airfoil" side of the ice sample. The ice sample was then simply placed over the transducer face (at -18°C), the water film under the ice sample freezing on contact with the cold transducer face thus bonding the ice sample to the transducer in the same orientation as would have occurred if the transducer had been mounted in the airfoil. No appreciable change in either the internal structure of the ice or the "top" ice/air surface of any of the NASA ice samples tested was observed as a result of this procedure. Once the ice sample under test had been successfully bonded to the transducer, the pulse-echo time in the sample was recorded from the oscilloscope display, as in the other ice simulation tests. The aluminum plate was then removed from the cold box and the average ice thickness over the transducer was measured.

Results and Discussion

MIT Glaze Ice, Rime Ice, and Ice Crystal Results

The results from the tests conducted on ice formed at MIT are plotted together in Fig. 6 as ice thickness D vs pulse-echo time T . Regression lines were fitted to the glaze and rime ice results in order to calculate the experimentally measured speed of sound for these ice structures. Therefore, the speed of sound C in Eq. (5) is simply twice the slope of the regression line. The experimentally determined values for the speed of sound in the glaze and rime ice formed at MIT were 3.78 and 3.95 mm/ μ s, respectively. A regression line was not fitted to the data from the ice crystal tests due to the small number of data points. However, it can be seen from Fig. 6 that the speed of sound in the ice crystal structure does not differ significantly from the values obtained for the glaze and rime ice structures. The typical error bar shown represents the inherent uncertainty for any ice thickness measurement made with the mechanical probe arrangement described earlier.

NASA Lewis Ice Results

In order to compare the results from the tests performed on the NASA Lewis IRT ice with those from the MIT ice structures, each of the NASA Lewis ice samples tested was categorized as either glaze or rime ice. The ice samples were categorized according to the tunnel temperatures at which they were formed and their physical characteristics (e.g., milky, clear, double-ridged surface, etc.). Figure 7 shows a scatter plot of the results obtained from the NASA Lewis ice samples, again with ice thickness plotted against pulse-echo time. Due to the small number of tests performed on each type of ice (glaze or rime), regression lines were not fitted to these results. However, the linear relationship between ice thickness and

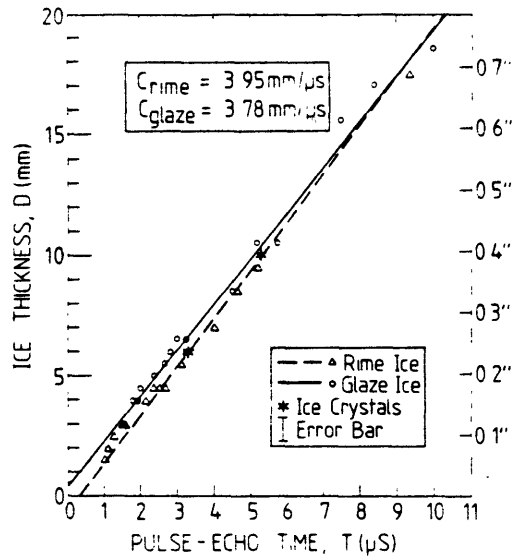


Fig. 6 Ice thickness vs pulse-echo time for MIT glaze and rime ice samples.

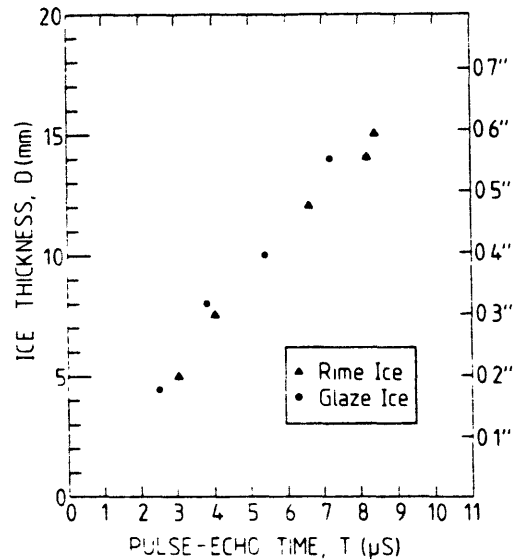


Fig. 7 Ice thickness vs pulse-echo time for NASA Lewis ice samples.

pulse-echo time—indicating a constant speed of sound—readily can be seen. Furthermore, the speed of sound, as indicated by the slope of the data, does not seem to be sensitive to the type of ice present. The greater spread in the data obtained for the NASA Lewis ice can be explained as follows. The NASA Lewis ice samples were all collected from airfoil surfaces in the IRT and all displayed either rough (rime ice) or concave (glaze ice) ice/air surfaces, while the ice surfaces produced during the MIT glaze and rime ice tests were generally flat and uniform. As a result of the surface irregularity of the NASA Lewis ice samples, it was often necessary to record an average ice thickness over the transducer and similarly a corresponding average pulse-echo time, since the echo from the ice/air interface above the transducer was now broadened by the irregular interface. Therefore, the NASA Lewis results have a larger typical error in both measured ice thickness and recorded pulse-echo time than the more "ideal" MIT ice results.

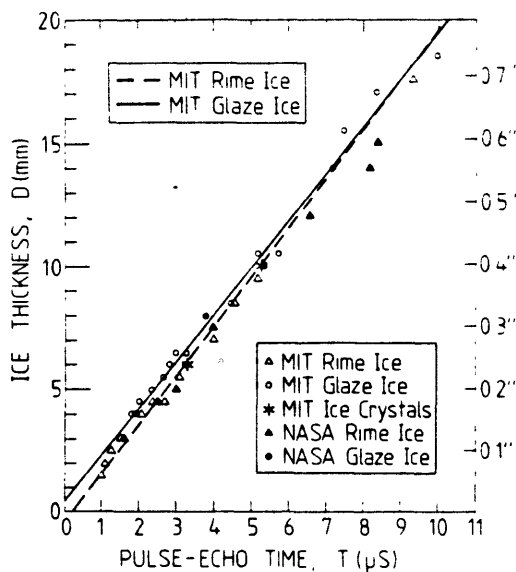


Fig. 8 Ice thickness vs pulse-echo time: MIT glaze and rime ice, NASA glaze and rime ice.

Although the actual uncertainty for any single NASA Lewis result depended on the particular ice sample geometry, the average uncertainty in these test results is approximately ± 1 mm for ice thickness and $\pm 0.5 \mu\text{s}$ for the corresponding pulse-echo time. Comparing the results from the MIT and NASA Lewis ice tests (Fig. 8) it can be seen that the results from the two series of tests correlate extremely well[‡]—especially considering the wide range of “icing” conditions under which the ice tested was formed. The slight difference between the experimentally determined speeds of sound for the MIT glaze and rime ice is within the expected data spread due to experimental error (primarily in measuring ice thickness with the mechanical probe), and the results from the tests conducted on the NASA Lewis IRT ice samples confirm that the speed of sound is insensitive to the type of ice present. Therefore, the results from both series of tests (MIT and NASA Lewis) may be regressed together to give an average or “effective” speed of sound in ice of $3.8 \text{ mm}/\mu\text{s}$. (This compares with a value of $3.98 \text{ mm}/\mu\text{s}$ quoted by Filipczynski et al.⁴ for “ice.”)

Since the speed of sound in ice must be known to calculate ice thickness from a measured pulse-echo time, the observed insensitivity of this speed of sound to the type of ice present permits pulse-echo time to be uniformly converted to ice thickness using this average speed of sound. One explanation for the similar speeds of sound measured in both rime and glaze ice formations is that, despite their optical differences, these ice structures are acoustically equivalent. Macklin⁵ has shown ice density to be relatively constant ($0.8 < \rho < 0.9 \text{ g}/\text{cm}^3$) at higher droplet impact velocities over a wide temperature range. If, in addition, the elastic constants for glaze and rime ice are also approximately equal, then ice structures formed under different icing conditions would yield similar speeds of sound, as observed. However, further study of both the speed of propagation and attenuation of ultrasonic compression waves in different ice structures is still needed to confirm the physical basis for the observed insensitivity of the speed of sound in different ice types.

The practical resolution of ice thickness achievable using the ultrasonic pulse-echo technique depends primarily on the diameter and frequency of the transducer element used. Since, within the near field, the ultrasonic wave propagates as a collimated beam of the same diameter as the transducer element,

[‡]The bulk correlation coefficient for all of the tests performed is 0.994.

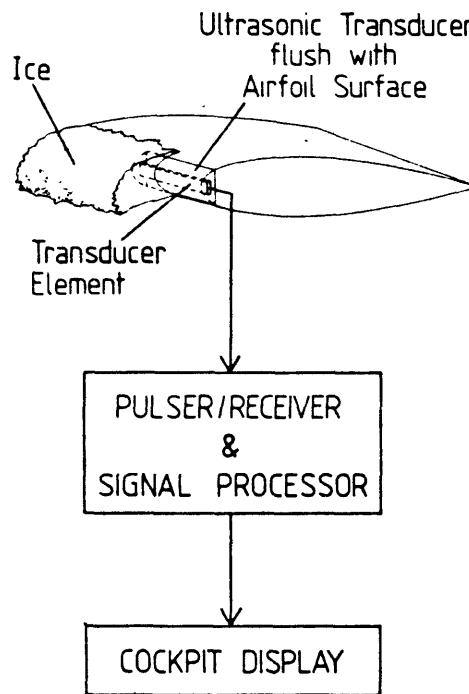


Fig. 9 Pulse-echo ice accretion measurement, system layout.

the resolution is limited by the ice thickness variation across the beam diameter at the ice/air interface. The spread in the data obtained from the tests conducted on ice shape geometries typically encountered on airfoils during flight in icing conditions (NASA Lewis ice tests) suggests an accuracy of better than 1 mm should be achieved for practical ice accretion measurements using pulse-echo techniques. The uncertainty due to ice thickness variation over the transducer can be minimized by the use of smaller diameter transducers; however, higher frequencies must be employed to remain in the near-field region.

Conclusions

Tests conducted on simulated rime and glaze ice formations and rime and glaze ice samples removed from airfoil sections installed in the Icing Research Tunnel at NASA Lewis Research Center have provided the following information.

1) An ultrasonic pulse, or compression wave, can be propagated through all ice formations likely to be encountered during flight in icing conditions and a return “echo” from the ice/air interface clearly discerned, using relatively inexpensive ultrasonic pulse-echo equipment.

2) An ultrasonic pulse propagates through ice at a velocity that does not significantly depend on the type of ice formation present. This velocity was experimentally determined to be $3.8 \text{ mm}/\mu\text{s}$. Therefore, ice thickness may be calculated from the measured pulse-echo time and this “constant” speed of sound, regardless of the type of ice accreted.

3) Ice thickness variations across the ultrasonic field produced by the radiating transducer result in a corresponding broadening of the echo from the ice/air interface. If the pulse-echo time is measured from the pulse emission to the “center” of the echo return, then an average ice thickness over the transducer is obtained. Likewise, if the pulse-echo time is taken to be the time elapsed between the pulse emission and the start of the echo return from the ice/air interface, then the minimum ice thickness over the transducer is measured.

4) The rough and/or concave ice surfaces characteristic of rime and glaze ice formations scatter the incident ultrasonic pulse and, therefore, reduce the strength of the echo signal received by the transducer. However, the echo signal is not

obscured and the pulse-echo time can be measured in all of the ice shapes typically encountered during flight in icing conditions.

Therefore, ultrasonic pulse-echo thickness measurement is considered to offer a practical solution to the problem of real-time ice accretion measurement for aircraft encountering icing conditions. The operational accuracy achievable with such a system depends primarily on the transducer specifications (frequency and element diameter) and the location of the transducer. An accuracy of ± 0.5 mm for ice thickness measurement is predicted. The configured ultrasonic pulse-echo system would comprise three components: an ultrasonic transducer, a pulser/receiver and signal processing unit, and a cockpit display (Fig. 9). The transducer is nonintrusive and mounted flush with the surface on which ice accretion is to be measured. The transducer units are small and lightweight and, therefore, may be mounted on almost any vulnerable surface, including helicopter rotor blades and engine inlets. The signal processor calculates the ice thickness from the measured pulse-echo time and also differentiates this real-time measurement with respect to time to obtain the ice accretion rate. The cockpit display unit provides the pilot with an automatic "icing encountered" alert and indicates icing severity as well

as controlling and or monitoring the operation of fitted ice protection systems.

Acknowledgment

This work was supported by the National Aviation and Space Administration under Grants NAG-1-100 and NGL-22-009-640.

References

- ¹Perkins, P. J., McCullough, S., and Lewis, R. D., "A Simplified Instrument for Recording and Indicating Frequency and Intensity of Icing Conditions Encountered in Flight," NACA RM-E 51E16, 1951.
- ²Magenheim, B. and Rocks, J. K., "Development and Test of a Microwave Ice Accretion Measurement Instrument (MIAMI)," NASA CR-3598, 1982.
- ³Ide, R. E. and Richter, G. P., "Evaluation of Icing Cloud Instrumentation for 1982-83 Icing Season Flight Program," AIAA Paper 84-0020, Jan. 1984.
- ⁴Filipczynski, L., Pawlowski, Z., and Wehr, J., *Ultrasonic Methods of Testing Materials*, Butterworths, London, 1966.
- ⁵Macklin, W. C., "Density and Structure of Ice Formed by Accretion," *Quarterly Journal of the Royal Meteorological Society*, Vol. 88, No. 375, Jan. 1962, pp. 30-50.

Appendix B

CALCULATION OF LIQUID WATER CONTENT FOR CYLINDER LOCATION OUTSIDE CALIBRATED CLOUD REGION

In order to estimate the actual liquid water content at the cylinder location, as a percentage of the (known) calibrated cloud value, the following approach was taken. The expected dry growth accretion rates on the cylinder stagnation line were analytically calculated (from Ref. 15) using the calibrated cloud liquid water content and median volume diameter values. These "calibrated cloud" accretion rates, \dot{D}_{cal} , were then compared to the experimentally measured dry growth rates on the cylinder, \dot{D}_{cyl} , and the ratio of these two rates was used to give the liquid water content at the cylinder location as a percentage of the calibrated cloud value.

For the ultrasonically measured dry ice growth rate, \dot{D}_{cyl} , on the cylinder stagnation line,

$$\dot{D}_{cyl} = (BW)_{cyl} V_{\infty} / \rho_{ice} \quad (B.1)$$

Where $(BW)_{cyl}$ is the actual impinging liquid water content on the cylinder stagnation line.

The analytically calculated accretion rate, \dot{D}_{cal} , based on the calibrated cloud values, is given by,

$$\dot{D}_{cal} = (\beta W)_{cal} V_{\infty} / \rho_{ice} \quad (B.2)$$

Where $(\beta W)_{cal}$ is the liquid water content that would impinge on the cylinder stagnation line if the cylinder were located in the calibrated cloud region of the test section.

Equations B.1 and B.2 may be combined to give,

$$\dot{D}_{cyl} / \dot{D}_{cal} = (\beta W)_{cyl} / (\beta W)_{cal} \quad (B.3)$$

Note that it has been assumed that the both the freestream velocity and ice density are the same for the cylinder location and calibrated cloud region.

If the droplet size distribution at the cylinder location is close to that in that calibrated region then the local collection efficiency terms may be cancelled and equation B.3 yields the desired ratio of liquid water contents,

$$\dot{D}_{cyl} / \dot{D}_{cal} = W_{cyl} / W_{cal} \quad (B.4)$$

Thus by comparing the measured accretion rates with the rates calculated for the calibrated cloud region, a

correction factor for the liquid water content at the cylinder location may be obtained. It should be noted that if the droplet size distribution does vary significantly over the test section then equation B.4 will not provide a consistent ratio for the liquid water contents. However the ratios obtained from equation B.4 were almost identical for different droplet sizes (MVD), indicating any effective difference in the droplet size distribution is small.

Table B.1 lists the five different calibrated cloud conditions tested (different icing cloud temperatures were tested for each of the conditions shown), and the experimentally measured dry growth rates for each condition. The analytically calculated rates for the calibrated region, \dot{D}_{cal} , are also shown.

LWC (g/m ³)	MVD (μ)	VEL (mph)	\dot{D}_{cyl} (mm/min)	\dot{D}_{cal} (mm/min)	$\dot{D}_{cyl}/\dot{D}_{cal}$ (-)
1.2	20	230	3.15	5.09	0.62
0.6	12	230	1.05	1.61	0.65
0.83	14	160	1.11	1.59	0.69
1.7	20.5	160	N/A	4.61	-
2.4	18	110	N/A	3.40	-
1.2	14	110	0.78	1.31	0.60

Table B-1. Summary of data used to calculate liquid water content for cylinder location.

(N/A = No dry growth observed, since no cold cloud temperature runs were performed for those two icing conditions.)

From equation B.4 and the values listed in Table B-1 for the accretion rate ratios, $\dot{D}_{\text{cyl}}/\dot{D}_{\text{cal}}$, the average ratio inferred for the liquid water content at the cylinder location is thus,

$$W_{\text{cyl}}/W_{\text{cal}} = \overline{\dot{D}_{\text{cyl}}/\dot{D}_{\text{cal}}} = (0.62 + 0.65 + 0.69 + 0.60)/4$$

$$\underline{W_{\text{cyl}} = 0.64 W_{\text{cal}}}$$

Hence the liquid water content at the cylinder location, W_{cyl} , is estimated to be approximately 64% of the calibrated cloud value, W_{cal} .